

Robert Bohle

Development of a Virtual Soft X-Ray Diagnostics and its Application to Ideal Kink Instabilities

IPP 1/342
July, 2011

DEVELOPMENT OF A VIRTUAL SOFT X-RAY DIAGNOSTICS AND ITS APPLICATION TO IDEAL KINK INSTABILITIES

Diploma Thesis
by
Robert Bohle

July 2011



Max-Planck-Institut
für Plasmaphysik

primary reviewer: Prof. Dr. Hartmut Zohm
secondary reviewer: Prof. Dr. Harald Lesch

ABSTRACT

Magnetically confined plasma in a tokamak is a possible energy source for future fusion reactors. The fusion plasma emits soft x-ray (sxr) radiation and occurring MHD instabilities displace the spatial radiation distribution. The volume integrated emissivity and its variation is measured in ASDEX Upgrade with pinhole sxr detectors.

In the scope of this thesis a virtual soft x-ray diagnostics is developed taking into account the full three-dimensional geometry. A model for the emissivity of a mode perturbed plasma is developed considering the poloidal displacement which depends on the toroidal position.

The consideration of the full poloidal geometry is crucial since it is shown here that a previously used model is incapable of reproducing observed phenomena but produces unphysical mathematical artifacts.

Applying the virtual sxr diagnostics in combination with the model of mode perturbed emissivity it is discussed, that the time dependent simulated signals depend on the background emissivity $e_0(\rho)$ (especially its gradient), the magnetic structure of the mode described by the displacement function $\vec{\xi}$ and the geometry of the equilibrium flux surfaces. It is also shown that there is coupling between the dependencies.

By keeping two of these three dependencies constant and varying the third, the resulting effects on the time dependent simulated signals of idealized examples of ideal internal $(m, n) = (1, 1)$ kink modes are investigated. New insight is gained because the effects are isolated from disturbing influences and they are studied under well defined conditions.

By the variation of the background emissivity and the displacement the simulated signals are fitted to the time dependent signals which result from observed kink modes. Good agreement has been achieved for peaked as well as for hollow emissivity profiles. However, asymmetries due to non-constant radiation of flux surfaces can not yet be described. This is recommended for future work.

Contents

| | | |
|----------|--|-----------|
| 1 | Introduction | 5 |
| 1.1 | Why do we need fusion research? | 5 |
| 1.2 | Thermonuclear fusion, MHD equations and the Tokamak | 6 |
| 1.2.1 | Magnetic confinement and plasma equilibrium | 7 |
| 1.2.2 | The flux coordinates ρ_{pol} and θ^* | 8 |
| 1.2.3 | Plasma instabilities and their displacement | 12 |
| 1.3 | Motivation and Outline | 15 |
| 2 | The soft x-ray diagnostics at AUG and the quantity emissivity | 17 |
| 2.1 | The pinhole detector array and its geometry | 17 |
| 2.2 | Pinhole-camera-tile arrangement | 19 |
| 2.3 | Creation mechanisms of soft x-ray radiation | 20 |
| 2.4 | The emissivity | 21 |
| 3 | The virtual soft x-ray diagnostics | 22 |
| 3.1 | An analytical formula for the signal | 22 |
| 3.2 | Numerics of the camera simulation | 25 |
| 3.3 | Test of the camera simulation | 26 |
| 4 | Models of emissivity | 29 |
| 4.1 | Emissivity as a flux surface quantity | 29 |
| 4.2 | The emissivity of mode-perturbed plasma | 32 |
| 4.3 | A comparison of emissivity models | 38 |
| 4.4 | Properties of modes defined in flux coordinates | 44 |
| 5 | Investigation of idealized internal kink modes | 48 |
| 5.1 | Impact of the displacement variation | 49 |
| 5.2 | Impact of emissivity variation | 55 |
| 5.3 | Impact of the equilibrium variation | 60 |
| 6 | Experimental investigation of (1,1)-kink modes | 65 |
| 6.1 | Fitting the equilibrium emissivity and its asymmetries | 65 |
| 6.2 | The investigation of the magnetic-structure of a kink mode | 68 |
| 6.3 | Investigation of a kink mode with a hollow emissivity profile | 69 |
| 7 | Recommendations for future work and Conclusion | 72 |
| | Appendix | 76 |
| | Appendix A | |
| | Signals resulting from the approximate model are harmonic in time | 76 |
| | Appendix B | |
| | AVOS of the sxr channels in AUG | 77 |

Abbreviations and names

Tokamak ТОроидапная КАмера в МАГнитных КАтушках
which means translated toroidal chamber with magnetic coils

AUG ASDEX Upgrade

MHD magneto-hydro-dynamics

VOS volume of sight

LOS line of sight

AVOS axis of the VOS

SXR soft x-ray

ECE electron cyclotron emission

NBI neutral beam injection

CLISTE a code to calculate the plasma equilibrium

STRAHL a code to calculate the radial transport of impurities

LFS low field side

HFS high field side

ELM edge localized mode

NTM neoclassical tearing mode

FFT fast Fourier transformation

RSS residual sum of squares

FWHM full width at half maximum

1 Introduction

The sun produces - by a natural occurring fusion process - the daylight we see and it is the goal of fusion research to develop a way to control an artificial induced fusion process so that energy generation is possible. In the following sections a very short introduction in the physics of fusion is given.

1.1 Why do we need fusion research?

The worlds energy demand is predicted to increase by 33% between 2011 and 2035 [1]. The main options we have today to cover up the energy need can be ordered into the three generation types and in the following the difficulties which are associated with these production types are described shortly [2].

First, the use of fossil energy has destructive environmental effects and also the recourse of it is limited and the consumption is creating a dependence on fossil-fuel-producing-countries.

Second, nuclear energy is connected with the unsolved problem of the final disposal of nuclear waste. Besides, the fact that weapons-usable plutonium can be produced there is the remaining risk of a maximum credible accident and there are possible health risks connected with the mining of uranium.

Last, renewable energies like wind and solar energy are only temporarily available, because an efficient storage does not exist. Hydropower depends on the local infrastructure of an embankment dam. The use of biogas goes along with monocultures and generally the consumption of resources is enormous.

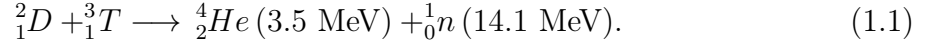
It is the goal of fusion research to develop a fusion power plant - driven by an artificial induced fusion process - which overcomes the above mentioned difficulties of present energy production. A future fusion power plant will be intrinsically safe, because the conditions required for energy generation are difficult to maintain [3]. Any deviation away from these conditions will stop the fusion processes and no further fusion-energy is released. Moreover, the activated atoms in the vessel only have a half-life of a few hundred years.

The energy source would be quasi unlimited because there is plenty of deuterium everywhere, the needed tritium is self-produced in the breeding blankets from lithium; another advantage is that there are no harmful environment effects [4].

Nobody knows whether nuclear fusion power plants will one day produce our energy; but we do know that it is difficult to cover up the increasing energy need. Therefore it is worthwhile to bring to light whether fusion is a practicable way for the energy supply of our future.

1.2 Thermonuclear fusion, MHD equations and the Tokamak

Nuclear fusion is the process of merging two atomic nuclei to one new atomic nucleus. There are fusion processes for which the mass of the resulting particles is smaller than before the fusion. This mass defect Δm results from released binding energy and it is released in form of kinetic energy. Let us for example consider the fusion of the hydrogen isotopes tritium and deuterium



The energy needed to overcome the classical Coulomb barrier ($\approx 380\text{keV}$ for D-T) is much lower than the energy gained by the fusion process [5]. For fusion it is not necessary for the nuclei to overcome the Coulomb barrier because of the quantum-mechanical effect of tunneling.

According to the mass proportion of the neutron and helium, the neutron has a kinetic energy of 14.1 MeV and future fusion reactors will gain the energy out of the particle flux. Since the above introduced D-T reaction has by far the largest cross-section at the lowest energies it is the most promising candidate for an energy-producing system [5].

In order to maximize the neutron flux the reactants are forced into the plasma state in which almost all particles are ionized. With present fusion devices thermonuclear fusion can be achieved with a temperature of about 10 keV (about 100 million degrees) [6]. There is no material which could withstand this plasma and so it is confined with magnetic fields.

Although the plasma consists at least of protons and of electrons, a magnetically confined plasma can be described as a conductive and electrically neutral fluid which reacts to magnetic fields [6]. This model is called Magneto-hydro-dynamics (MHD) and it consists of a combination of Maxwell's equations with the equations of fluid dynamics. In the ideal MHD the resistivity of the plasma is neglected, therefore the magnetic field lines can not reconnect and the topology of the field lines is maintained. The equations of ideal MHD read:

mass conservation:

$$\frac{\partial \rho}{\partial t} + \vec{\nabla} \cdot \rho \vec{v} = 0 \quad (1.2)$$

Ampere's law:

$$\vec{j} = \frac{1}{\mu_0} \vec{\nabla} \times \vec{B} \quad (1.3)$$

adiabatic equation:

$$\left(\frac{\partial}{\partial t} + \vec{v} \cdot \vec{\nabla} \right) p + \frac{5}{3} p \vec{\nabla} \cdot \vec{v} = 0 \quad (1.4)$$

MHD kinematic equation:

$$\frac{\partial \vec{B}}{\partial t} = \vec{\nabla} \times (\vec{v} \times \vec{B}) \quad (1.5)$$

absence of magnetic charges:

$$\vec{\nabla} \cdot \vec{B} = 0 \quad (1.6)$$

momentum equation:

$$\rho \left(\frac{\partial}{\partial t} + \vec{v} \cdot \vec{\nabla} \right) \vec{v} = -\vec{\nabla} p + \vec{j} \times \vec{B} \quad (1.7)$$

1.2.1 Magnetic confinement and plasma equilibrium

Under several different geometrical setups to provide magnetical confinement the Tokamak is the most developed one and it is briefly described in the following section [5].

The constituent parts of a Tokamak are shown in figure 1.1. The plasma is confined in a torus-like volume by the toroidal and the poloidal fields. The toroidal field is produced by the external toroidal field coils. It is much stronger than the poloidal field produced by the toroidal plasma current which results from the change of the current in the primary transformer circuit [6]. With the currents in the introduced external coils the shape and the position of the plasma is controlled and determined [6].

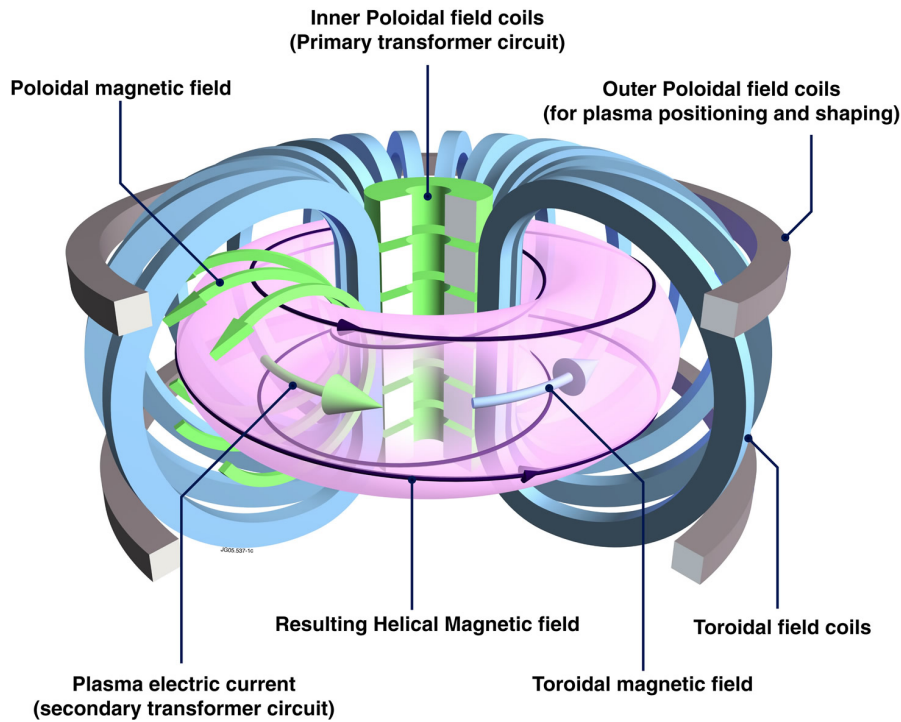


Figure 1.1 – Constituent parts of a Tokamak referring to [3].

In the state of equilibrium the time derivatives in the MHD equations 1.2 - 1.7 vanish. With $\vec{v} = 0$ for the flow of the plasma \vec{v} (this is a good assumption if $v \ll c_s$, with c_s being the ion sound velocity) the momentum equation 1.7 reduces to the force balance equation $\nabla p = \vec{j} \times \vec{B}$ and there is an internal balance between the pressure of the plasma p and the forces due to the total magnetic field \vec{B} . The field lines of \vec{B} lie in surfaces of constant pressure. These surfaces are called flux surfaces and they are plotted in a typical poloidal cross section in figure 2.2.

In order to achieve high temperature the plasmas energy is increased with various heating systems and, furthermore, the energy must be confined in the plasma and the efficiency of the confinement of plasma pressure by the magnetic field is represented by the ratio

$$\beta = \frac{2\mu_0 \langle p \rangle}{B^2} = \frac{\text{thermal pressure}}{\text{magn. pressure}} \quad [6].$$

1.2.2 The flux coordinates ρ_{pol} and θ^*

Equations simplify by choosing proper coordinate systems. The torus coordinate system is introduced in figure 1.2. R denotes the major radius and r denotes the minor radius. The shape of the confined plasma is deformed and in the following the *radial* (poloidal) flux coordinate ρ_{pol} and the straight field line angle θ^* are introduced.

For the definition of ρ_{pol} let us consider an arbitrary flux surface. Let C_t be an arbitrary closed curve on one flux surface which circulates once poloidally and which does not circulate toroidally. Let A be the area which is carved out by the curve C_t . The poloidal flux ψ_{pol} which passes through the surface A is given by $\psi_{pol} = \int \vec{B} d\vec{A}$ and it is independent of the chosen path and only depends on the chosen flux surface. So ψ_{pol} is a flux surface quantity. The flux surfaces with

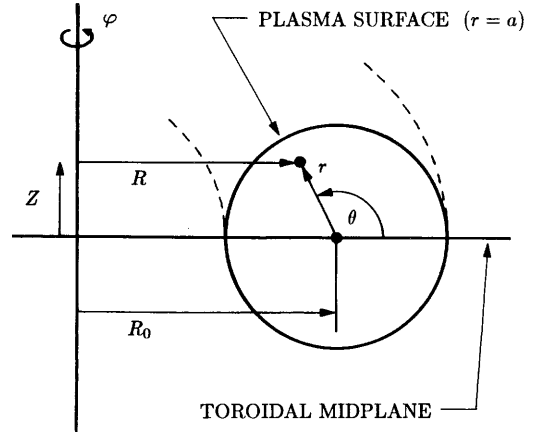


Figure 1.2 – The torus coordinate system.

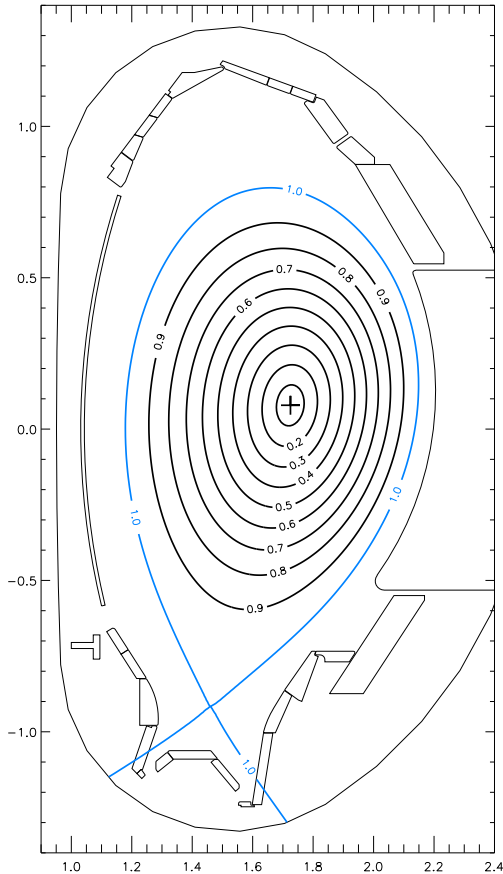


Figure 1.3 – Shows a typical poloidal cross section with the flux surfaces and their ρ_{pol} -values. The separatrix at $\rho = 1$ is plotted in blue and the magnetic axis at $\rho = 0$ is plotted with the + mark.

small (not minimal) ψ_{pol} are, in a poloidal plane, topologically circles. There are two border cases which are visualized in figure 2.2. First, the point (not surface) with minimal ψ_{pol} is called magnetic axis.

Second, for larger ψ_{pol} the flux surfaces topology in the poloidal plane is equivalent to a lemniscate¹ and an X-point is formed where the flux surface reconnects; the corresponding flux surface is called separatrix.

Finally, the position and the shape of the flux surfaces is taken into account by introducing the dimensionless *radial* flux coordinate ρ_{pol} , which is defined by

$$\rho_{pol}(R, z) = \sqrt{\frac{\psi_{pol}(R, z) - \psi_{axis}}{\psi_{separatrix} - \psi_{axis}}}. \quad (1.8)$$

The introduced *radial* flux coordinate, which is in the following denoted by ρ is constant on a flux surface and so it takes the poloidal geometry of the flux surfaces into account.

¹A lemniscate refers to a curve which is shaped like ∞ .

With figure 1.4 the straight field line angle θ^* is introduced which takes the poloidal geometry of field lines into account.

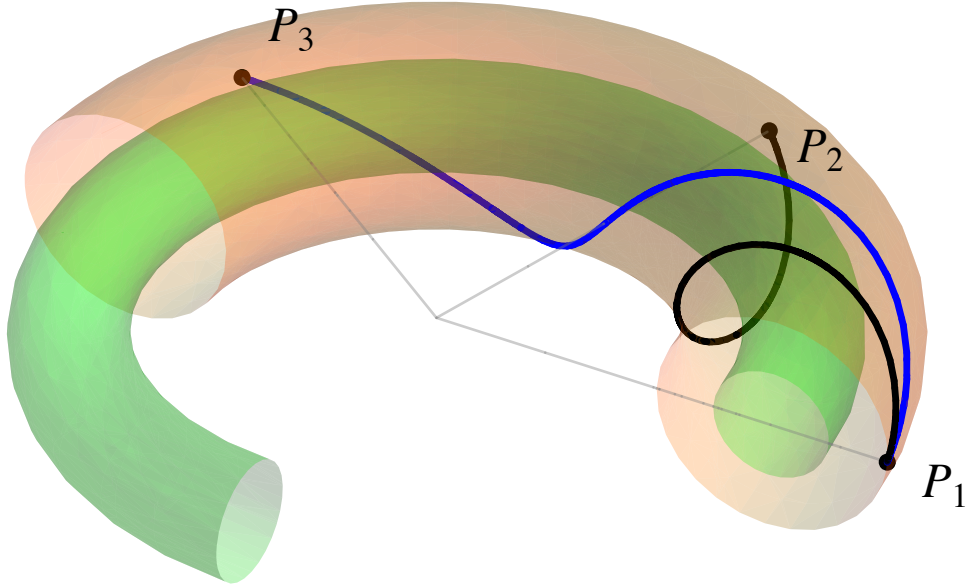


Figure 1.4 – Visualization of two flux surfaces in flux coordinates. The field line section f which is plotted with line style — . The field line plotted with line style — results from the doubling of the toroidal field B_t .

Let us consider an arbitrary flux surface inside the separatrix by choosing an arbitrary $\rho_1 \leq 1.0$ (the red surface in figure 1.4). Let f be the field line section which starts at $P_1 = (\rho_1, \theta_1 = 0, \phi_1)$ and performs one full poloidal rotation until the endpoint of the field line section which is given by the point $P_2 = (\rho_1, \theta_2 = 2\pi, \phi_2)$ is reached. On f we assign each θ -value a ϕ -value and get the function $\phi(\theta)$. We now introduce the quantity θ^* so that the function $\phi(\theta^*)$ is a linear function passing through the origin. Hence θ^* is named straight field line angle.

Based on this an expression for θ^* on the considered flux surface can be derived:

$$\frac{d\phi}{d\theta^*} = q = \text{const.} \quad (1.9)$$

Rearranging the equation and solving for θ^* leads to the following definition:

$$\theta^*(\theta) := \frac{1}{q}\phi(\theta). \quad (1.10)$$

The constant q is called safety factor and for the field line section f the safety factor is given by

$$q = \frac{\phi_2 - \phi_1}{2\pi} [6]. \quad (1.11)$$

The safety factor in equation 1.10 provides a normalization so that $\theta^*(\theta = 2\pi) = 2\pi$ is fulfilled and because of equation 1.10 $\theta^*(\theta = 0) = 0$ holds.

Although the q -value (and so the toroidal magnetic field B_t) is used in the definition 1.10, the straight field line angle θ^* is independent of the toroidal magnetic field B_t . It is shown in [33] that θ^* only depends on the radial field B_R , the vertical field B_z and the geometry of the considered flux surface. To better understand the independency on B_t let us raise B_t by a factor of 2. Then the field line in figure 1.4 with line style — transforms into the field line with line style — and the straight field line remains invariant because $1/q$ is lowered by the factor 2 and $\phi(\theta)$ is raised by a factor of 2. Note that the value of q is necessary for the reconstruction of the toroidal field line geometry. For this reconstruction the value of θ^* in a poloidal plane is not sufficient because with a given θ^* it is not possible to calculate $d\phi/d\theta^* = q$. This is because for the field line $d\phi$ is unknown. In conclusion, in θ^* there is only poloidal information about the field line structure, because θ^* only depends on the vertical field B_z and the radial field B_r and it is independent of the toroidal field B_t .

To avoid unnecessary error propagation resulting from the error on B_t and the error on q the definition 1.10 should not be used to calculate θ^* . The equation which is used to calculate θ^* reads

$$\theta^*(\theta) = 2\pi \left(\int_0^\theta \frac{1}{JR} d\theta' \right) \left(\int_0^{2\pi} \frac{1}{JR} d\theta' \right)^{-1} \quad (1.12)$$

whereas the Jacobian J is given by

$$J = \left(1 + \left(\frac{z - z_0}{R - R_0} \right)^2 \right)^{-1} \left(RB_z \frac{1}{R - R_0} - RB_r \frac{z - z_0}{(R - R_0)^2} \right) [33]. \quad (1.13)$$

In equations 1.12 and 1.13 the calculation is performed in a poloidal plane and B_z is the vertical field and B_r is the radial field. Moreover $(R(\theta), z(\theta))$ refers to the position of the considered flux surface and the magnetic axis is denoted by (R_0, z_0) . It is shown in [22] on page 20 that the definition in equation 1.10 is equivalent with the equation 1.12 which is used to calculate θ^* .

Figure 1.5 shows that lines of equal θ^* are curvilinear in real space because the poloidal field line structure is taken into account.

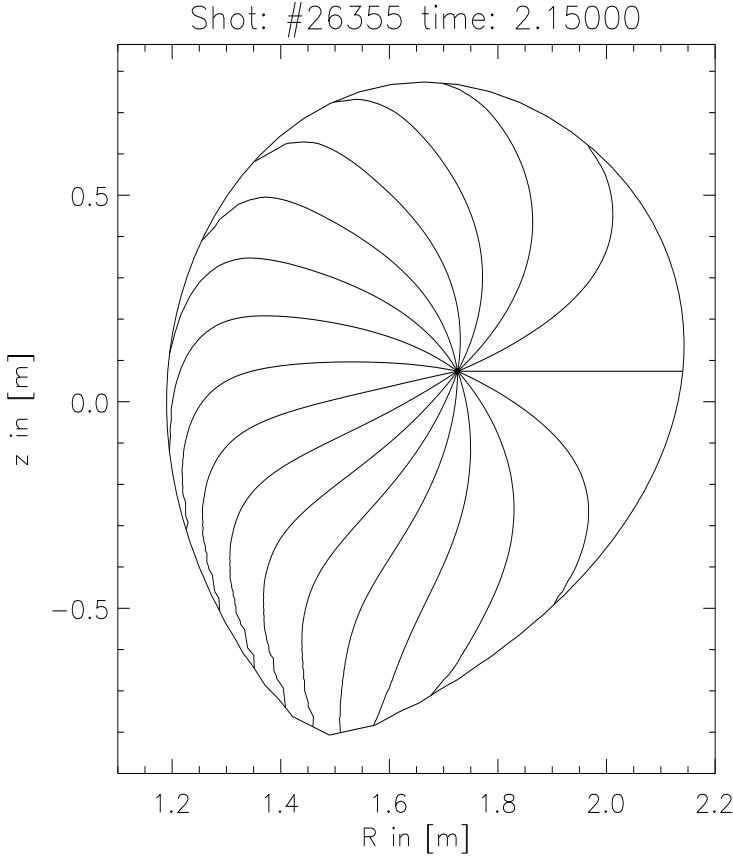


Figure 1.5 – Lines of equal θ^* in real space geometry and the flux surface with $\rho = 0.99$ are shown.

The rather mathematical definition in equation 1.10 is in the following refreshed by a physical motivation. Physical problems simplify if they are stated in the right coordinate system. The right coordinate stands out due to the fact that equations become linear. Let us assume a mode (which will be introduced in the next section) moves along the resonant flux surface with the angular velocity $\omega_{tor}(\rho)$ in toroidal direction [22]. Such a toroidal mode rotation can be induced - for example - by neutral beam injection. Let the mode rotate uniformly in toroidal direction:

$$\frac{d\phi}{dt} = \omega_{tor} = const. \quad (1.14)$$

The mode has the helical structure of the field lines. And if a mode is observed in a poloidal plane the mode appears to rotate with the poloidal rotation velocity ω_{pol} in that plane. Differentiation equation

1.10 with the respect to t and using equation 1.14, it follows that the mode rotates uniformly in θ^* :

$$\frac{d\theta^*}{dt} = \omega_{pol} = const. \quad (1.15)$$

Plasma instabilities are described using the straight field line angle θ^* considering the poloidal field line structure and this is also discussed in section 4.4.

1.2.3 Plasma instabilities and their displacement

The above introduced plasma equilibrium does not have to be stable. This is the case if a perturbation of the equilibrium does not vanish or even grows as time evolves. These plasma instabilities (also called modes) lower the total energy of the plasma and are observed often in plasma discharges.

The instabilities play a dual role in fusion experiments [44]. On the one hand, the instabilities can be instrumental to limit the impurity content in the plasma [44].

On the other hand, they can limit the operating regime of the tokamak by limiting - for example - the maximal achievable β . Furthermore instabilities can lead to disruptions which destroy the plasma confinement uncontrolled. The plasma current decay can give rise to large forces on the Tokamak vessel [5]. Instabilities enhance the level of radial particle and energy transport which decrease the quality of the confinement of the plasma. The successful ELM mitigation in AUG [45] is an example that the (fractional) understanding of the physics of plasma instabilities can lead to techniques to mitigate them.

The instabilities cause the equilibrium flux surfaces to displace. The displacement is given by the vector field $\vec{\xi}(\vec{x})$ which is illustrated in figure 1.6.

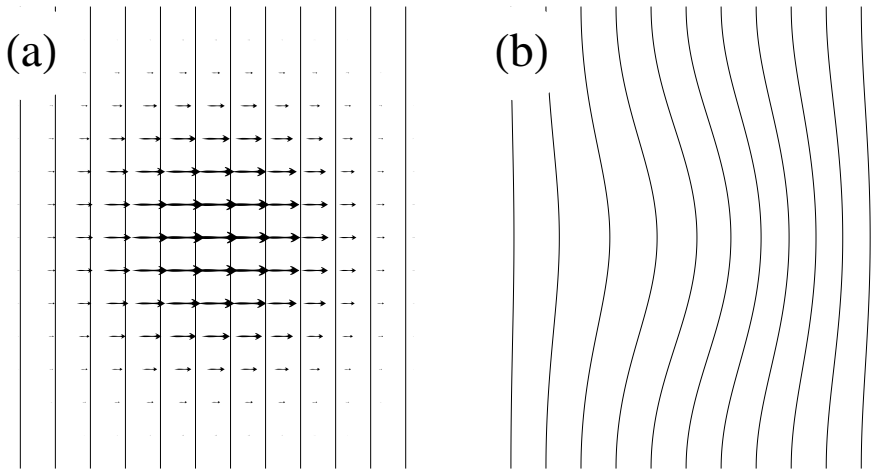


Figure 1.6 – In (a) the undisplaced flux surfaces and the displacement vector field $\vec{\xi}(\vec{x})$ are shown and in (b) the displaced flux surfaces are shown.

The vector field $\vec{\xi}$ represents the displacement of the plasma away from its equilibrium position and the force on the plasma-fluid arising from this displacement follows from a perturbation of the momentum equation 1.7 and it is given by:

$$\vec{F}(\vec{\xi}) = \rho \frac{\partial^2 \vec{\xi}}{\partial t^2} = \vec{j}_1 \times \vec{B}_0 + \vec{j}_0 \times \vec{B}_1 - \nabla p_1 \quad [15]. \quad (1.16)$$

The potential energy change resulting from this displacement $\vec{\xi}$ of the plasma is given

by

$$\delta W = -\frac{1}{2} \int \vec{\xi} \vec{F} dV. \quad (1.17)$$

In the framework of ideal MHD the total energy is conserved and the question whether an equilibrium is stable or unstable can be determined by analyzing only the sign of δW [15]. An equilibrium is stable if $\delta W \geq 0$ for all (physically allowed) $\vec{\xi}$ and it is unstable if $\delta W < 0$ for any (physically allowed) $\vec{\xi}$. If the equilibrium is not stable an instability occurs and this instability drives the plasma to another equilibrium or to an unstable situation [5].

The MHD instabilities are classified by the expansion of their boundary and by their driving source: if the plasma-vacuum interface moves from its equilibrium position the instability is called to be external and if the plasma-vacuum interface remains motionless the instability is called internal [15].

It is convenient to split up the energy functional in equation 1.17: $\delta W = \delta W_{va} + \delta W_{pl}$ where $\delta W_{va} = \int_{pl} \frac{B^2}{2\mu_0} dV$ is the perturbed magnetic energy of the vacuum region and δW_{pl} is the perturbed energy of the plasma which is given by

$$\delta W_{pl} = \frac{1}{2} \int_{pl} \left[\gamma p_0 (\vec{\nabla} \vec{\xi})^2 + \underline{(\vec{\xi} \vec{\nabla} p_0) \vec{\nabla} \vec{\xi}} + \frac{B_1^2}{\mu_0} - \underline{\vec{j}_0 (\vec{B}_1 \times \vec{\xi})} \right] dV \quad [15]. \quad (1.18)$$

Only the two underlined terms can cause the energy functional δW_{pl} to be negative and they correspond to two different sources of the instabilities: if the dominant destabilizing term is proportional to $\underline{(\vec{\xi} \vec{\nabla} p_0) \vec{\nabla} \vec{\xi}}$ the instability is pressure-driven and if the dominant driving source is proportional to $\underline{\vec{j}_0 (\vec{B}_1 \times \vec{\xi})}$ the instability is current-driven [15].

Let us concentrate on internal current driven instabilities. The most important features of the current driven instabilities can be studied in the low- β , "straight tokamak" approximation (i.e. periodic screw-pinch) considering cylindrical coordinates, in which

$$\vec{B} = B_z(r) \hat{e}_z + B_\theta \hat{e}_\theta, \quad q = \frac{r B_z}{R B_\theta} \quad \text{and} \quad \epsilon = \frac{a}{R_0} \ll 1 \quad \text{holds}$$

where ϵ is the inverse aspect ratio and a is the characteristic scale length of the minor plasma radius [23]. Within this approximation the change in potential energy due to an ideal MHD perturbation is given by

$$\delta W = \frac{W_0}{a^2} \int_0^a \left(\frac{n}{m} - \frac{1}{q} \right)^2 \left[r^2 \left(\frac{d\xi}{dr} \right)^2 + (m^2 - 1) \xi^2(r) \right] r dr \quad (1.19)$$

where ξ is the radial component of the displacement. A minimization with respect to the other two components ξ_θ and ξ_ϕ leads to the condition for incompressibility $\vec{\nabla} \vec{\xi} = 0$ [48].

For the $(m, n) = (1, 1)$ case equation 1.19 reads:

$$\delta W = \frac{W_0}{a^2} \int_0^a \left(1 - \frac{r}{a}\right)^2 r^3 \left(\frac{d\xi}{dr}\right)^2 dr \quad (1.20)$$

For $q \neq 1$ the energy functional in equation 1.20 is minimized by $\frac{d\xi}{dr} = 0$. At the resonant surface with $q = 1$ the energy functional vanishes and $\frac{d\xi}{dr} = 0$ is not necessary for the minimization of the energy functional.

Starting from the ideal MHD equations (no flux surface reconnection) and using the low- β approximation the following conditions for the displacement of the internal ideal $(m, n) = (1, 1)$ kink are derived: the plasma is displaced incompressibly $\vec{\nabla} \cdot \vec{\xi} = 0$ and inside the $q = 1$ region $\frac{d\xi_\rho}{dr} = 0$ holds for the radial displacement ξ_ρ . This leads to a constant rigid displacement inside the $q = 1$ region and because this instability *kinks* the plasma out of its equilibrium position it is called kink. Since the internal kink is considered there is an undisplaced flux surface inside the plasma and for all flux surfaces outside of the undisplaced flux surface the displacement also vanishes.

The $m = 1$ kink plays a special role because only the $m = 1$ kink mode has the topology of a torus. The $m \geq 2$ kinks are not homeomorphic to a torus. Furthermore the $m = 1$ kink is unstable and the $m \geq 2$ kinks are commonly stable (for very high pressure or/and current gradients also these modes can get unstable).

The kink-instability is an often observed instability in the AUG Tokamak in conventional scenarios and large scale kink modes limit the operation regime of the Tokamak [5] [22] [27]. Furthermore the kink-instability displaces a rather big area of the plasma and the value of the displacement is big compared to other plasma instabilities, therefore the kink mode is well suitable for investigations using the srx diagnostic and its virtual counterpart which are introduced in section 2 and 3 [46].

1.3 Motivation and Outline

Usually the searched quantity - in this case the emissivity - is calculated by solving the equations directly but for the case of the srx diagnostics this means the following. The signals of the ~ 200 channels result from the convolution of the emissivity $e_0(\vec{x})$ with the point response function of the detector over the VOS:

$$S_i = \int_{\vec{x} \in VOS_i} \Omega(\vec{x}) e(\vec{x}) dV \text{ and } i = 1, \dots, \sim 200. \quad (1.21)$$

In order to calculate the spatial emissivity distribution $e(\vec{x})$ these ~ 200 equations must be solved for $e(\vec{x})$. This is the ill-posed problem of tomography [13] and in plasma physics sophisticated algorithms are developed in order to solve it.

In this thesis a different approach is considered to quantify the emissivity: a virtual diagnostics in combination with a model for the emissivity is used.

In the following the two approaches are briefly compared. For a tomographic inversion no model of emissivity is needed. This can be advantageous if the model is unknown like for the emissivity of the bolometer diagnostics. But the use of a model of emissivity is very useful because important additional information like the displacement can be gained on the way. Using tomographic inversion the final result is the emissivity distribution $e(\vec{x}, t)$ and if important additional information like the displacement is needed it must be calculated starting from $e(\vec{x}, t)$.

There is prior information about the detector like the three-dimensional geometry of the VOS and the point response function. Furthermore there is quasi prior information about the spatial emissivity distribution of the plasma. For example it can be assumed that the emissivity is displaced accordingly to the mode numbers (m, n) .

Referring to [31] and to [32] it is possible but rather complicated to consider the (quasi) prior information in rotation tomography. In this thesis the (quasi) prior information is considered as explained in section 3.1 and 4.

In conclusion, using the virtual diagnostics in combination with a model for the search quantity has the advantage (compared to tomography), that the implementation of (quasi) prior information is straight forward. With tomography it is only possible to derive the spatial emissivity distribution. It is discussed in the following that the virtual diagnostics is not limited to this purpose.

With a virtual diagnostics in combination with a model for the search quantity the following goals can be achieved:

- It is possible to quantify the search quantity. In this thesis the search quantity is the emissivity and the perturbation of it which corresponds to the magnetic structure of plasma instabilities. The described approach is applied in section 6.1.
- With the help of the virtual diagnostics it is possible to gain knowledge about the features and the properties of the real diagnostics. In this thesis this aspect is touched in section 5.3.
- It is also possible to investigate the optimal position, alignment and dimensions of the pinhole-detector-array in order to measure certain predefined effects. The method is used to design a new diagnostics and this objective is not followed up in this thesis.
- With the help of the virtual diagnostics a validation of data analysis tools is possible.
- For this thesis most important, working with a virtual diagnostics in combination with a model for the measuring quantity an investigation of idealized examples is possible. With this method it is possible to isolate effects from disturbing influences and investigate isolated effects under well defined conditions. The signal depends on many parameters and the virtual allows to vary these parameters specifically. By varying only one parameter and setting all other parameters fixed the pure impact of this variation can be investigated and new insight can be gained. There are cases where the interpretation of the raw data is impossible. With the help of the virtual one can get an idea of the effects which play a role and one can investigate the impact of the effect on the signals. This helps to understand the functionality of the diagnostics and also the physics of plasma.

Outline

The purpose of this thesis was to design and implement a virtual sxr diagnostic and a model for the mode displaced emissivity. This thesis is organized as follows: first in section 1 a short introduction aiming to explain the motivation for fusion research, the fundamentals of a Tokamak and introducing the kink MHD instability is given.

After the real sxr diagnostics is described in section 2, in section 3 the approach and the implementation of its virtual counterpart is explained.

Section 4 derives a model for mode displaced plasma considering the full poloidal displacement and compares the results with two approximations used in the literature.

In section 5 idealized examples of kink modes are defined and under well known conditions the impact on the simulated signals is investigated.

Section 6 applies the simulation to observed kink modes.

2 The soft x-ray diagnostics at AUG and the quantity emissivity

In this section the main properties of the soft x-ray diagnostics at AUG and its measuring quantity, the emissivity, are introduced (a more detailed description is given in [12]).

An important plasma diagnostics in current fusion research are soft x-ray cameras which measure the srx radiation. This is because the analysis of srx diagnostics signals provides information about important plasma properties for example plasma instabilities, equilibrium configuration and impurity transport.

2.1 The pinhole detector array and its geometry

At AUG the srx cameras consist of semiconductor diode arrays with a pinhole geometry as visualized in figure 2.1. Simplifying the notation several pinhole-diode-arrays at the same poloidal position and at roughly the same toroidal position are referred to a camera labeled with the letters F, G, H, I, J, K, L and M.

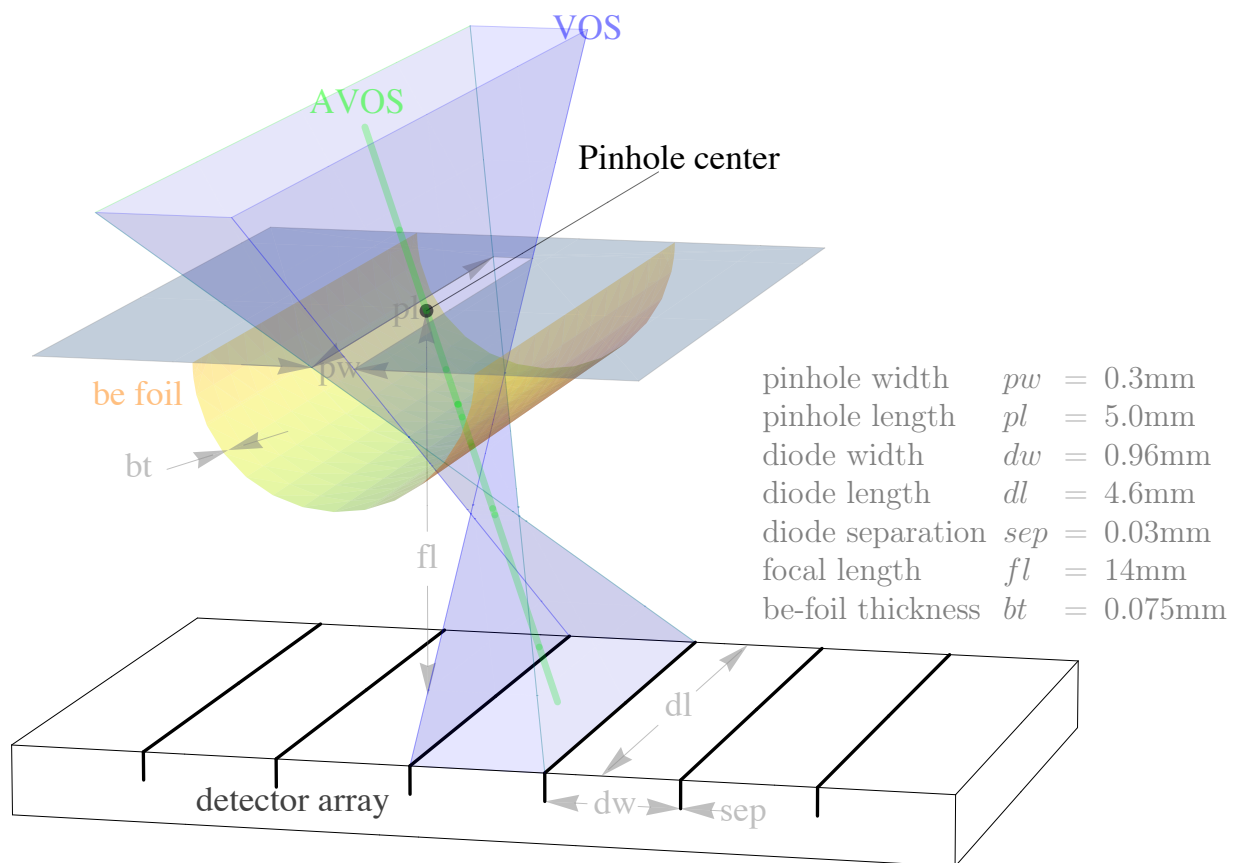


Figure 2.1 – The geometry and the dimensions of the pinhole-detector-array arrangement.

The outer border of one diode of the detector-array and the pinhole span a pyramid-like volume. This volume is called volume of sight (VOS) and it is plotted in figure 2.1 in blue. The line connecting the center of the pinhole and the center of the diode is called axis of the VOS (AVOS) and it is plotted in figure 2.1 in green. The radiation inside the VOS contributes to the measured signal and the origin of the radiation is discussed in section 2.3.

According to the data sheet of the detector (centronic LD35-5T) [20] it is sensitive to radiation with lower energy (for example visible light which is also emitted by the plasma). In order to block low energy photons up to around 1 keV from the detectors a beryllium-foil is installed between every pinhole and the detector array [12]. The beryllium foil has a cylindrical shape such that the effective thickness is approximately equal for every channel of the diode array.

The sxr diagnostics is a passive diagnostics in the sense, that it does not affect the plasma. The diagnostics has been designed to have a high time resolution (in order to resolve fast plasma instabilities) and a high number of channels (in order to provide a good spatial resolution). The AUG sxr diagnostics consists of 8 cameras which provide ~ 200 independent channels.

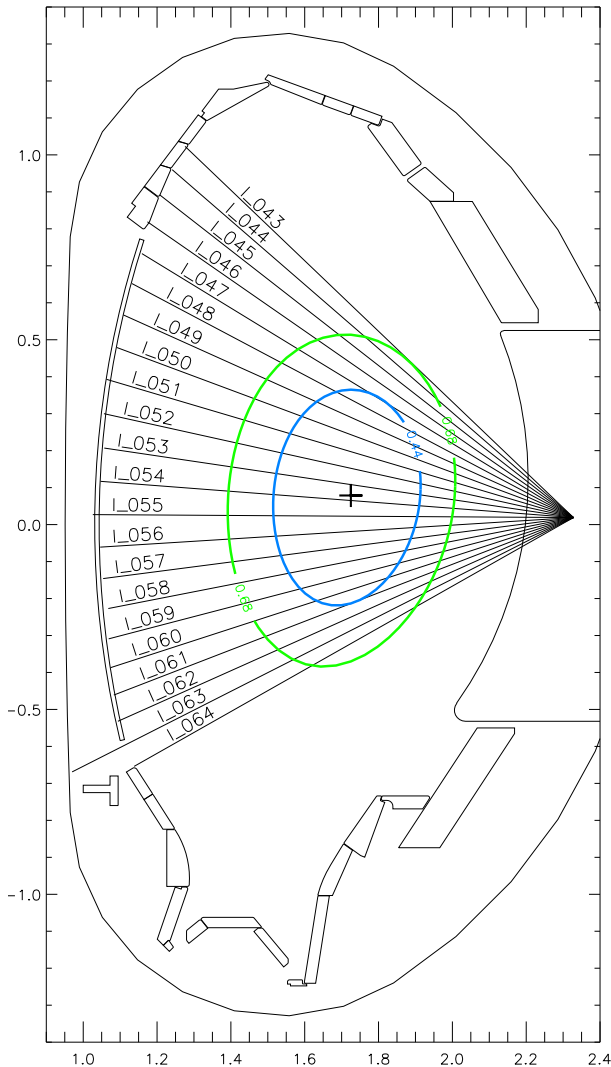


Figure 2.2 – Visualization of the AVOS of the I-camera and of two flux surfaces. The magnetic axis is plotted with +. The value of the x-axis is R in [m] and for the y-axis it is z in [m].

In figure 2.2 the AVOS and the corresponding channel names of the I-camera are visualized. A visualization of all channels is given in the appendix C. In figure 2.2 also the two flux surfaces with $\rho_1 = 0.44$ and $\rho_2 = 0.68$ are plotted. The AVOS of the channel I_{043} is tangent to the flux surface ρ_2 and the two AVOS of the channels I_{047} and I_{061} are tangent to the flux surface ρ_1 . The emissivity $e_0(\rho)$ and the displacement $\xi(\rho)$ is plotted over ρ , therefore it is convenient to label also the channels with the corresponding ρ -value of the flux surface on which the AVOS tangents. With the following convention it is possible to distinguish the channels which tangent the same flux surface (for this example the channels I_{047} and I_{061}). For the channels of the I camera, the channels which tangent the flux surface below the magnetic axis are labeled with $+\rho$ and those which tangent the flux surface above the magnetic axis are labeled with $-\rho$. For the other cameras similar conventions are defined.

By modifying the pinhole dimension and its position with respect to the detector the optimal compromise between a maximal signal-to-noise ratio (larger the larger the VOS) and a maximal spatial resolution (larger the smaller the VOS and larger the smaller the out-fanning of the VOS) can be found.

The spectral response (and so the spectral range) is defined by the semiconductor diode and by the thickness of the Beryllium-foil.

In the following two peculiarities of the sxr diagnostics are discussed. First it provides a non-local measurement of the emissivity (introduced in section 2.4) because the signal results of the convolution of the emissivity $e_0(\vec{x})$ with the point response function of the detector over the VOS as described in section 3.1. Second the measured quantity is the emissivity which contains no information of the energy distribution of the radiation. It is not possible to unfold this information because every channel has nearly the same spectral response (the spectral response depends on the angle of incidence of the radiation on the detector surface [17]). Which leads to a slightly different spectral response for different diodes.

2.2 Pinhole-camera-tile arrangement

The VOS of the cameras F,G, L and M is not only limited by the detector and the

| Camera | $d [cm]$ | $\gamma [^\circ]$ | $b [cm]$ |
|--------|----------|-------------------|----------|
| F | 3.4 | 0.0 | 1.2 |
| G | 3.4 | 0.0 | 1.17 |
| L | 4.0 | 36.9 | 0.64 |
| M | 3.6 | -16.75 | 0.54 |

Table 1 - Orientation and Position of tiles.

pinhole area but also by tiles which protect the vessel from the plasma. The geometry of the detector-pinhole-tile arrangement is visualized in figure 2.3. The positions and orientations of the tiles are summarized in table 1. The length d is the distance between the pinhole center and the tile surface in z-direction. The angle γ is the angle between the normal vector of the tiles surface plotted in yellow in figure 2.3 and the vector z plotted in blue. The length (in toroidal direction) of the gap between the tiles is denoted by b . The vector z points approximately toward the plasma center and a positive (negative) angle γ corresponds to a tilt in clockwise (counterclockwise) direction considering a poloidal plane like in figure 2.2.

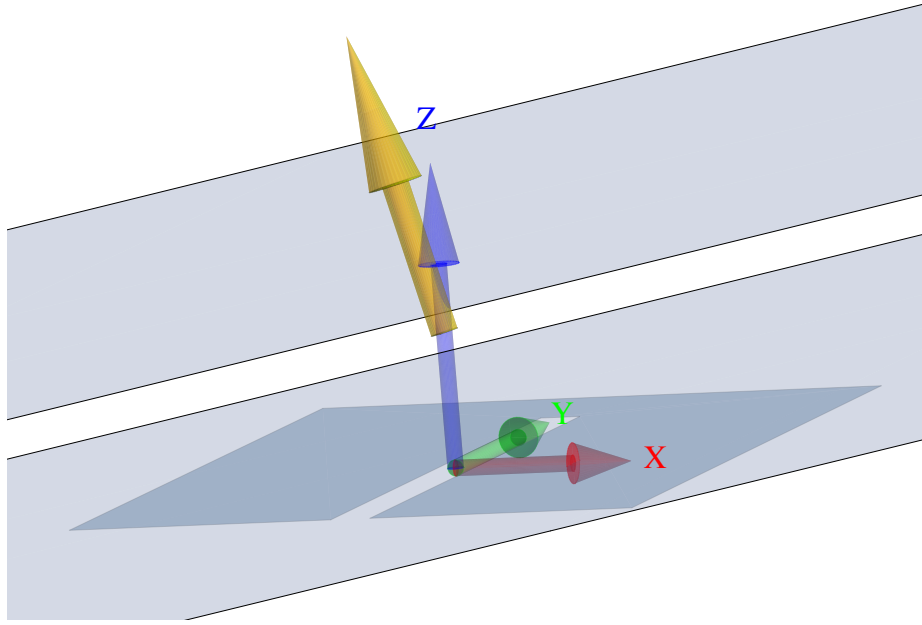


Figure 2.3 – Geometry of the tiles limiting the VOS of the cameras F, G, L and M.

2.3 Creation mechanisms of soft x-ray radiation

Electromagnetic radiation in the spectral region from approximately 1keV to 20keV is called soft x-ray (sxr) radiation. In plasma discharges it results from three different creation mechanisms. Considering the scattering of an electron on an atom or nucleus the mechanisms can be characterized by the initial and the final state of the electron: free-free bremsstrahlung, free-bound recombination radiation and bound-bound line radiation. The last process results in line radiation and it is due to impurities with high nuclei-charge which are not completely ionized because the plasma temperature is not high enough. It is important to consider the line radiation because there are plasma discharges in which the power of the line radiation overcomes the Bremsstrahlung. In most discharges the contribution of recombination radiation can be neglected in the core plasma [26].

The information of the spectral distribution of the radiation is given by the power spectral density dP/dE of the plasma and it depends on the following physical quantities:

$$n_e, T_e, Z_{eff}, n_{imp1}, n_{imp2}, \dots \quad (2.1)$$

where $n_{imp1}, n_{imp2}, \dots$ are the densities of all impurities and $Z_{eff} = \sum_i n_i Z_i^2 / \sum_i n_i Z_i$ is the effective nuclear charge.

The measured quantity of the sxr diagnostics is the emissivity and in the next section it is derived from the power spectral density dP/dE .

2.4 The emissivity

The response of electromagnetic radiation on the detector depends on the energy of the radiation, because the signal depends on the design of the solid state detector and the thickness of the beryllium-filter. A measure for this response is the spectral response function $f(E)$.

Let dP/dE be the power spectral density of the plasma and let $f(E)$ be the spectral response function of the detector-beryllium-filter-arrangement. The emissivity is given by:

$$e(\vec{x}) = \int_0^\infty f(E) \frac{dP(\vec{x})}{dE} dE \quad \text{with the unit } [Wm^{-3}sr^{-1}] \text{ [12]}. \quad (2.2)$$

In this thesis the spatial emissivity distribution is modeled directly without considering the physical source of it. This is because the power spectral density depends on many physical quantities presented in 2.1 and the spatial distributions of the impurity densities not well known. Furthermore the emissivity depends on the spectral response function of the detector which is not precisely known. The complexity of a bottom up calculation of the emissivity limits the possibilities of comparing and crosschecking with other measured quantities. So the uncertainty of the spectral response and the uncertainty of the power spectral density are passed to the single uncertainty of the emissivity.

In this thesis the emissivity is considered to be constant on flux surfaces (which are displaced as time evolves) and in the following the quality of this consideration is discussed. The constancy of the emissivity on flux surfaces depends on the constancy of the physical quantities given in 2.1. For most conventional tokamak scenarios at AUG we consider n_e and the electron temperature T_e to be constant on flux surfaces. The constancy of Z_{eff} on a flux surface depends on the constancy of the impurity densities. And the constancy of the impurity density on a flux surface depends on the toroidal angular velocity ω_t of the plasma because in highly rotating plasmas the centrifugal-force forces the heavy impurity ions into the LFS [39] and there are also up/down asymmetries of the impurity density observed [40] [41] (compare section 6.1).

Although the possible discrepancy of the constancy of the emissivity on flux surfaces, as discussed in [38], is known, in this thesis the emissivity is considered to be constant on flux surfaces (compare section 6.3).

All the emissivity inside the VOS which is introduced in this section contributes to the measured signal. An analytical formula for the signal will be derived in section 3.1.

3 The virtual soft x-ray diagnostics

In this section the implantation of the virtual sxr diagnostics is explained starting from a derived analytical formula for the signal considering the full three-dimensional geometry.

3.1 An analytical formula for the signal

Starting from the spatial emissivity distribution $e(\vec{x})$ (section 2.4) in this section an equation for the signal of a channel is introduced.

In the virtual soft x-ray diagnostics which are developed in [21] and [42] the spreading of the detector and of the pinhole are neglected. This leads to the approximation, that the signal results from the integration over a line of sight which is visualized in figure 3.1 (a).

In reality the diode and the pinhole has a spread and the measured signal result from the convolution of the emissivity $e_0(\vec{x})$ with the point response function of the detector over the VOS which will be explained in this section. This VOS is a pyramid-like volume which is visualized in figure 3.1 (b). In this thesis the full geometry of the pinhole-detector-array arrangement is considered like in [50]. For the cameras F,G,L and M the situation is even more complex because the VOS is additionally limited by tiles which protect the vessel from the hot plasma. This pinhole-detector-array-tile arrangement is considered in section 3.3.

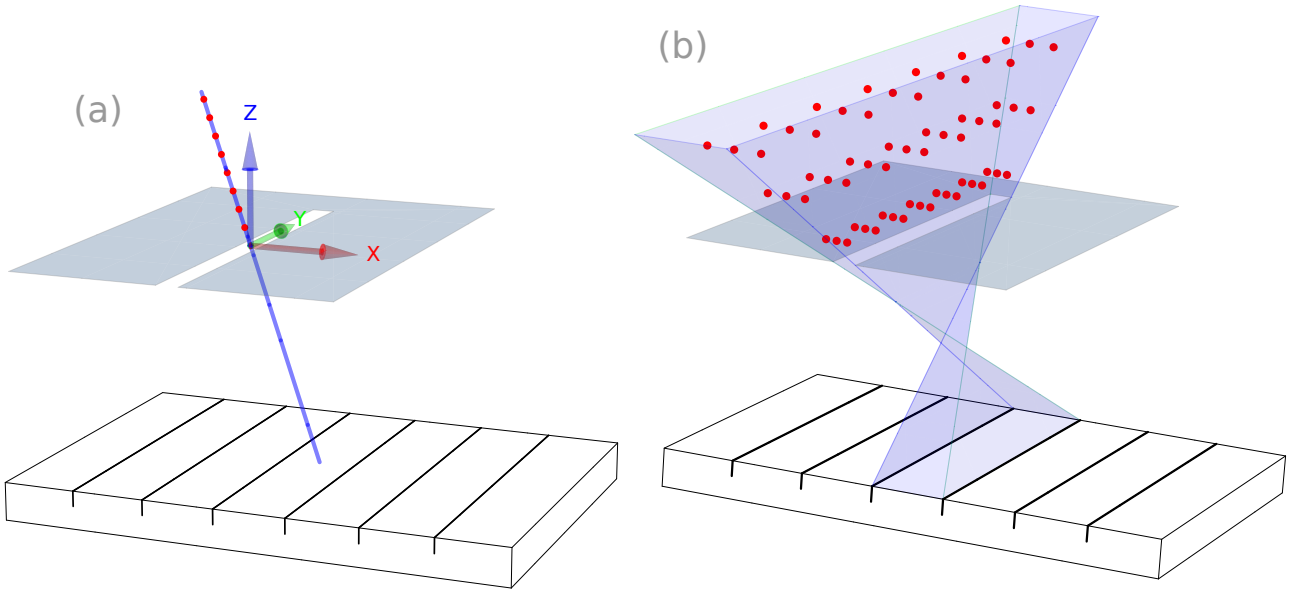


Figure 3.1 – A visualization of the line of sight (a) and the volume of sight (b) approach. The grid-points of integration are plotted with the plot mark \bullet . In (a) the camera coordinate system is defined.

The grid-points of integration which are plotted in figure 3.1 are defined in the camera

coordinate system which is also visualized in this figure. The numerics will be explained in section 3.2.

Now we change the perspective by considering a single point source of (soft x-ray) radiation inside the VOS. Let the point source radiate an isotropic emissivity per steradian of e_{point} with the unit $[\text{W sr}^{-1}]$ and it is visualized in figure 3.2 by the green dot (●).

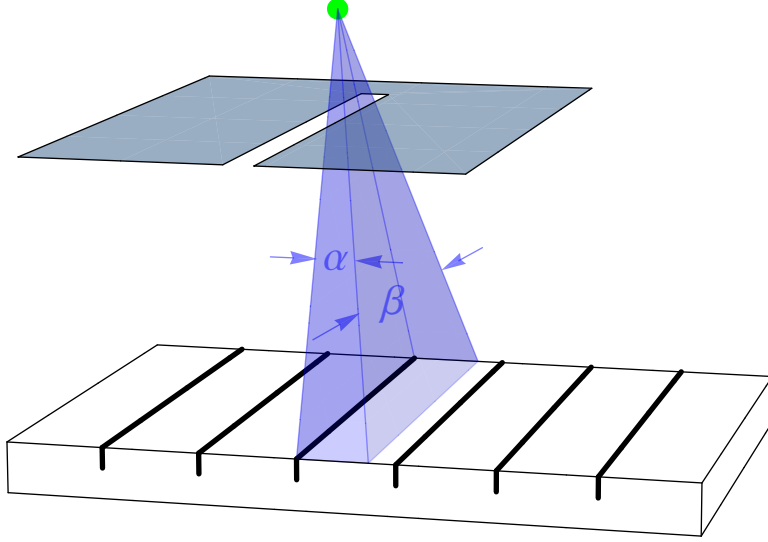


Figure 3.2 – Only the radiation from the point source (●) inside the blue pyramid reaches the detector-chip because radiation with a different direction either propagates aside the chip-area or is blocked by the pinhole.

The impact of this point source on the signal depends on the position of the point source in the VOS because the radiation power which is emitted onto the detector area is proportional to the solid angle Ω subtended by the detector-area to the point source. The solid angle Ω is given by

$$\Omega = 4 \arcsin(\sin(\alpha/2) \sin(\beta/2)) \text{ with the unit [sr] [10].} \quad (3.1)$$

whereas the angles α and β are defined in figure 3.2. The power which is emitted from the point source onto the detector is given by $e_{point}\Omega$ with the unit [W]; it is proportional to the solid angle Ω which depends on the position \vec{x} of the point source.

We now turn to continuously in space defined emissivity density per steradian $e(\vec{x})$ with the unit $[\text{W m}^{-3}\text{sr}^{-1}]$. Then the signal resulting from the emissivity in the volume dV is

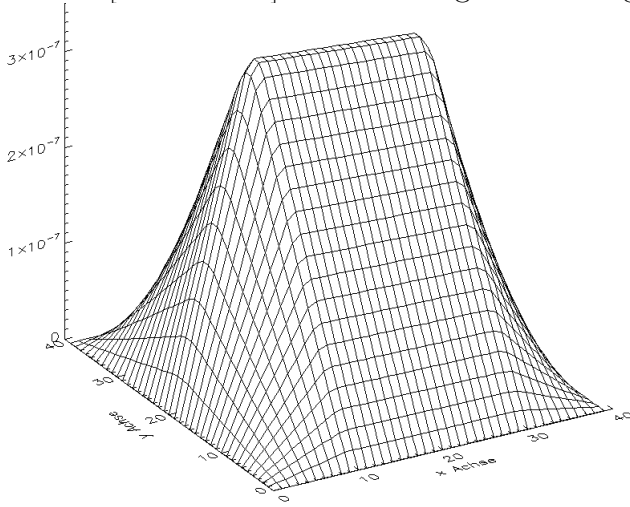


Figure 3.3 – The solid angle of the *seen* detector area (point response function) for different positions in the x-y plane at $z = 2.3$ cm for the channel J_079 . The axes correspond to the number of one grid point.

given by $e(\vec{x})\Omega(\vec{x})dV$ whereas the solid angle $\Omega(\vec{x})$ is a continuously in space defined weight. This weight is also called apparatus function or point response function [11] and in figure 3.3 the value of it is plotted for the channel J_079 in the x-y plane for $z=2.3$ cm. In the figure the camera coordinate system is used. Note that the solid angle at the border of the VOS is zero because emissivity in this locations is regarded to be totally blocked by the pinhole. A deviation can occur, because in this thesis the material in which the pinhole is, is considered to have zero thickness and is considered to be totally absorbing. These ideal assumptions are of course not fulfilled in reality.

Since the electromagnetic radiation is not coherent and the pinhole is very big compared to the wavelength, wave-effects like interference can be neglected. The plasma is optically thin in the region of visible light [30] and it is a reasonable assumption that this is also true in the srx region; so the absorption of radiation by the plasma is neglected.

The total power S resulting from the emissivity density per steradian $e(\vec{x})$ which is emitted onto a detector-chip is given by the following volume integration over the VOS

$$S = \int_{\vec{x} \in \text{VOS}} e(\vec{x})\Omega(\vec{x})dV. \quad (3.2)$$

and the unit of the simulated signal S is W.

Note that there are detector properties which are not taken into account. Defining the emissivity in equation 2.2 it is assumed, that the spectral response function $f(E)$ is independent on the angle of incidence of the radiation. But it is discussed in [17] that the solid state detector consists of doped layers of semiconductors and the signal depends on the effective thickness of the layers which is larger the steeper the angle of incidence is. Because of the following reasons the effect is rather small. First, the diagnostics is designed to have a minimal steepness of the angles of incidence. Furthermore the radiation with low energy is absorbed by the beryllium-filter-foil in an angle-independent manner, because the filter thickness is approximately equal for every channel. The effective thickness of the active detection layer of the diode only slightly affects high energetic photons above $\approx 6\text{keV}$, so mainly the signals of the diodes observing the core plasma are reduced. Further effects can occur because of variations in the thickness of the beryllium foil.

3.2 Numerics of the camera simulation

It will be discussed in chapter 4 that the emissivity $e(\vec{x})$ is (finally) defined in flux coordinates (ρ, θ^*, ϕ) . Since the flux coordinates are calculated for discrete points in real space it is necessary to carry out the volume integration of equation 3.2 numerically over a discrete grid.

The one dimensional midpoint-rule is given by

$$\int_{x_{min}}^{x_{max}} f(x)dx \approx \sum_{i=1}^n \Delta x f(x_i) \quad \text{with } x_i = x_{min} + \Delta x(i - 1/2), \quad (3.3)$$

whereas the interval $[x_{min}, x_{max}]$ is divided into n equal subintervals of length $\Delta x = (x_{max} - x_{min})/n$ [9].

For one channel the signal S is calculated with the three dimensional midpoint-rule:

$$S = \int_{\vec{x} \in VOS} \Omega(\vec{x}) e(\vec{x}) dV \quad (3.4)$$

$$= \int_{z_{min}}^{z_{max}} \int_{x_{min}(z)}^{x_{max}(z)} \int_{y_{min}(z)}^{y_{max}(z)} \Omega(\vec{x}) e(\vec{x}) dx dy dz \quad (3.5)$$

$$\approx \sum_{k=1}^{n_z} \sum_{i=1}^{n_x} \sum_{j=1}^{n_y} \Delta V_{i,j,k} \Omega(\vec{x}_{i,j,k}) e(\vec{x}_{i,j,k}), \quad (3.6)$$

where $\vec{x}_{i,j,k} = (x_i, y_j, z_k)$ and where $\Delta V_{i,j,k}$ is the volume element of the grid point (x_i, y_j, z_k) . These volume elements are given by the geometry of the integration grid, which can be chosen arbitrarily. In the used implementation the grid is chosen by the following manner. In every x-y plane there is the same user defined number of grid points which are equidistant in x-direction and equidistant in y-direction. All the x-y planes are equidistant and have the same user defined distance Δz ; the grid is visualized in figure 3.4.

Because the equation 3.2 is discretized by choosing a grid, numerical limitations occur. The bigger the Volume $\Delta V_{i,j,k}$ the bigger is the deviation between the calculated signal and the true signal, and the smaller the Volume $\Delta V_{i,j,k}$ the higher is the number of grid points and the longer is the time needed for the calculation. It is necessary to find a compromise between a sufficient accuracy of the calculated signal and an acceptable calculation time. This compromise depends on the sizes of structures in the emissivity $e(\vec{x})$.

With the emissivity being time dependent also the signals depend on time and in the following the numerics of the amplitude and phase calculation is explained. In order to calculate the amplitude and the phase of the time dependent signal a time window with the length of a multiple of one single period of the mode is chosen and within this time window a time series of signals is calculated. This procedure increases the calculation time (because many signals are calculated) but the procedure is necessary, since the signals are in general not harmonic in time as discussed in section 4.4 and in appendix

A. The amplitudes and the phases of the time series of signals is calculated using a standard FFT implementation. The same routine is used to calculate the amplitudes and the phases of the measured signals.

In section 6.1 it is pointed out, that a fit routine is used in order to find the emissivity function $e_0(\rho)$ for which the measured and the simulated signals fit best. For this purpose a numerical minimizer, in this case a standard implementation of the downhill simplex method of Nelder and Mead, is used [14]. The parameters of the displacement function $(\rho_1, \rho_2, \zeta_0, \rho)$ are varied manually until measured and simulated amplitudes fit best. The parameters are not included in the fitting routine because the amplitudes and the phases are calculated using time traces which takes a much longer calculation time than one single time step. This limitation can be removed by parallelizing the code.

We now turn to a remark about the numerics of the θ^* -calculation. The libkk-routine `kkEQqFL` [8] calculates, based on equations 1.12 and 1.13, an array $(\theta_1^*, \theta_2^*, \theta_3^* \dots, \theta_n^*)$ for input points $(\theta_1, \theta_2, \theta_3 \dots, \theta_n)$ which lie on one single flux surface. Since generally every grid point inside the VOS has a different ρ -value it would be necessary to call the `kkEQqFL`-routine for every grid-point which takes about 5 minutes. To speed up the calculation-time a numerical routine has been developed which provides a fast calculation of $(\theta_1^*, \theta_2^*, \theta_3^* \dots, \theta_n^*)$ for points which are not on the same flux surface. This numerical routine is based on the equations 1.12 and 1.13 just like the libkk-routine.

3.3 Test of the camera simulation

The correctness of the implementation of the numerical signal calculation in equation 3.2 is checked by the following two steps. First the correctness of the geometry of the grid of integration is checked. The geometry of the VOS of the channels is implemented a second time using the software MATHEMATICA. With this independently programmed representation of the VOS geometry the VOS for channel I_{055} is visualized in figure 3.4 in the color yellow.

For this example the border points of a volume element $V_{i,j,k}$ are calculated with the camera simulation which is implemented in the IDL programming language. The border points and not the midpoints which are described in equation 3.6 are calculated because only the border points correspond to the border of the VOS. The calculated coordinates of the border grid points are stored in a file which is loaded into the MATHEMATICA visualization described above. Figure 3.4 shows that the border grid points plotted with plot mark \bullet correspond to the independently implemented VOS in yellow. Therefore the correctness of the grid point calculation is verified.

Second the correctness of the point response function is checked. The signals resulting from an emissivity profile $e_0(\rho)$ are normalized to the signal of the central channel. Then the geometrical calibration factor (section 4.1) is also normalized to the central channel. By comparing the normalized calibration factors with the normalized signals the correctness of the point response function is checked.

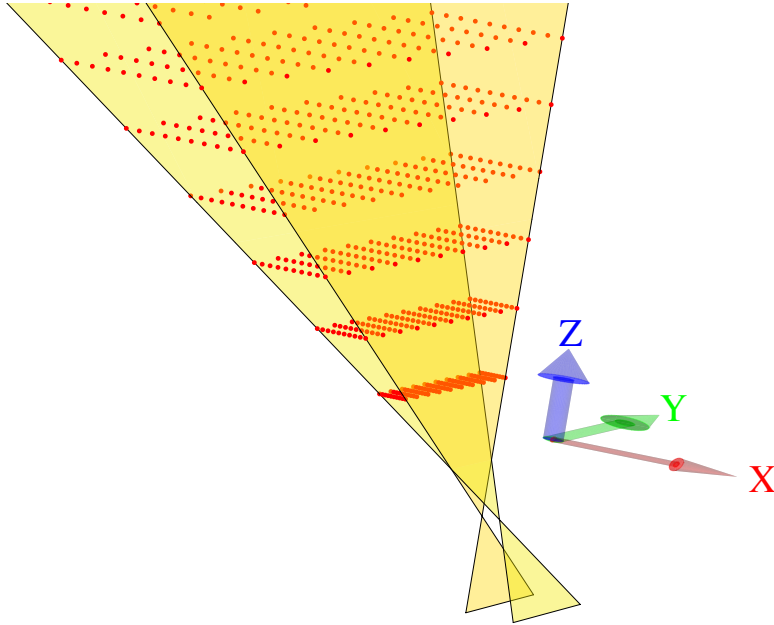


Figure 3.4 – Visualization of the grid points ● of the channel I_{055} in the camera coordinate system.

For the VOS approach the full three-dimensional geometry is considered. This is advantageous because all the emissivity (with its structures) inside the VOS contributes realistically to the signal. For the LOS approach this described feature does not hold.

By changing the three-dimensional geometry of the VOS it is possible to test whether an effect is influenced by the geometry of the VOS (see section 5.3).

The pinhole-tile-detector-array geometry

Figure 3.5 shows the grid points of the channel L_021 with a ● mark. The VOS which results by neglecting the tile is visualized in yellow and its spread in y -direction is much larger than the gap in the tile. So the actually used VOS with the grid points is limited by the tile in y -direction.

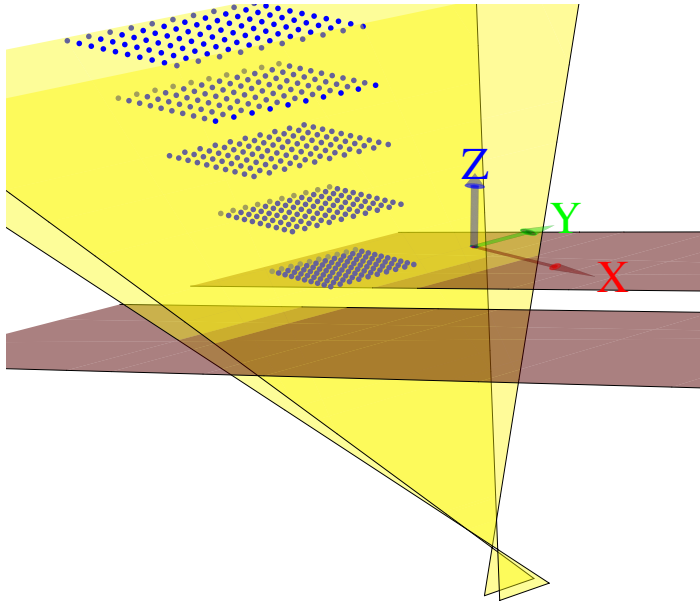


Figure 3.5 – Visualization of the grid points ● of the channel L_021 in the camera coordinate system. The VOS is limited in $\pm y$ -direction by a tile.

There are also limiting tiles for the cameras M, G and F. The full three-dimensional geometry of the VOS is considered. The tiles limit the VOS in $\pm y$ -direction and in the torus this is the toroidal direction. For a channel with a VOS which is limited by a tile the geometry of the VOS and the point response function is more complex.

For a point inside the VOS the solid angle (point response function) can be limited in $+y$ -direction by two different limitations: tile-limitation or pinhole-limitation. Because there is a limitation in $+y$ and in $-y$ -direction, it is considered, that there are 4 different limitation scenarios for one grid point and the smallest solid angle is realized.

itiation in $+y$ and in $-y$ -direction, it is considered, that there are 4 different limitation scenarios for one grid point and the smallest solid angle is realized.

4 Models of emissivity

In order to calculate the simulated camera signal for one point in time the emissivity is given by an emissivity function $e(\rho, \theta, \phi)$ for that time point. The emissivity function is defined for every point (ρ, θ, ϕ) inside the separatrix and the emissivity outside the separatrix is assumed to be zero. This is a good assumption since the electron temperature is very low therefore almost no photon above the energy of 1keV are emitted, so the radiation which contributes to the sxr signal can be neglected outside the separatrix. In the following sections emissivity functions are introduced and discussed.

4.1 Emissivity as a flux surface quantity

Due to plasma instabilities the flux surfaces - with constant emissivity - are displaced as time evolves (this is further explained in section 4.2). Let us consider the time average over a time window with the length of a multiple (for example 3) of one single period of the mode of the emissivity to be constant on an equilibrium flux surface. With this approximation the time-averaged emissivity is an equilibrium flux surface quantity and the emissivity is given by:

$$e = e(\rho).$$

Here, the function $e(\rho)$ is considered to be a cubic spline with 11 nodes at $\rho_i = i/10$ with $i = 0, 1, \dots, 10$. The emissivity $e(\rho)$ should be differentiable everywhere (because the derivative $de/d\rho$ is calculated for example in equation 4.25). Because (θ, ρ) is a polar coordinate system the differentiability of $e(\rho)$ at $\rho = 0$ is provided by choosing $de/d\rho = 0$ at $\rho = 0$. With the virtual sxr diagnostics it is possible to reconstruct the emissivity profile $e(\rho)$. The 11 parameters of the cubic spline are varied with the algorithm described in section 3.2 until the simulated signals and the measured signals fit best according to the residual sum of squares (RSS) measure as explained in section 6. In figure 4.1 an example of a reconstructed emissivity profile $e(\rho)$ is presented.

shot # 26355 time = 2.15000

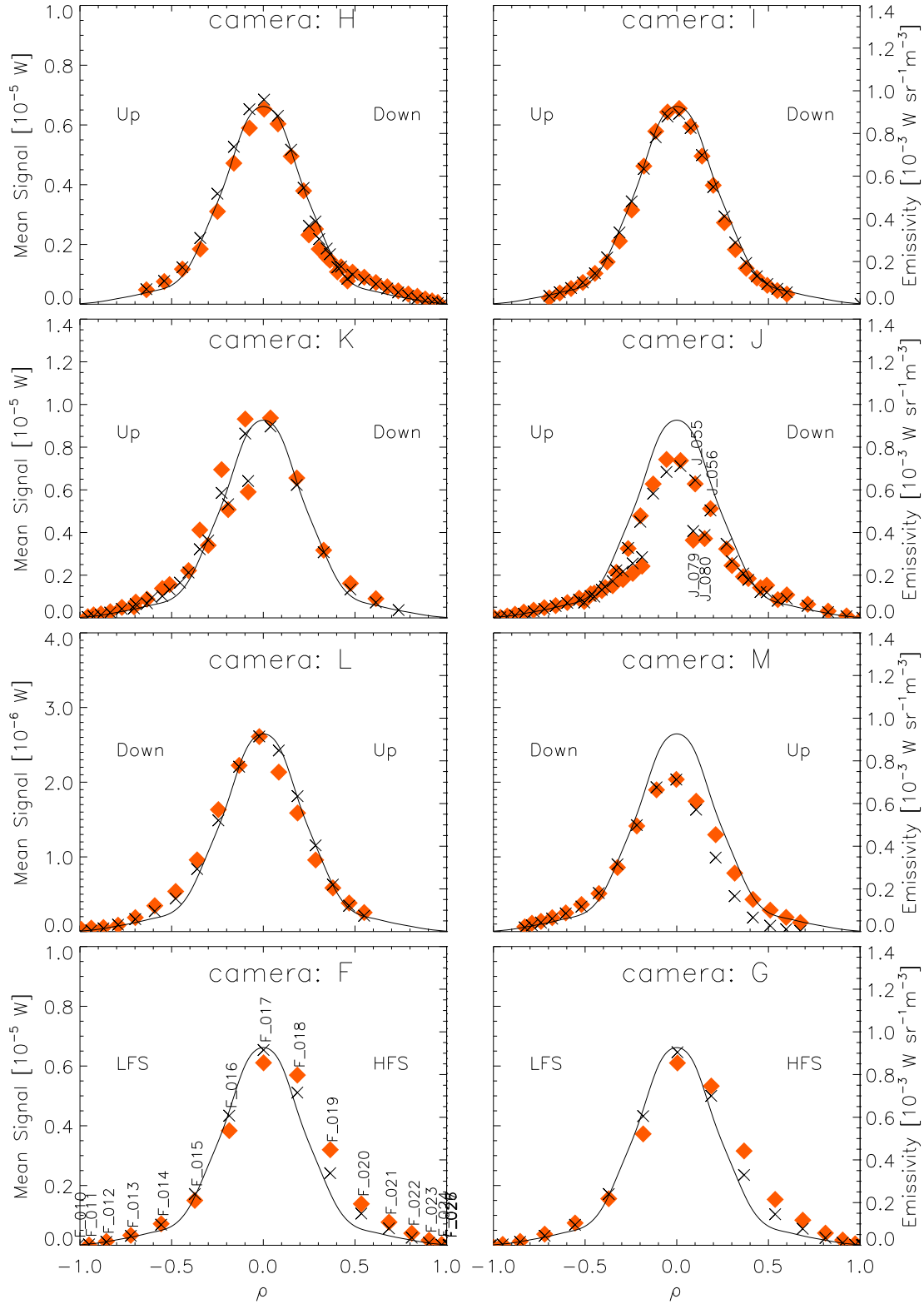


Figure 4.1 – This example shows the simulated (\times) and the measured (\blacklozenge) camera signals for all available channels. The simulated signals result from one single emissivity profile $e_0(\rho)$ which is plotted as a continuous line (—). For clarity only the signal names which are explicitly mentioned in the text are plotted.

In the following the results in figure 4.1 are discussed. The VOS (volume of sight) of the L, M, F and G camera is limited by tiles as explained in section 3.3. This is the reason why the maximal signal of the L and M camera is smaller by a factor of approximately 0.4 than the maximal signal of the H camera. The maximal signal of the F and G cameras have the same magnitude as the maximal signal of the H camera. This is because the tile-effect is compensated by the longer VOS of the F and G cameras which point to the top.

Although the VOS with the signal-names $\blacklozenge J_{_055}$ and $\blacklozenge J_{_079}$ (and also $\blacklozenge J_{_056}$ and $\blacklozenge J_{_080}$) are roughly identical, the signals of $\blacklozenge J_{_079}$ and $\blacklozenge J_{_080}$ are much lower. The reason for this is discussed in the following. Let us consider that all the channels of one camera see the same homogeneous emissivity. Then the channels with border chip position have a smaller signal because the point-response-function (introduced in section 3.1) is lower (in the same x-y plane in camera coordinates) and the VOS is smaller. Because the signals $\blacklozenge J_{_079}$ and $\blacklozenge J_{_080}$ result from a chip with border-position the signals are much lower. This effect also arises at camera K and H.

Since the described geometry-effects are due to detector properties and not due to plasma properties they are often eliminated with a geometrical calibration ([22] equation 3.15). This geometrical calibration causes the signals to have the unit Wm^{-2} instead of the unit W .

Because the camera-simulation (which is described in section 3) takes the full three-dimensional geometry into account (and the simulated camera signals have the unit W) the simulated signal should be compared with the geometrically-uncalibrated measured signals (which also have the unit W).

In this section the reconstruction of an emissivity profile is explained using an example. Note that the degree of non-uniqueness of the emissivity profile is high. This is especially the case for hollow profiles which are discussed in section 5.2.

The approach of constant emissivity in time is a first approximation. Due to the time dependent perturbation of the equilibrium flux surface the emissivity changes over time. This effect is considered in the next section.

4.2 The emissivity of mode-perturbed plasma

In the last section we considered the time-averaged emissivity which is constant in time. We now improve this first approximation by considering the emissivity of mode-perturbed plasma. The flux surfaces are displaced due to the displacement function $\vec{\xi}$ and emissivity does not change on the displaced flux surfaces. First the representation of the displacement in two different coordinate systems is explained. The first is a polar coordinate system with the coordinates (ρ, θ) which have been introduced in section 1.2.2. The magnetic axis is the center of the polar coordinate system. The second coordinate system is cartesian and it is defined by

$$\begin{pmatrix} v \\ w \end{pmatrix} = \begin{pmatrix} \rho \cos(\theta) \\ \rho \sin(\theta) \end{pmatrix}. \quad (4.1)$$

This coordinate system is not a real space coordinate system and should not be identified with the spatial coordinates (R, z) . The unit vectors of the polar coordinate system e_ρ, e_θ and the unit vectors of this cartesian coordinate system e_v, e_w have the following representation:

$$\hat{e}_\rho = \begin{pmatrix} \cos(\theta) \\ \sin(\theta) \end{pmatrix}, \hat{e}_\theta = \begin{pmatrix} -\sin(\theta) \\ \cos(\theta) \end{pmatrix}, \hat{e}_v = \begin{pmatrix} 1 \\ 0 \end{pmatrix}, \hat{e}_w = \begin{pmatrix} 0 \\ 1 \end{pmatrix}. \quad (4.2)$$

The degree of freedom of the displacement function $\vec{\xi}$ is reduced by $\xi_\phi = 0$ for the toroidal component of the displacement function ξ_ϕ (note that $\vec{\xi}$ still depends on ϕ). This restriction is justified by the fact that, the srx diagnostics can only resolve the poloidal displacement of flux surfaces. This is because it is expected, that the possible toroidal displacement has the same magnitude then the poloidal displacement ($\approx 0.05\rho \approx 2.5\text{cm}$) and the toroidal width of the VOS ($\approx 5\text{cm}$) is larger. Furthermore, there is almost no emissivity gradient in the toroidal direction and a displacement in this direction has almost no impact on the poloidal spatial emissivity distribution.

The representation of the displacement function $\vec{\xi}$ depends on the coordinate system:

$$\vec{\xi} = \xi_\rho \hat{e}_\rho + \xi_\theta \hat{e}_\theta = \xi_v \hat{e}_v + \xi_w \hat{e}_w. \quad (4.3)$$

To assure the divergence freeness of $\vec{\xi}$ as discussed in section 1.2.3 we use the fact, that $\nabla \cdot (\nabla \times \vec{f}) = 0$ holds for every twice-differentiable vector field \vec{f} [28]. In this thesis we consider a two-dimensional displacement in the poloidal plane and therefore $\vec{f} \sim e_\phi$ and $\nabla \times \vec{f} = e_\phi \times \nabla f_\phi$ holds.

Finally the displacement $\vec{\xi}$ is represented by

$$\vec{\xi} = e_\phi \times \nabla f_\phi. \quad (4.4)$$

Like in [27], let the radial component of the displacement be

$$\xi_\rho = \xi_0(\rho) \cos(m\theta + n\phi + \varphi_0 + \omega t). \quad (4.5)$$

In order to reproduce equation 4.5 the function f_ϕ is chosen to be

$$f_\phi = \frac{1}{m} \rho \xi_0(\rho) \sin(m\theta + n\phi + \varphi_0 + \omega t). \quad (4.6)$$

Using the nabla operator ∇ in polar coordinates from 4.4 and 4.6 follows:

$$\vec{\xi} = \begin{pmatrix} \xi_\rho \\ \xi_\theta \\ \xi_\phi \end{pmatrix} = \begin{pmatrix} \frac{1}{\rho} \partial_\theta f_\phi \\ -\partial_\rho f_\phi \\ 0 \end{pmatrix} = \begin{pmatrix} \xi_0(\rho) \cos(m\theta + n\phi + \varphi_0 + \omega t) \\ -\frac{1}{m} \sin(m\theta + n\phi + \varphi_0 + \omega t) (\xi_0(\rho) + \rho \xi_0'(\rho)) \\ 0 \end{pmatrix}. \quad (4.7)$$

So the displacement function $\vec{\xi}$ is totally defined by the poloidal mode number m , the toroidal mode number n , the angular velocity ω of the mode, the phase ϕ_0 and the radial displacement ξ_0 . A change of sign of ω causes the mode to rotate in the opposite direction.

Switching to cartesian coordinates using 4.2 and dropping the third component of 4.7 leads to:

$$\vec{\xi} = \begin{pmatrix} \xi_v \\ \xi_w \end{pmatrix} = \xi_\rho \begin{pmatrix} \cos(\theta) \\ \sin(\theta) \end{pmatrix} + \xi_\theta \begin{pmatrix} -\sin(\theta) \\ \cos(\theta) \end{pmatrix} = M \begin{pmatrix} \xi_\rho \\ \xi_\theta \end{pmatrix} \text{ with } M = \begin{pmatrix} \cos(\theta) & -\sin(\theta) \\ \sin(\theta) & \cos(\theta) \end{pmatrix}.$$

In the following a model for the emissivity of displaced flux surfaces is derived. Let us consider a fixed position (ρ, θ) in the representation of a cartesian coordinate system in flux coordinates:

$$\begin{pmatrix} v \\ w \end{pmatrix} = \begin{pmatrix} \rho \cos(\theta) \\ \rho \sin(\theta) \end{pmatrix}. \quad (4.8)$$

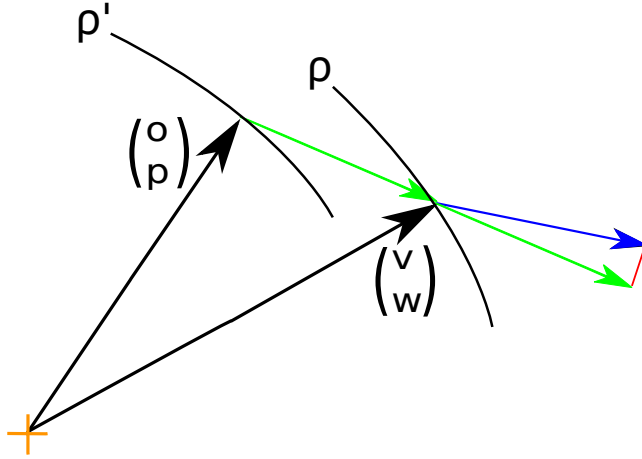


Figure 4.2 – Visualization of two displaced flux surfaces. The magnetic axis is plotted with +.

The fixed position (v, w) is visualized in figure 4.2. The ρ -value of the corresponding flux surface is given by $\rho = \left\| \begin{pmatrix} v \\ w \end{pmatrix} \right\|$, where $\|\vec{u}\| = \sqrt{\langle \vec{u}, \vec{u} \rangle}$ is the Euclidean norm of \vec{u} . Then the flux surfaces are perturbed from the equilibrium due to a displacement which is given by the displacement

function $\vec{\xi}$. The vector of the displacement vector field at the position (v, w) denoted by $\vec{\xi}(v, w)$ is plotted in blue in figure 4.2. With the framework of ideal MHD the topology of the flux surfaces does not change and flux surfaces do not reconnect. For the considered situation this means, that there is a unique position (o, p) from where the undisplaced

flux surface (which is denoted by ρ') is displaced with the displacement $\vec{\xi}(o, p)$ to the position (v, w) :

$$\begin{pmatrix} v \\ w \end{pmatrix} = \begin{pmatrix} o \\ p \end{pmatrix} + \vec{\xi}(o, p). \quad (4.9)$$

The displacement $\vec{\xi}(o, p)$ is plotted with a green vector in figure 4.2. Due to the displacement the ρ -value at the fixed position (v, w) changes from ρ to ρ' . The value of ρ' is given by

$$\rho' = \left\| \begin{pmatrix} v \\ w \end{pmatrix} - \vec{\xi}(o, p) \right\|. \quad (4.10)$$

In order to calculate the position (o, p) the equation 4.9 has to be inverted respectively to (o, p) . The analytical inversion exists because the flux surfaces do not reconnect and there is a unique flux surfaces displaced to (v, w) . But the analytical inversion is complicated because of the form of $\vec{\xi}$ in equation 4.7. A numerical inversion is possible, but due to the number of grid points (~ 20000 per channel) this procedure is very calculation-time intensive. Therefore there is an approximation considered in the following. Using equation 4.9 the displacement $\vec{\xi}$ is given by:

$$\vec{\xi} \begin{pmatrix} o \\ p \end{pmatrix} = \vec{\xi} \left(\begin{pmatrix} v \\ w \end{pmatrix} - \vec{\xi} \begin{pmatrix} o \\ p \end{pmatrix} \right). \quad (4.11)$$

where the notation $\vec{\xi}(o, p) = \vec{\xi} \begin{pmatrix} o \\ p \end{pmatrix}$ is used. The Taylor expansion of equation 4.11 reads

$$\vec{\xi} \begin{pmatrix} o \\ p \end{pmatrix} = \vec{\xi} \begin{pmatrix} v \\ w \end{pmatrix} - J_{\xi}|_{(v,w)} \vec{\xi} \begin{pmatrix} o \\ p \end{pmatrix} + O \left(\left\| \vec{\xi} \begin{pmatrix} o \\ p \end{pmatrix} \right\|^2 \right) \quad (4.12)$$


where $J_{\xi}|_{(v,w)}$ is the Jacobian matrix of $\vec{\xi}$ at (v, w) . The neglect of the second order and of all higher order terms is a good approximation if

$$\left\| \vec{\xi} \begin{pmatrix} o \\ p \end{pmatrix} \right\| \ll 1 \quad (4.13)$$

also the first order in equation 4.12 is neglected. This is a good approximation if

$$|\xi_i(v, w)| \ll \left| \left(J_{\xi}|_{(v,w)} \xi(o, p) \right)_i \right| \quad (4.14)$$

holds for every component $i = 1, 2$.

This condition means that the vector field shall not vary much with respect to the length of the vector field itself. This condition is visualized in figure 4.2 and it holds if the red line  is short compared to the length of the vectors of the vector field around (v, w) .

holds. So if the change of the vector field from (v, w) to (o, p) is small it is a good approximation to set

$$\vec{\xi} \begin{pmatrix} o \\ p \end{pmatrix} \approx \vec{\xi} \begin{pmatrix} v \\ w \end{pmatrix}. \quad (4.15)$$

As discussed in section 1.2.3 the displacement of a $m = 1$ kink mode is constant inside the $q = 1$ surface and for this region equation 4.15 holds without being approximative. Outside this region the radial displacement function changes and in this region 4.15 is an approximation. For the example shown in figure 4.2 the possible difference between $\vec{\xi}(v, w)$ and $\vec{\xi}(o, p)$ is visualized with a red line (—).

The flux coordinate $\rho'(v, w, \vec{\xi}(v, w))$ describes the displaced flux surfaces and ρ' is constant on a displaced flux surface. Therefore ρ' represents the structure of the displaced flux surfaces (and the structure of the mode). In the following ρ' will be derived in the units of the undisplaced equilibrium.

With the appearance of a displacement $\vec{\xi}$ the radial flux coordinate ρ at (v, w) changes. The new flux coordinate is denoted by ρ' and it is described in units of the unperturbed equilibrium:

$$\rho' = \left\| \begin{pmatrix} v \\ w \end{pmatrix} - \begin{pmatrix} \xi_v \\ \xi_w \end{pmatrix} \right\| = \left\| \begin{pmatrix} \rho \cos(\theta) \\ \rho \sin(\theta) \end{pmatrix} - M \begin{pmatrix} \xi_\rho \\ \xi_\theta \end{pmatrix} \right\| = \quad (4.16)$$

$$= \sqrt{\left(\begin{pmatrix} \rho \cos(\theta) \\ \rho \sin(\theta) \end{pmatrix} \right)^2 - 2 \left\langle M \begin{pmatrix} \xi_\rho \\ \xi_\theta \end{pmatrix}, \begin{pmatrix} \rho \cos(\theta) \\ \rho \sin(\theta) \end{pmatrix} \right\rangle + \left(M \begin{pmatrix} \xi_\rho \\ \xi_\theta \end{pmatrix} \right)^2} \quad (4.17)$$

Because M is a rotation matrix $\langle M\vec{a}, M\vec{b} \rangle = \langle \vec{a}, \vec{b} \rangle$ and $\langle M\vec{a}, \vec{b} \rangle = \langle \vec{a}, M^{-1}\vec{b} \rangle$ hold for every \vec{a} and \vec{b} . We also use 4.8 and the equation for ρ' reduces to

$$\rho' = \sqrt{\rho^2 - 2 \left\langle M \begin{pmatrix} \xi_\rho \\ \xi_\theta \end{pmatrix}, \begin{pmatrix} \rho \cos(\theta) \\ \rho \sin(\theta) \end{pmatrix} \right\rangle + \left(\begin{pmatrix} \xi_\rho \\ \xi_\theta \end{pmatrix} \right)^2} \quad (4.18)$$

$$= \sqrt{\rho^2 - 2\rho \left\langle \begin{pmatrix} \xi_\rho \\ \xi_\theta \end{pmatrix}, M^{-1} \begin{pmatrix} \cos(\theta) \\ \sin(\theta) \end{pmatrix} \right\rangle + \left(\begin{pmatrix} \xi_\rho \\ \xi_\theta \end{pmatrix} \right)^2} \quad (4.19)$$

$$= \sqrt{\rho^2 - 2\rho\xi_\rho + \xi_\rho^2 + \xi_\theta^2} \quad (4.20)$$

where ξ_ρ and ξ_θ are given by equation 4.7.

Let the equilibrium emissivity be described by an emissivity profile $e_0(\rho)$ like discussed in section 4.1. Considering the displacement due to $\vec{\xi}$, the emissivity at (v, w) is given by the emissivity at the original point ρ' :

$$e'(\rho, \theta) = e_0(\rho') \quad (4.21)$$

$$e'(\rho, \theta) = e_0 \left(\sqrt{\rho^2 - 2\rho\xi_\rho + \xi_\rho^2 + \xi_\theta^2} \right). \quad (4.22)$$

This model of emissivity is called poloidal-perturbation emissivity model. Note that the derivation is carried out using θ but the derivation remains valid by replacing θ by θ^* . In order to consider the poloidal structure of the field lines, in the implementation θ^* is used in equation 4.22.

We now consider an example using the derived poloidal-perturbation emissivity model in order to check whether the simulation and the model reproduces the expected results.

We consider the two examples $m=1$ and $m=2$ and for reasons of simplicity we set $\omega = 1, n = 1$ and $\varphi_0 = 0$. Let the plasma emissivity be $e(\rho) = -\rho^2 + 1$ and let the displacement be given by the step-function:

$$\text{with } \xi_0(\rho) = \begin{cases} 0.1 & \text{for } \rho \leq 0.5 \\ 0 & \text{for } \rho > 0.5. \end{cases} \quad (4.23)$$

It is discussed in section 1.2.3 that choosing ξ_0 to be a step-function can be physically motivated for the $m = 1$ case. But according to equation (25) in [23] $\xi_0(\rho) \sim \rho^{m-1}$ holds and the step-function does not minimize the energy functional 1.19 for the $m = 2$ case. Figure 4.3 shows the results of the simulation.

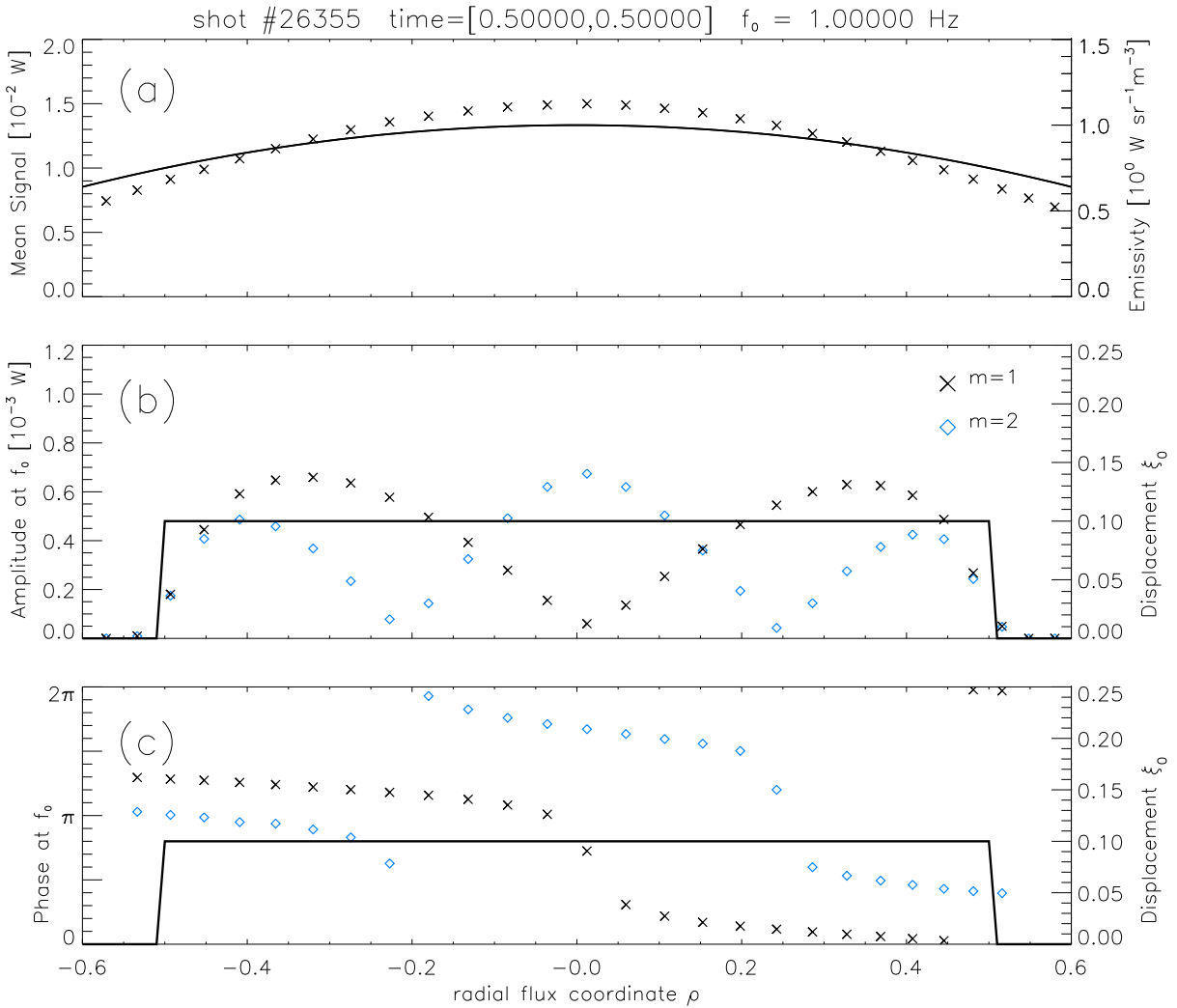


Figure 4.3 – (a) shows the mean emissivity profile (—) and the simulated signals (\times). In (b) and (c) the amplitudes and phases of the signals for the $m = 1$ (\times) and the $m = 2$ (\diamond) case and the radial displacement ξ_0 (—) are plotted. All values are calculated as discussed in section 3.2.

It is discussed in [22] that modes with the poloidal mode number m (inside a peaked e_0 profile) cause m minima in the amplitude profile and each minimum in the amplitude profile is connected with a phase jump of π . Figure 4.3 shows, that the expected results are reproduced by the emissivity model and the camera simulation.

4.3 A comparison of emissivity models

Since the equilibrium profile e_0 just depends on ρ one may be tempted to neglect the tangential displacement ξ_θ . The so called radial perturbation emissivity model is given by

$$e = e_0(\rho + \xi_\rho). \quad (4.24)$$

Now we push the approximation even further by a first order Taylor expansion of equation 4.24 to the first order around $\rho = 0$. This leads to the so called approximate model for the emissivity of mode-perturbed plasma:

$$e = e_0(\rho) + \frac{\partial e}{\partial \rho} \xi_\rho. \quad (4.25)$$

This model was presented in [21]. Now the three models of emissivity of mode perturbed plasma which are given in equation 4.22, 4.24 and 4.25 are compared using an example. Let ξ_0 be a step-function and let the poloidal mode number be $m=1$. Without loss of generality we set $\varphi_0 = 0$ and consider a time point $t = 0$. The derivative freeness $\xi'_0 = 0$ and $m = 1$ implies, according to equation 4.7, that $\xi_\rho^2 + \xi_\theta^2 = \xi_0^2$ holds. Using the known values equation 4.20 transforms to

$$\rho' = \sqrt{\rho^2 + 2\rho\xi_0 \cos(\theta + n\phi) + \xi_0^2} \quad (4.26)$$

Let us now consider all the points (ρ, θ, ϕ) with $\rho \leq 1$ for which $\cos(\theta + n\phi) = \pm 1$ hold. These points represent a two-dimensional manifold (which is a surface) in space (for the next example the intersection of it and the poloidal plane at $\phi = 0$ is the x-axis in figure 4.5). On the $\cos(\theta + n\phi) = \pm 1$ manifold $\xi_\rho = \pm \xi_0$ holds and the equation 4.26 transforms to

$$\rho' = \sqrt{\rho^2 \pm 2\rho\xi_0 + \xi_0^2} = \rho \pm \xi_0. \quad (4.27)$$

This means that the radial perturbation and the poloidal perturbation emissivity model are not distinguishable on a $\cos(\theta + n\phi) = \pm 1$ manifold. On the $\cos(\theta + n\phi) = \pm 1$ manifold the approximate model gives different values than the other two models.

On the $\cos(\theta + n\phi) = 0$ manifold (this is, for the next example, the y-axis in figure 4.5) the radial displacement vanishes and the emissivity given by the radial perturbation model (equation 4.24) and the approximate model (equation 4.25) reduces to the equilibrium emissivity $e_0(\rho)$. So on a $\cos(\theta + n\phi) = 0$ manifold the radial perturbation model and the approximate model are indistinguishable from the equilibrium emissivity $e_0(\rho)$. But a significant difference between the poloidal perturbation model and the equilibrium emissivity $e_0(\rho)$ occurs.

The general results are illustrated with an example: let the equilibrium emissivity profile be

$$e_0(\rho) = 2.0 \diamond(-(\rho/0.1)^2) + \diamond(-(\rho/0.3)^2) \quad (4.28)$$

and let the displacement be defined by the step-function in equation 4.23. The resulting displacement vector field is visualized in figure 4.4. Figure 4.5 shows the contour plots of the emissivity on a poloidal plane at $\phi = 0$ in the cartesian coordinate system resulting from the poloidal perturbation model (fig. 4.5(a')), radial perturbation (fig. 4.5(b')) model and the approximate model (fig 4.5(c')).

For the given example the $\cos(\theta + n\phi) = \pm 1$ manifold corresponds to the x-axis and the $\cos(\theta + n\phi) = 0$ manifold corresponds to the y-axis in figure 4.5. Furthermore, this means that the values on the x-axes in figure 4.5(a') and 4.5(b') are equal and the values on the y-axes in figures 4.5(b'), 4.5(c') and 4.5(c) are equal.

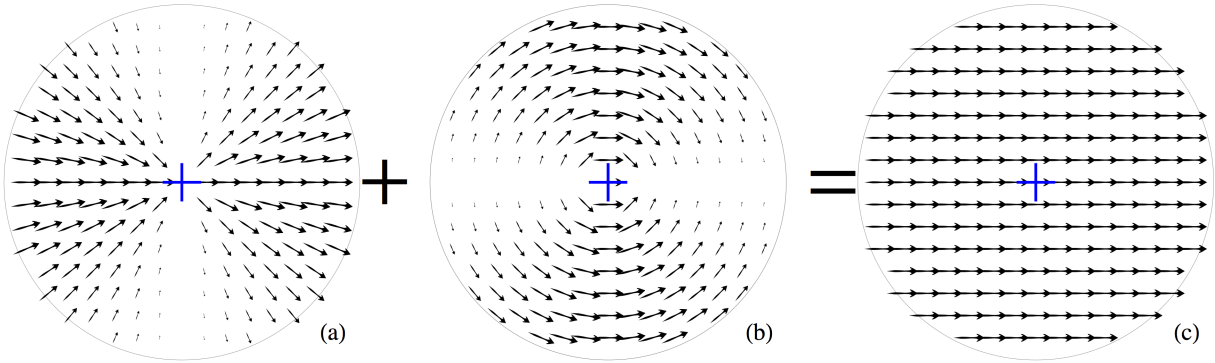


Figure 4.4 – Vector plots of the displacement resulting from equation 4.23. The displacement consists of the radial displacement $\hat{e}_\rho \xi_\rho$ (a) and the angular displacement $\hat{e}_\theta \xi_\theta$ (b). The addition of both $\hat{e}_\rho \xi_\rho + \hat{e}_\theta \xi_\theta$ is called the poloidal displacement (c). A circle with a radius of 0.5 is plotted and the + sign marks the origin. The vectors are not drawn to scale.

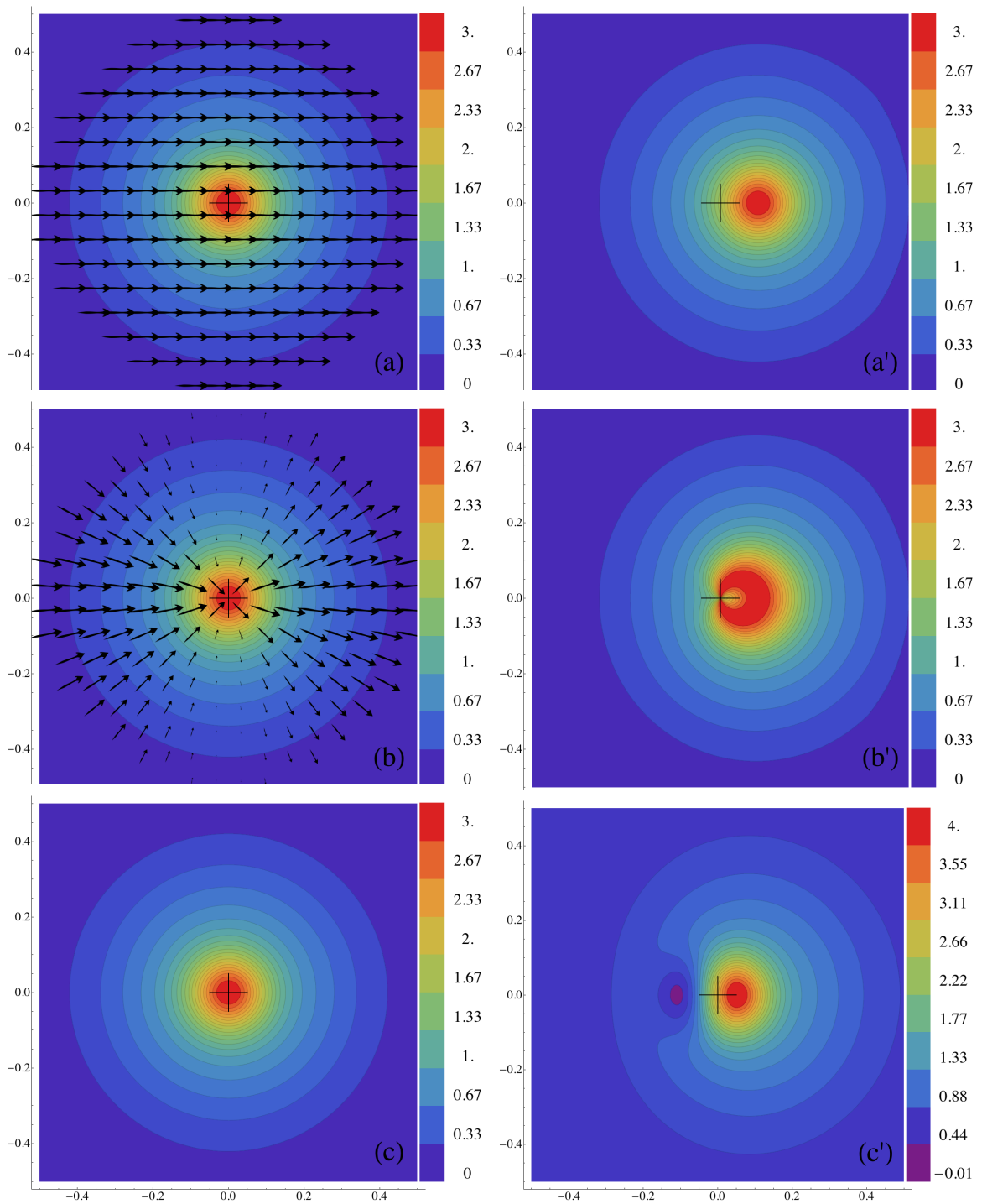


Figure 4.5 – Figure (c) shows a contour plot of the equilibrium emissivity which is defined in equation 4.28. In figures (a) and (b) the equilibrium emissivity is over plotted with the vector field of the poloidal displacement (a) and the radial displacement (b) function. Note that the vectors are not drawn to scale. Figures (a'), (b') and (c') show a contour plot of the emissivity resulting from the poloidal perturbation model (a'), the radial perturbation model (b') and the approximate model (c'). The + sign marks the magnetic axis.

We now apply the developed virtual srx diagnostic on the introduced example (which is reminiscent of a snake structure [37]), given by equations 4.28 and 4.23. The displacement is considered to be time dependent like in equation 4.5 and we set $\omega = 1$. The results for the three different models for mode perturbed emissivity are compared and discussed; figure 4.6 shows the results of the simulations.

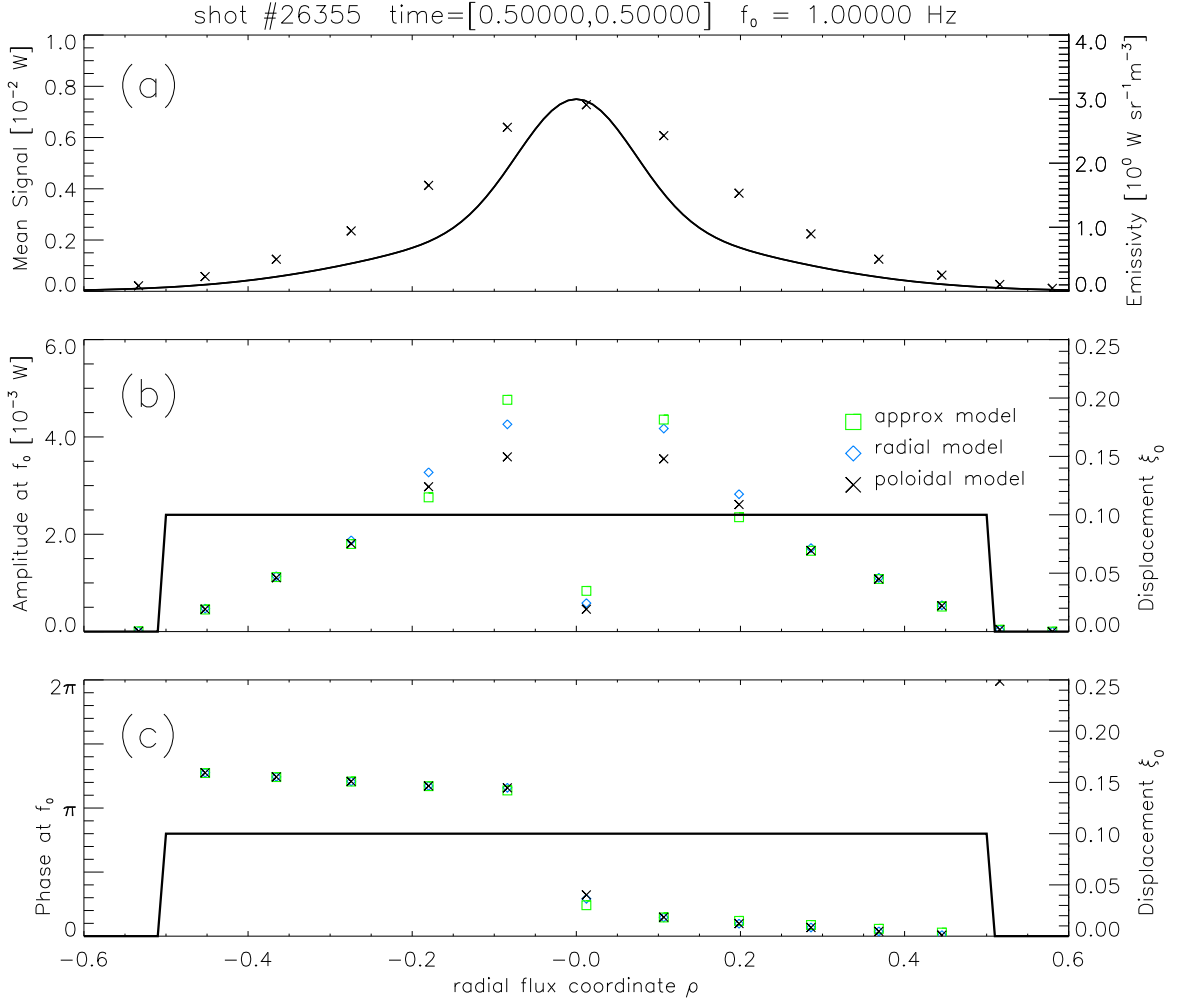


Figure 4.6 – Comparison of the simulated signals resulting from the poloidal perturbation model (\times), the radial perturbation model (\diamond) and the approximate model (\square) using the same equilibrium emissivity (— in (a)) and the same displacement ξ_0 (— in (b) and (c)).

The comparison using the virtual sxr diagnostic leads to the result that the shape of the amplitudes does not depend on the model. In the domain of a very high emissivity gradient $\rho \in [-0.3, 0.3]$ the amplitudes resulting from the radial perturbation model and the approximate model are almost always increased. In the domain of a lower emissivity gradient $\rho \in \pm(0.3, 1.0]$ the magnitude of the amplitudes does not depend on the model. Over the whole domain $\rho \in [-1, 1]$ there are no significant differences observable in the simulated phases.

So far the amplitudes and phases of the simulated signals have been compared. Now we turn to a comparison of time traces of the signals. In figure 4.7 the signals of the I_053 camera (the central channel at about $\rho = 0.0$ in fig. 4.6) resulting from the three models are plotted over the time.

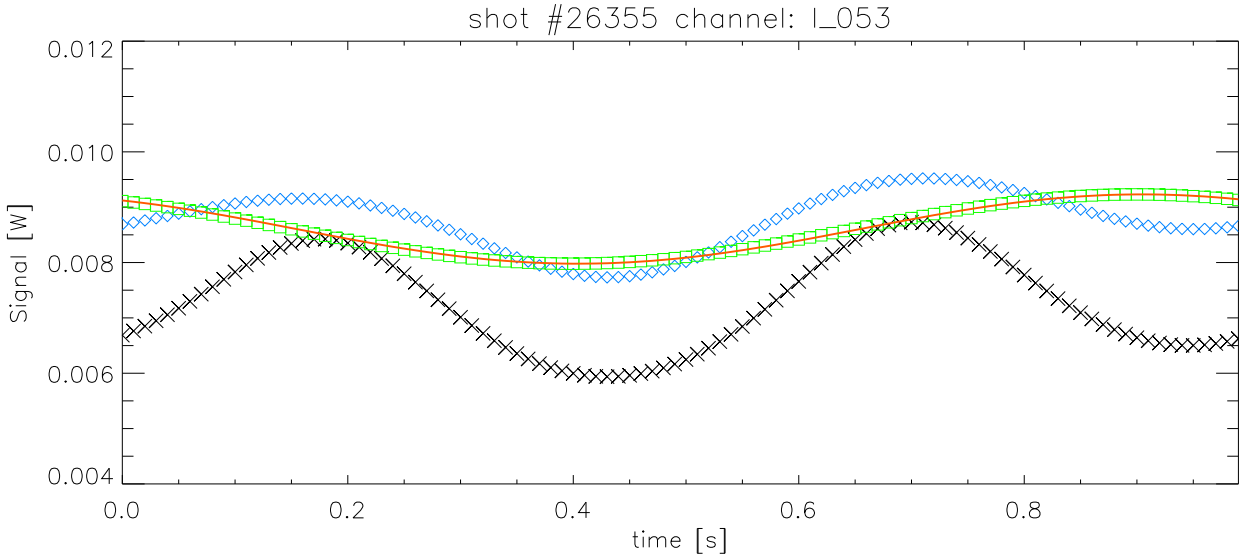


Figure 4.7 – Comparison of time traces of the simulated signals of the I_054 camera resulting from the poloidal perturbation model (\times), the radial perturbation model (\diamond) and the approximate model (\square). A sine function ($—$) is fitted to the simulated signals resulting from the approximate model (\square).

The temporal evolution of signals resulting from different models are quite different. In the time traces of the poloidal perturbation model (\times) and of the radial perturbation model (\diamond) frequency-doubling occurs; which means, that the maximal signal occurs twice during one mode period.

It is no accident that the sine function ($—$) matches the simulated signals, resulting from the approximate model (\square), so well. The signals resulting from the approximate model are harmonic in time. This is proven in appendix A.

In conclusion, the consideration of the displacement only in ρ -direction ξ_ρ (radial perturbation model) is an approximation although the equilibrium emissivity only depends on ρ . The consideration of the tangential displacement ξ_θ and the associated detour of introducing the cartesian coordinate system in equation 4.8 is necessary to derive the poloidal displacement model.

The usefulness of the radial perturbation model is limited for several reasons:

- The displacement in θ -direction ξ_θ is neglected. This causes in general the divergence of $\vec{\xi}$ not to vanish.
- As illustrated in figure 4.5, the approach changes the structure of the flux surface (and so the emissivity) in an unphysical manner.

Now we turn to the approximate model. It is not possible to get the emissivity structure which results from the approximate model (figure 4.5(c')) by displacing the equilibrium flux surfaces (figure 4.5(c)) because the codomains of emissivity are different. The codomain of emissivity resulting from equation 4.28 is $e \in [0.0, 3.0]$ (figure 4.5(c)) and the codomain of emissivity resulting from the approximate model, for the introduced example, is $e \in [-0.05\dots, 4.19\dots]$ (figure 4.5(c')). It is not possible to generate emissivity in the range of $e \in [3.0, 4.19\dots]$ or $e \in [-0.05\dots, 0.0]$ by displacing the equilibrium flux surfaces (figure 4.5(c)). There is no possibility of negative emissivity for the radial and poloidal displacement model because these models only effect the argument of the equilibrium emissivity e_0 and e_0 is always positive by definition.

We interpret the emissivity in figure 4.5(c) as constant on displaced flux surfaces. Then the lines of equ-emissivity are also lines of equ-flux. According to this interpretation the approximate model produces, for the introduced example, an additional *island* (in the sense that the topology of the flux surfaces is changed) with the center at $(x, y) = (-0.109\dots, 0.0)$ (figure 4.5(c)). The additional *island* is a mathematical artifact which arises from approximation and it has no physical counterpart.

Besides the above listed limitations for the radial perturbation model which apply even more strongly for the approximate model there are the following additional limitations:

- The time dependent simulated camera-signals resulting from equation 4.25 have a harmonic form in time. This is proven in appendix A.
- With this approach there is the possibility of negative emissivity which is unphysical. In the example in figure 4.5(c') negative emissivity actually occurs.
- It is illustrated in figure 4.7 that the phenomenon of frequency-doubling for snake-like emissivity distributions in the central VOS cannot be described.

The quality of the two approximations degrades the larger the displacement is and the larger the gradient of the equilibrium emissivity is.

From now on the poloidal perturbation model is used. Note that the approach can be used to investigate the mode structure with other diagnostics. Assume the equilibrium temperature and current profiles $T_e(\rho)$ and $j(\rho)$ are known. Then the mode perturbed values are given by $T_e(\rho')$ and $j(\rho')$ with ρ' as defined in equation 4.20.

4.4 Properties of modes defined in flux coordinates

In this section the structure of the emissivity in flux coordinates is compared with the structure of the emissivity in real space coordinates. Also the impact of the consideration of θ^* instead of θ is discussed. The effects are exemplified using the following emissivity:

$$e_{con}(\rho, \theta, t) = \left(\frac{1}{2}(\sin(\pi\rho) + 1.0) \right)^{14} \left(\frac{1}{2}(\cos(\theta + 2\pi t) + 1) \right)^6. \quad (4.29)$$

Only for this example the ϕ -dependence is neglected; in general the dependency is considered. Figure 4.8 (a) shows a contour plot of the emissivity defined in equation 4.29 in the cartesian coordinate system $(x, y) = (\rho \cos(\theta), \rho \sin(\theta))$ using the radial flux coordinate ρ .

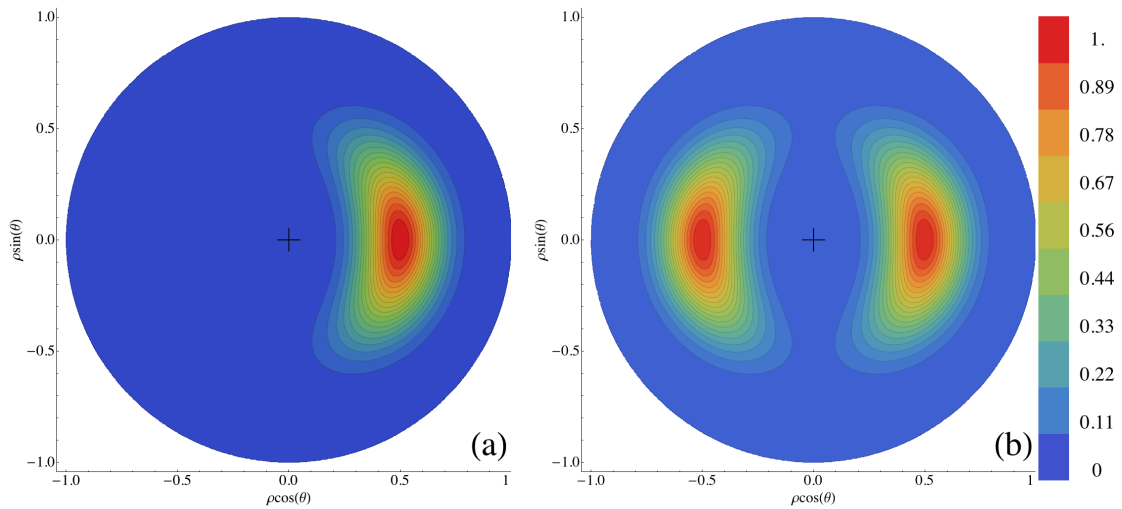


Figure 4.8 – In (a) the emissivity $e_{con}(\rho, \theta, t = 0)$ and in (b) the emissivity $e_{con}(\rho, \theta, t = 0) + e_{con}(\rho, \theta, t = 0.5)$ is visualized in flux coordinates. The axes are given by $x = \rho \cos(\theta)$ and $y = \rho \sin(\theta)$.

In order to compare the emissivity on the LFS and on the HFS $e_{con}(\rho, \theta, t = 0) + e_{con}(\rho, \theta, t = 0.5)$ is visualized in figure 4.8 (b); the structure is symmetric with respect to reflection on the y-axis. Figure 4.9 (b) shows that this symmetry does not hold in real space coordinates anymore because on one flux surface (with fixed ρ) the radial real space coordinate r depends on θ .

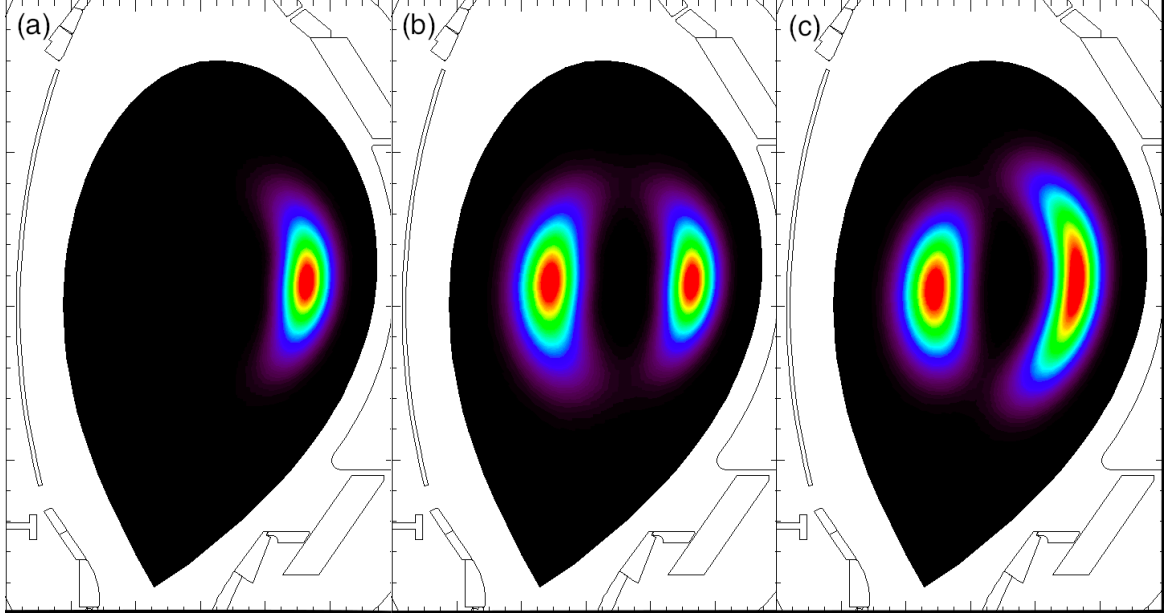


Figure 4.9 – In (a) the emissivity $e_{con}(\rho, \theta, t = 0)$, in (b) the emissivity $e_{con}(\rho, \theta, t = 0) + e_{con}(\rho, \theta, t = 0.5)$ and in (c) the emissivity $e_{con}(\rho, \theta^*, t = 0) + e_{con}(\rho, \theta^*, t = 0.5)$ is visualized in real space coordinates.

On the horizontal plane ($z = 0$) a change of $d\rho$ on the HFS causes a change of dr_{HF} in real space coordinates and $d\rho$ on the LFS causes a change of dr_{LF} in real space coordinates. Because of $dr \sim \frac{1}{R}B\theta$ it follows that $dr_{HF} > dr_{LF}$ holds [33]. And as visualized in figure 4.9 (b) the structure of emissivity has a bigger width in ρ -direction on the HFS compared to the width on the LFS.

So far the emissivity has been parametrized using the angular coordinate θ . But the emissivity is considered to be constant on field lines and the geometry of field lines in a poloidal plane is described with θ^* . Therefore the emissivity is parametrized using the straight field line angle θ^* and θ in equation 4.29 is replaced by θ^* . In figure 4.9 (c) the resulting emissivity $e_{con}(\rho, \theta^*, t = 0) + e_{con}(\rho, \theta^*, t = 0.5)$ is visualized.

Comparing 4.9 (b) and (c), the size of the emissivity structure in ρ -direction remains unchanged. And there is almost no difference between the two emissivity structures on the HFS $e_{con}(\rho, \theta, t = 0.5)$ and $e_{con}(\rho, \theta^*, t = 0.5)$. The emissivity structure $e_{con}(\rho, \theta^*, t = 0)$ on the LFS is heightened in θ -direction compared to the emissivity structure $e_{con}(\rho, \theta, t = 0)$. The impact of the exchange of θ by θ^* is now investigated using the camera simulation. In figure 4.10 the mean signals, amplitudes and phases resulting from the simulation using $e_{con}(\rho, \theta, t)$ are compared with the simulation using $e_{con}(\rho, \theta^*, t)$.

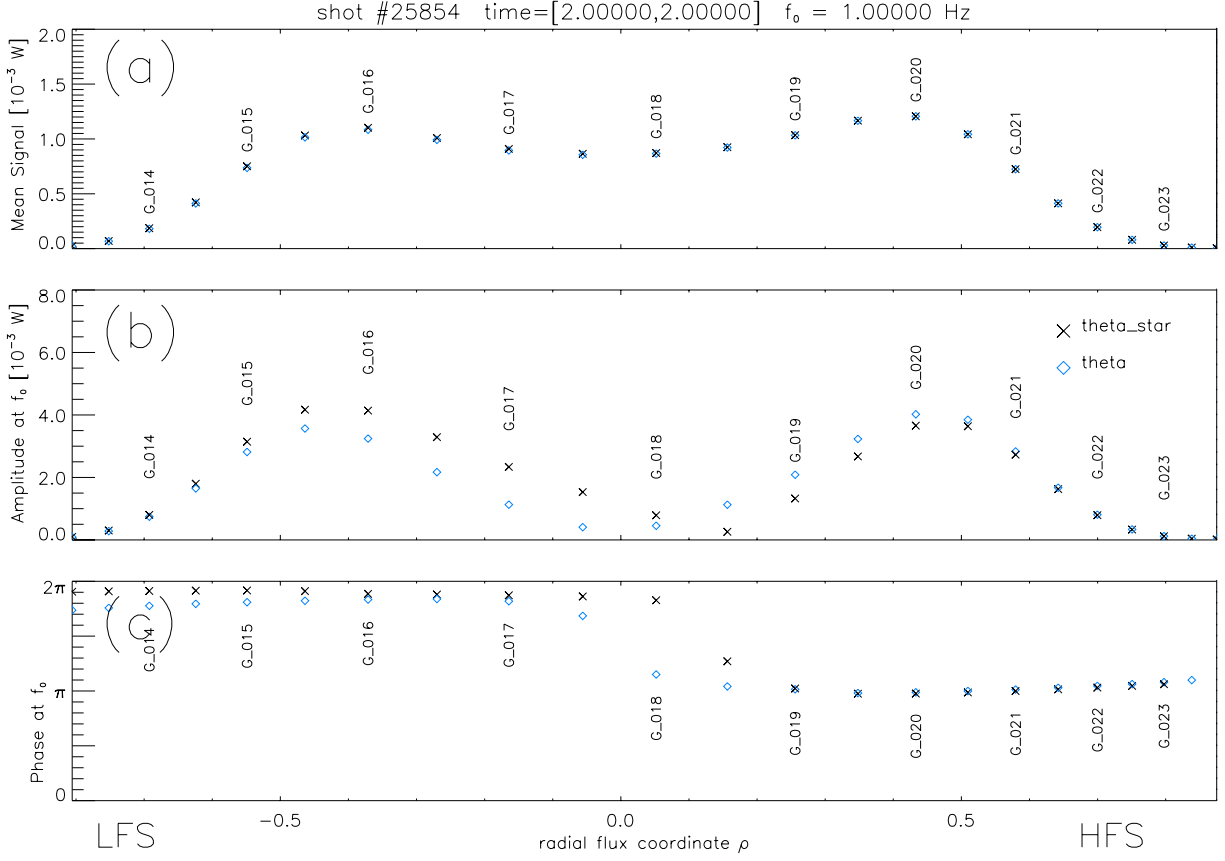


Figure 4.10 – The mean signals (a), amplitudes (b) and phases (c) resulting from the camera simulation using the emissivity $e_{con}(\rho, \theta, t)$ (\diamond) and the emissivity $e_{con}(\rho, \theta^*, t)$ (\times). For a better resolution, additional virtual channels are introduced in this example. These purely virtual channels are plotted without signal names.

Due to the exchange of θ by θ^* the amplitudes on the LFS increase and the amplitudes on the HFS decrease. Besides the changed position of the phase jump the phases change only marginally. The increase of the size in θ -direction on the LFS has almost no effect on the mean signals which is plotted in figure 4.10 (a). The reason for this effect is now investigated considering time traces of virtual camera channels.

In order to see a clear single signal maximum the outer channels (in terms of ρ) G_{015} and G_{021} are chosen. The phenomena of frequency doubling which was already encountered in figure 4.7 is investigated with a pure virtual channel G_{vir} . The channel is purely virtual in the sense, that is has no counterpart in reality. The channel G_{vir} is constructed in order to avoid any possible disturbing effects arising from geometry. The AVOS of the channel G_{vir} goes exactly through the plasma center and the angle of the axis of the VOS is $\theta = 90^\circ$. Figure 4.11 shows the simulated signals for the three channels resulting from $e_{con}(\rho, \theta, t)$ and from $e_{con}(\rho, \theta^*, t)$.

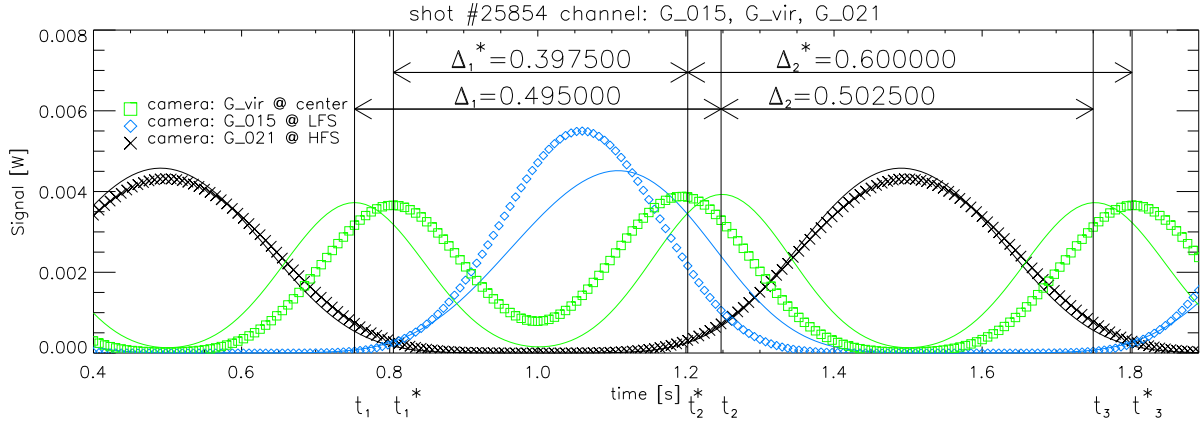


Figure 4.11 – Shows the time traces resulting from $e_{con}(\rho, \theta, t)$ with camera G_{015} (—), G_{021} (—), and G_{vir} (—) and resulting from $e_{con}(\rho, \theta^*, t)$ with camera G_{015} (◇), G_{021} (×), and G_{vir} (□).

As visualized in figures 4.10 (b) and (c) the structure of the emissivity on the HFS is almost not effected by the exchange of θ by θ^* . So in 4.11 there are only marginal differences between the signals with plot-mark — and the signals with plot-mark ×.

It is visualized in the same figures, that the exchange of θ by θ^* causes the emissivity structure to expand in θ -direction on the LFS. This causes the maximum of the signals with plot-mark ◇ to be higher than the maximum of the signals with plot-mark —. This effect has almost no effect on the mean of the signals because the higher maximum of the signals with plot-mark ◇ is compensated by the smaller FWHM. The FWHM is smaller because the structure of high emissivity propagates faster on the LFS then on the HFS. This effect is investigated closer.

In the time range $[0.5, 1.5]$ there are two maxima in the time trace of the G_{vir} camera (plot-mark □ and —) because the structure of high emissivity passes trough the VOS twice during one period $T = 1$. Because G_{vir} is constructed to be the central channel one maximum corresponds to the highest position (in z) P_1 and the other maximum corresponds to the lowest position (in z) P_2 of the structure of high emissivity.

For the emissivity $e_{con}(\rho, \theta, t)$ the structure of high emissivity reaches the position P_1 at the time point t_1 . The angular velocity is chosen to be positive so the mode moves clockwise and reaches the position P_2 at t_2 . Then the structure of high emissivity passes the HFS and reaches P_1 again at t_3 . The time it takes for the structure of high emissivity to move from P_1 to P_2 on the LFS Δ_1 is approximately the same time Δ_2 it takes to move from P_2 to P_1 on the HFS. Figure 4.7 shows that $\Delta_1 \approx \Delta_2$ holds.

Considering the emissivity defined in straight field line coordinates $e_{con}(\rho, \theta^*, t)$ the time it takes for the structure of high emissivity to pass the LFS Δ_1^* is shorter than the time Δ_2^* it takes to pass the HFS. Figure 4.7 shows that $\Delta_1^* < \Delta_2^*$ holds. So anharmonic (localized) emissivity structures propagate faster on the LFS than on the HFS because the steepness of the field lines B_p/B_t is higher on the LFS then on the HFS [22].

This discussion showed that there is a significant change in the signals if θ^* is considered instead of θ . Because θ^* describes the (poloidal) field line structure it is used in the implementation.

5 Investigation of idealized internal kink modes

In this section idealized examples of ideal internal $(m, n) = (1, 1)$ kink modes are investigated considering the (two-dimensional) poloidal displacement which is generated by the displacement function $\xi_0(\rho)$ referring to equation 4.7. This poloidal displacement $\vec{\xi}$ depends on the toroidal position ϕ pursuant to the defined toroidal mode number n . It is discussed how the time dependent simulated signals depend on the magnetic structure of the kink which is described by the displacement function $\vec{\xi}(\vec{x})$, on the background emissivity profile $e_0(\rho)$ (and especially its gradient) and on the position of the equilibrium flux surfaces. By keeping two of these three dependencies constant and varying the third the resulting isolated effects are studied under well defined conditions.

It is outlined in section 1.2.3 that the energy functional 1.19 is minimized by a displacement which is divergence free and referring to equation 4.7 the displacement $\vec{\xi}$ is constructed from $\xi_0(\rho)$ in such a way that the divergence freeness is inherently given. With \vec{v} being the flow velocity of a fluid, the fluid is incompressible if and only if $\vec{\nabla} \cdot \vec{v} = 0$ holds [29]. The flow velocity of the flux surface is $\vec{v} = d\vec{\xi}/dt$ and the divergence freeness of $\vec{\xi}$ corresponds to an incompressible flow of the flux surfaces; an example is given in section 5.1.

The ideal internal kink instability is introduced in section 1.2.3 and so far it is characterized by the following: there is a region $\rho \in [0, \rho_1]$ in which the displacement ξ_0 is constant and because the instability is internal and the plasma-vacuum interface remains motionless so there is a region $\rho \in [\rho_2, 1]$ in which the displacement vanishes. The simplest approach is to set $\rho_1 = \rho_2$. This leads to the step function which has been established (for $\rho_1 = 0.5$) in equation 4.23. With this approach flux surfaces merge mathematically at $\rho = 0.5$ and magnetic reconnection occurs. Nevertheless the step-function displacement is a well known approach in ideal-MHD because the infinitesimal interval $\rho \in [\rho - \delta, \rho + \delta]$ where reconnection occurs is not taken into account.

We now remove this limitation by considering the simplest structure for the $\rho_1 \neq \rho_2$ case. In order to study the structure of ξ_0 inside the $\rho \in [\rho_1, \rho_2]$ region it is, in this thesis, heuristically parametrized by:

$$\xi_0 = \begin{cases} \zeta_0 & \rho \in [0, \rho_1) \\ \frac{1}{2}\zeta_0(\cos(\pi \frac{\rho - \rho_1}{\rho_2 - \rho_1}) + 1) & \rho \in [\rho_1, \rho_2] \\ 0 & \rho \in (\rho_2, 1] \end{cases} \implies \frac{d\xi_0}{d\rho} = \begin{cases} 0 & \rho \in [0, \rho_1) \\ \frac{\pi}{2(\rho_1 - \rho_2)}\zeta_0 \sin(\pi \frac{\rho - \rho_1}{\rho_2 - \rho_1}) & \rho \in [\rho_1, \rho_2] \\ 0 & \rho \in (\rho_2, 1]. \end{cases} \quad (5.1)$$

The parametrization depends on the parameters ρ_1, ρ_2 and ζ_0 . In figure 5.1 the displacement defined in equation 5.1 is compared with the step function displacement.

In this thesis ideal MHD is considered and in this framework the flux surfaces do not reconnect. In equation 5.1 a displacement function $\xi_0(\rho)$ with non-vanishing derivative is defined and it is shown in the following that the maximal absolute slope of the displacement

$$|\xi_0'(\rho_{cent})| = \left| \frac{\pi}{2(\rho_1 - \rho_2)} \zeta_0 \right| \quad (5.2)$$

at $\rho_{cent} = \rho_1 + \frac{1}{2}(\rho_2 - \rho_1)$ given in equation 5.1 is limited by the condition of non-connectivity.

According to equation 1.8 the radial flux coordinate $\rho(r)$ is monotonically increasing with the small radius r because ψ_{pol} is monotonically increasing with the small radius r . Reconnecting the flux surfaces would mean that ρ' is not monotonically increasing. Let us consider the $\cos(m\theta + n\phi + \omega t) = \pm 1$ manifold where the radial displacement is extremal and, according to equation 4.27,

$$\rho' = \rho \pm \xi_\rho \quad (5.3)$$

holds.

Since the flux surfaces do not reconnect it is required for ρ' to be monotonically increasing which means, that

$$\frac{d\rho'}{d\rho} > 0 \quad (5.4)$$

holds. Combining equations 5.3 and 5.4 leads to

$$1 \pm \frac{d\xi_\rho}{d\rho} > 0 \implies \left| \frac{d\xi_\rho}{d\rho} \right| < 1 \quad (5.5)$$

If the condition 5.5 is fulfilled the flux surfaces do not reconnect (ideal MHD) and this condition limits the maximal absolute slope of ξ_ρ . The displacement functions parametrized like in equation 5.1 which are considered in this thesis (except the step function) fulfill the above condition.

5.1 Impact of the displacement variation

Before we turn to the experimental investigation of internal (1,1) kink modes in section 6 we investigate the properties of the virtual cameras (introduced in section 3) and the model for mode perturbed emissivity (introduced in section 4) by varying the displacement and the emissivity independently from each other.

The author of [22] discussed a simple analytical model for the emissivity of modes and considered a line integration to calculate the resulting signal. With this procedure it is possible to understand the mode amplitudes and the mode phases qualitatively.

In the following it is shown, that it is, furthermore, possible to describe the effects also quantitatively using the virtual diagnostics (with all the three-dimensional geometry considered) and a realistic model for the mode perturbed emissivity.

We start with the variation of the displacement and let the mean emissivity be fixed and given by

$$e(\rho) = e^{-(2\rho)^2} - e^{-4} \quad (5.6)$$

with $e(1) = 0$. The equilibrium in which the calculations are carried out is given by the one which is calculated by the equilibrium code CLISTE for the discharge #26355 at $t = 2.15$ s.

Using the parametrization for the displacement ξ_0 in equation 5.1 the impact of the variation of the displacement on the (1,1) amplitudes and phases is investigated.

In the comparison visualized in figure 5.1 the impact of different slopes of ξ_0 is investigated. In the region $\rho \in [\pm 0.1, \pm 0.3]$ the different displacements cause a difference in the amplitudes: the higher the displacement ξ_0 at ρ_{local} is the higher is, the amplitude of the channels which tangent at approximately ρ_{local} . In the region $\rho \in [0.0, \pm 0.1]$ the different displacements cause no change in the amplitude although the VOS sees through the region of different displacement. The changes in the phases are only marginally.

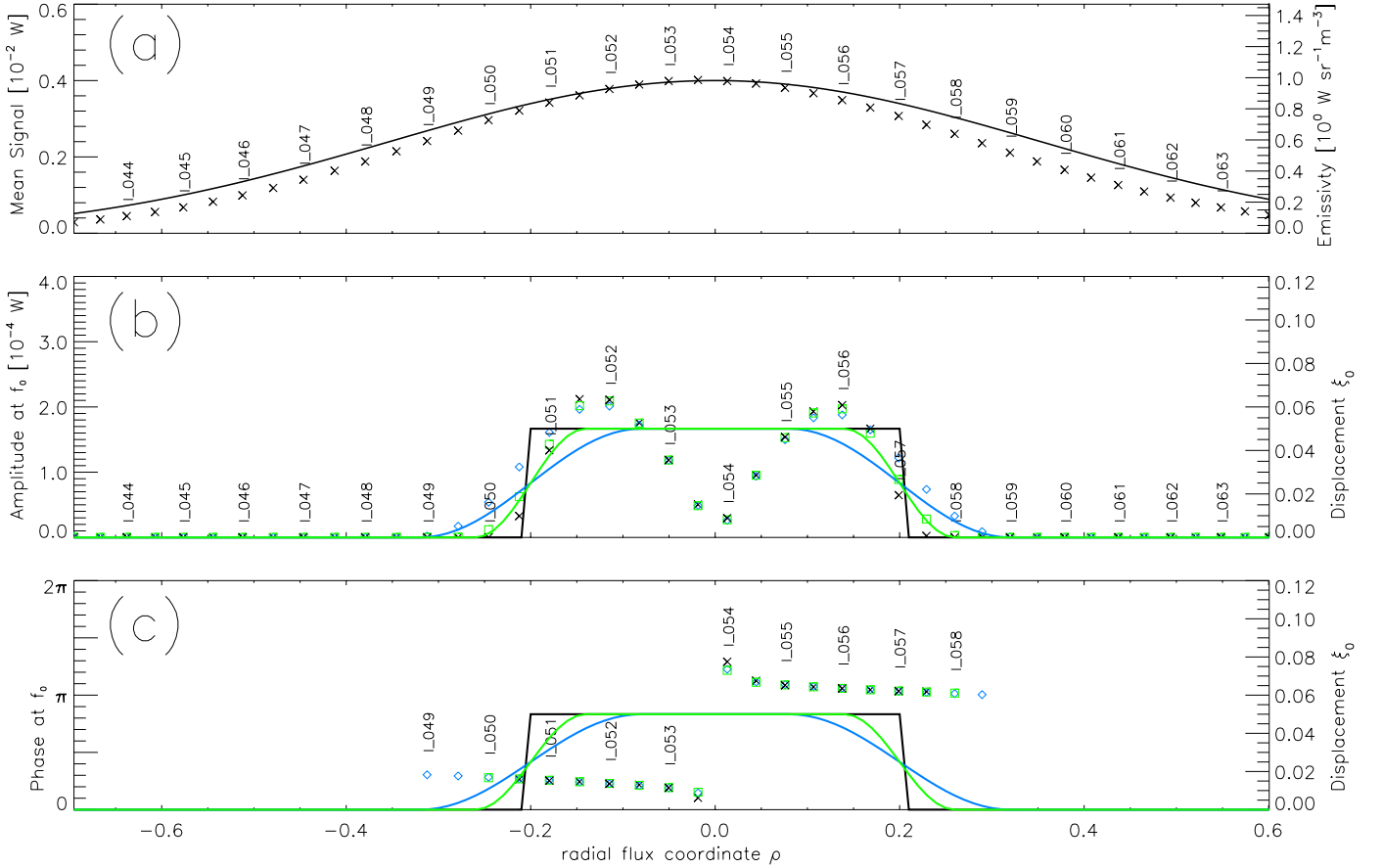


Figure 5.1 – Comparison of displacements ξ_0 with different slopes. The parameters are given by: $(\rho_1, \rho_2, \zeta_0) \in \{(0.08, 0.32, 0.05), (0.14, 0.26, 0.05), (0.2, 0.2, 0.05)\}$.

The two-dimensional displacement which results from the displacement-functions $\xi_0(\rho)$, $\xi_0(\rho)$ and $\xi_0(\rho)$ is visualized in figure 5.2.

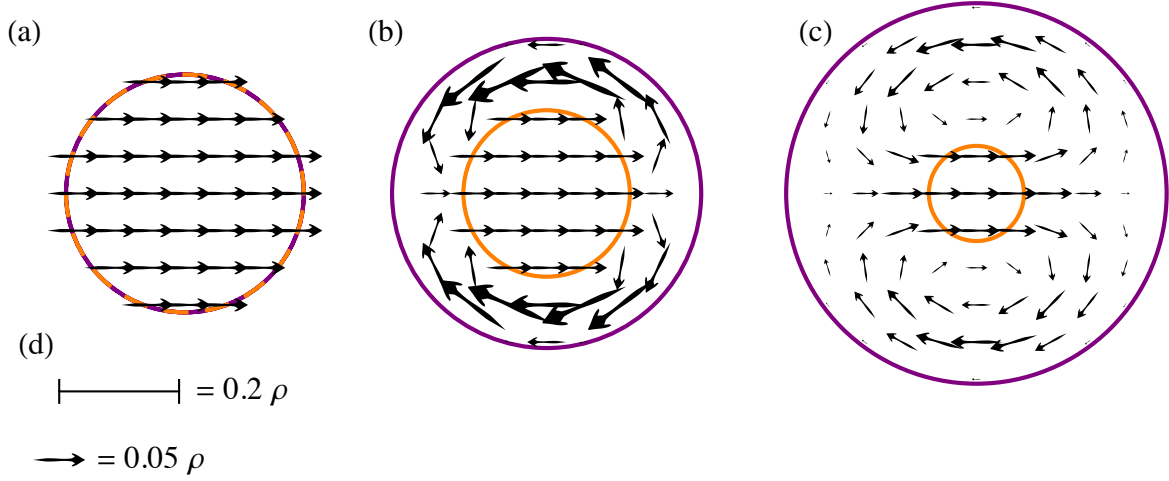


Figure 5.2 – Displacement resulting from the displacement functions $\xi_0(\rho)$ (a), $\xi_0(\rho)$ (b) and $\xi_0(\rho)$ (c). The circle radii correspond to the parameters (ρ_1, ρ_2) in figure 5.1. For (a) $\rho_1 = \rho_2 = 0.2$, for (b) $\rho_1 = 0.14$, $\rho_2 = 0.26$ and for (c) $\rho_1 = 0.08$, $\rho_2 = 0.32$. The scale of the flux surfaces and the scale of the vector field is indicated in (d).

A similar flow-pattern of the internal $m = 1$ kink mode can also be found in [6] on page 331. The following discussion of figure 5.2 is inspired by the author of [23]. Inside the flux surface with radius ρ_1 there is a rigid displacement of the plasma and the plasma outside the ρ_2 circle remains motionless. The displacement is constructed in such a way that the plasma is incompressible. So in the region between ρ_1 and ρ_2 the plasma is pushed with a high displacement in θ -direction. And the smaller the $[\rho_1, \rho_2]$ region is the higher is the displacement ξ_θ in this region. Note that the impact of the displacement in θ -direction ξ_θ on the signals is small compared with the impact of the displacement ξ_ρ because the emissivity profile $e_0(\rho)$ is symmetric in θ , i.e. $e_0(\rho)$ has no θ -dependence.

In figure 5.3 the height ζ_0 of the displacement is varied considering a constant decay range $[\rho_1, \rho_2]$. The doubling of the displacement cause a doubling in the amplitudes. There is no significant change in the phases.

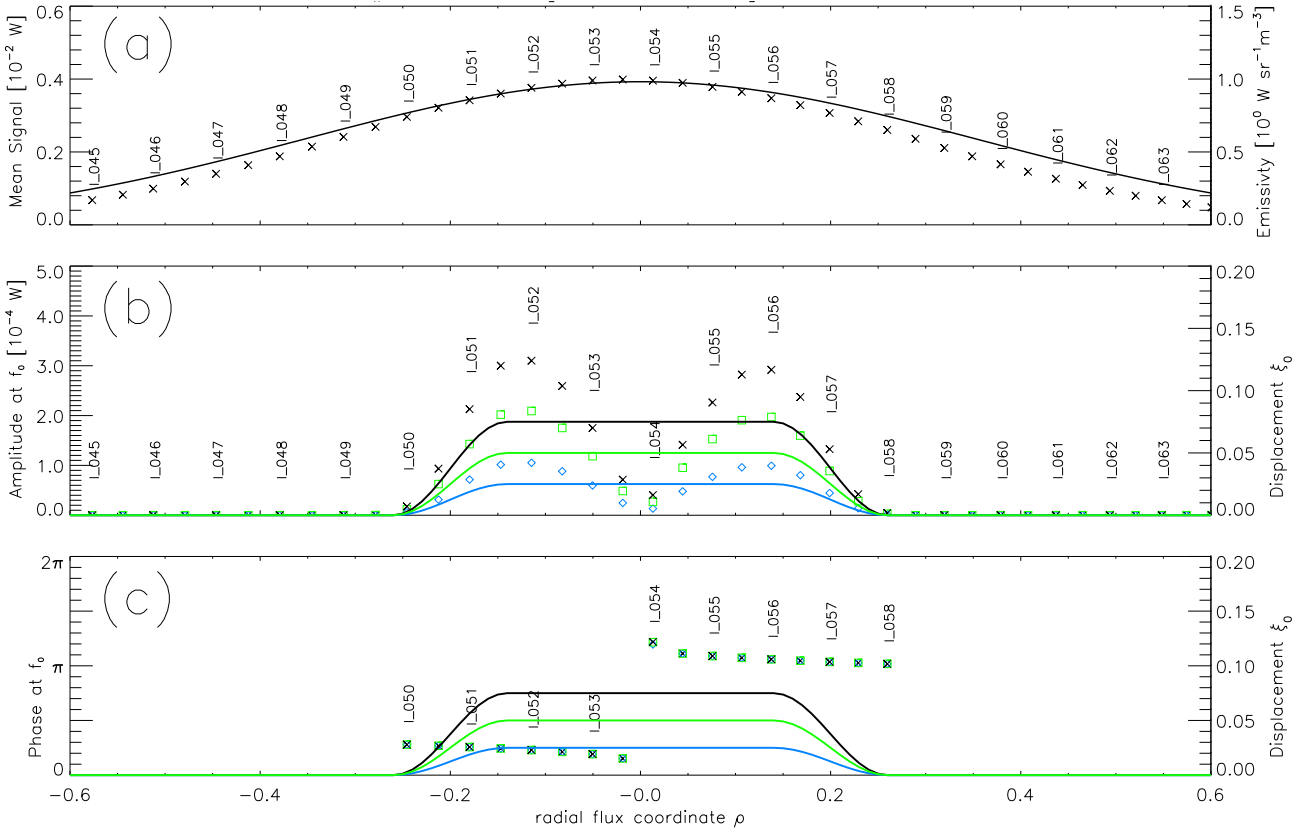


Figure 5.3 – Comparison of displacements ξ_0 with different height. The parameters are given by: $(\rho_1, \rho_2, \zeta_0) \in \{(0.14, 0.26, 0.025), (0.14, 0.26, 0.05), (0.14, 0.26, 0.075)\}$. In (a) the mean signals resulting from the displacement $(\rho_1, \rho_2, \zeta_0) = (0.14, 0.26, 0.075)$ is shown with \times .

For the situation presented in figure 5.3 for the channel I_{055} a time trace is plotted in figure 5.4.

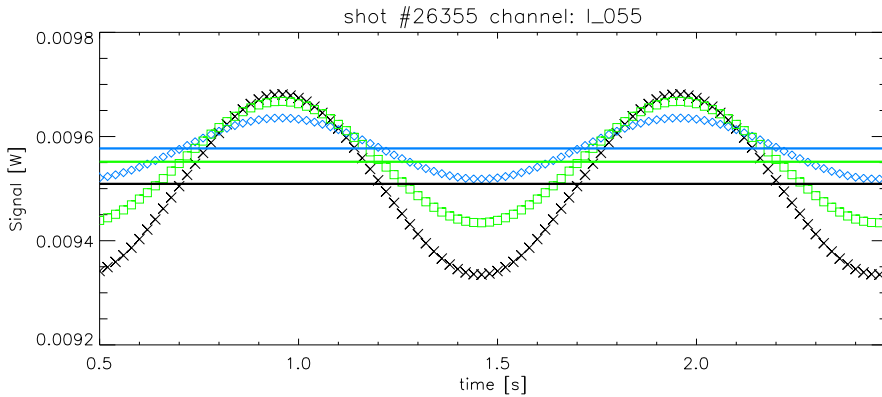


Figure 5.4 – Time traces of the simulated signals resulting from channel I_{055} . The color corresponds to the color of the displacement function in figure 5.3.

In figure 5.4 the corresponding mean signals are plotted with a horizontal line. The larger the displacement the lower the mean signal. Due to the displacement the maximal signal is increased and the minimal signal is decreased and the effect is bigger the bigger the displacement is. This is because the emissivity profile is peaked, which means, that the emissivity rises monotonically towards the magnetic axis and the higher the displacement is the more inner and the more outer regions of emissivity are *seen* by the channel I_{055} . Finally, an increase in the displacement causes the mean signal to decrease because the decrease of the signals is stronger than the increase of the signals.

This example shows, that the mean signal can depend on the displacement. In the following it is explained that in general there is coupling between the mean signal and the displacement. Let us assume, there is a measured time trace for channel I_{055} which is to be reconstructed. The mean signal of I_{055} is lowered by the displacement. The effect can be compensated by raising the emissivity profile function $e_0(\rho)$ which results from the least square fit in the region where I_{055} is tangent to the flux surface. But the change of the emissivity profile may change the emissivity gradient, which will have an impact on the simulated amplitude. So, the displacement is to be adjusted which will again change the mean signal. There is an infinite loop which converges because the coupling effect gets smaller from step to step.

The important point is, that in general the fitting of the background emissivity can not be separated from the fitting of the displacement (and vice versa) because there is coupling between them and an appropriate approach is to implement a fit routine where the parameters of the background emissivity and the parameters of the displacement are varied simultaneously in order to find the best fit result for both.

In figure 5.5 the expansion of the displacement is varied: with $[\rho_1 + c, \rho_2 + c]$ being the decay range c is varied. An increase of the expansion of the displacement causes the amplitudes to expand and to increase in height. The value of the amplitude increases because the volume of the emissivity which is moved increases. The changes in the phases of the central channels are only marginally.

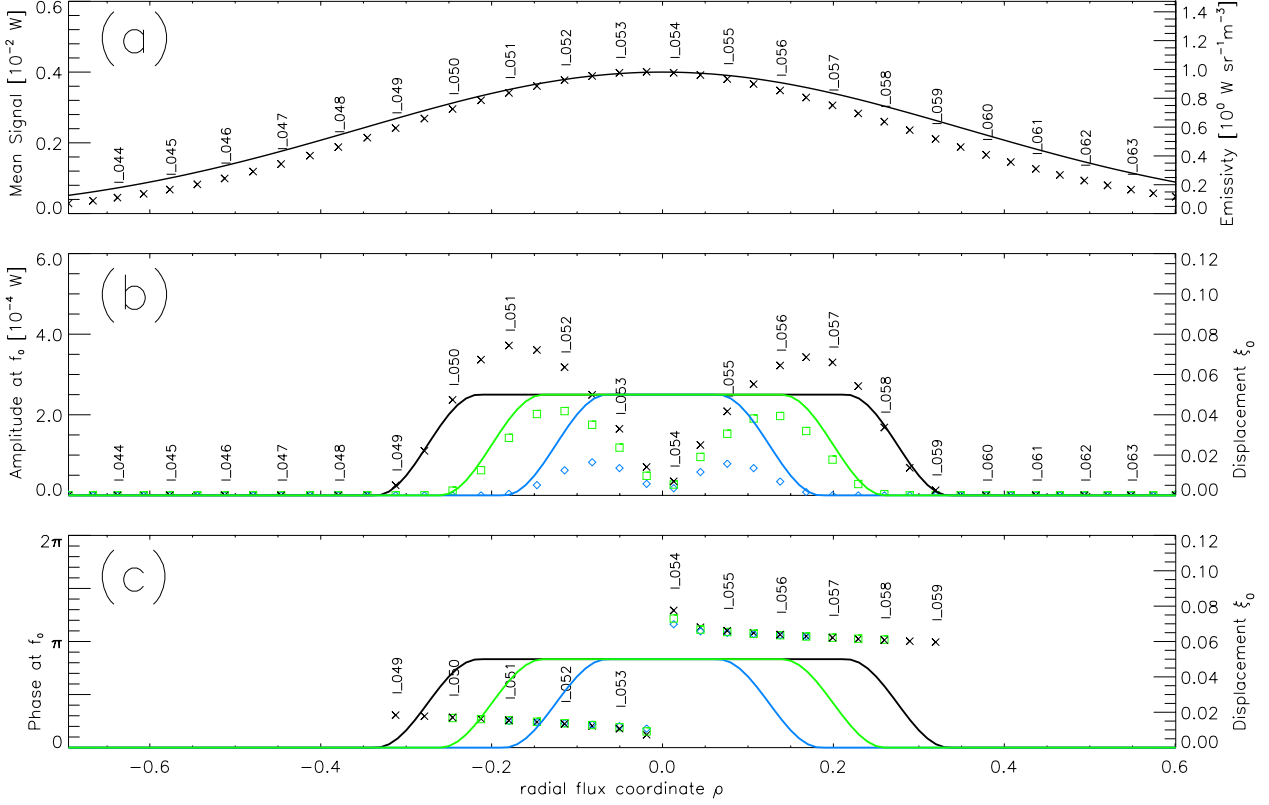


Figure 5.5 – Comparison of different expansion of displacements ξ_0 . The parameters are given by: $(\rho_1, \rho_2, \zeta_0) \in \{(0.065, 0.185, 0.05), (0.14, 0.26, 0.05), (0.215, 0.335, 0.05)\}$.

It is shown in this section that, under the condition of an existing emissivity gradient, different displacements ξ_0 cause different amplitude-values. For all examples the amplitude is higher the higher the displacement is and the phases are almost independent of a variation of the displacement. Note that all the results depend on the gradient of the emissivity profile $e_0(\rho)$. This dependency is discussed in the next section.

5.2 Impact of emissivity variation

Now the previous section is supplemented by an analogous investigation for the variation of the mean emissivity. Let the displacement be fixed and given by equation 5.1 with the parameters $(\rho_1, \rho_2, \zeta_0) = (0.3, 0.4, 0.05)$ and let the emissivity (which will be varied) be given by a natural cubic spline with 11 nodes at $\rho_i = i/10$ and $i = 0, 1 \dots, 10$. Let the emissivity-values at the nodes ρ_i be given by

$$e(\rho_i) = 10^{-4} \cdot [10.0, 8.6, 5.9, 3.4, 1.3, 1.1, 0.6, 0.5, 0.2, 0.2, 0.1]_i. \quad (5.7)$$

Now the impact of the variation of the mean emissivity on the amplitudes and on the phases is investigated. Starting with the emissivity profile e_0 which is a natural cubic spline with node-values defined in equation 5.7 an ensemble of 22 mean emissivity spline-functions $e_0^{(\pm i)}$ are created by the following procedure. The functions $e_0^{(\pm i)}$ and e_0 differ only at the i -th node ρ_i by a constant: $e_0^{(\pm i)}(\rho_i) = e_0(\rho_i) \pm \Delta e$. The constant Δe is chosen to be 10% of the maximal emissivity $\Delta e = 10^{-4}$ and for nodes with a low emissivity the constant $-\Delta e$ is increased in such a way that the emissivity stays non-negative. For every $e_0^{(\pm i)}$ the resulting signals, amplitudes and phases are calculated for every virtual channel. For every virtual channel the minimal and the maximal signal, amplitude and phase is considered and the colored areas in figure 5.6 are bounded by these extremal values.

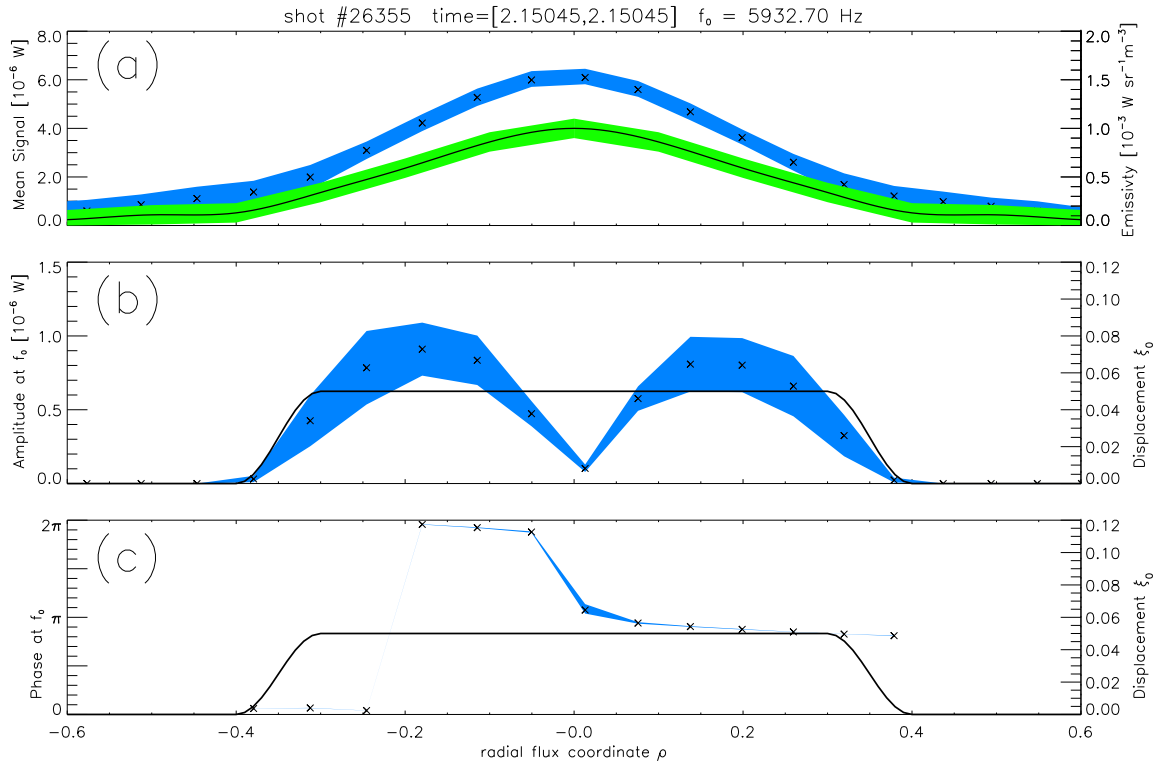


Figure 5.6 – The mean emissivity is varied within the green colored area in (a). In (a) the impact on the signals in (b) on the amplitudes and in (c) on the phases is visualized. The displacement function $\xi_0(\rho)$ is shown in (b) and (c).

According to the data which is plotted in figure 5.6 a variation of $\pm 10\%$ of the emissivity profile cause a maximal change of only $\pm 8\%$ in the signal. This is because the changed region is only a small part of the overall emissivity inside the VOS and the VOS is quite big. For the reconstruction of the background emissivity profile $e_0(\rho)$ it would be beneficial, if it were the other way around. The above variation in the emissivity profile cause changes of maximal $\pm 32\%$ in the amplitudes. The maximal change of the phases is only $\pm 6\%$ at the most central channel at $\rho \approx 0$.

A deeper insight in the reason for the change in the amplitudes is given by the variation of the emissivity at single node which is visualized in figure 5.7.

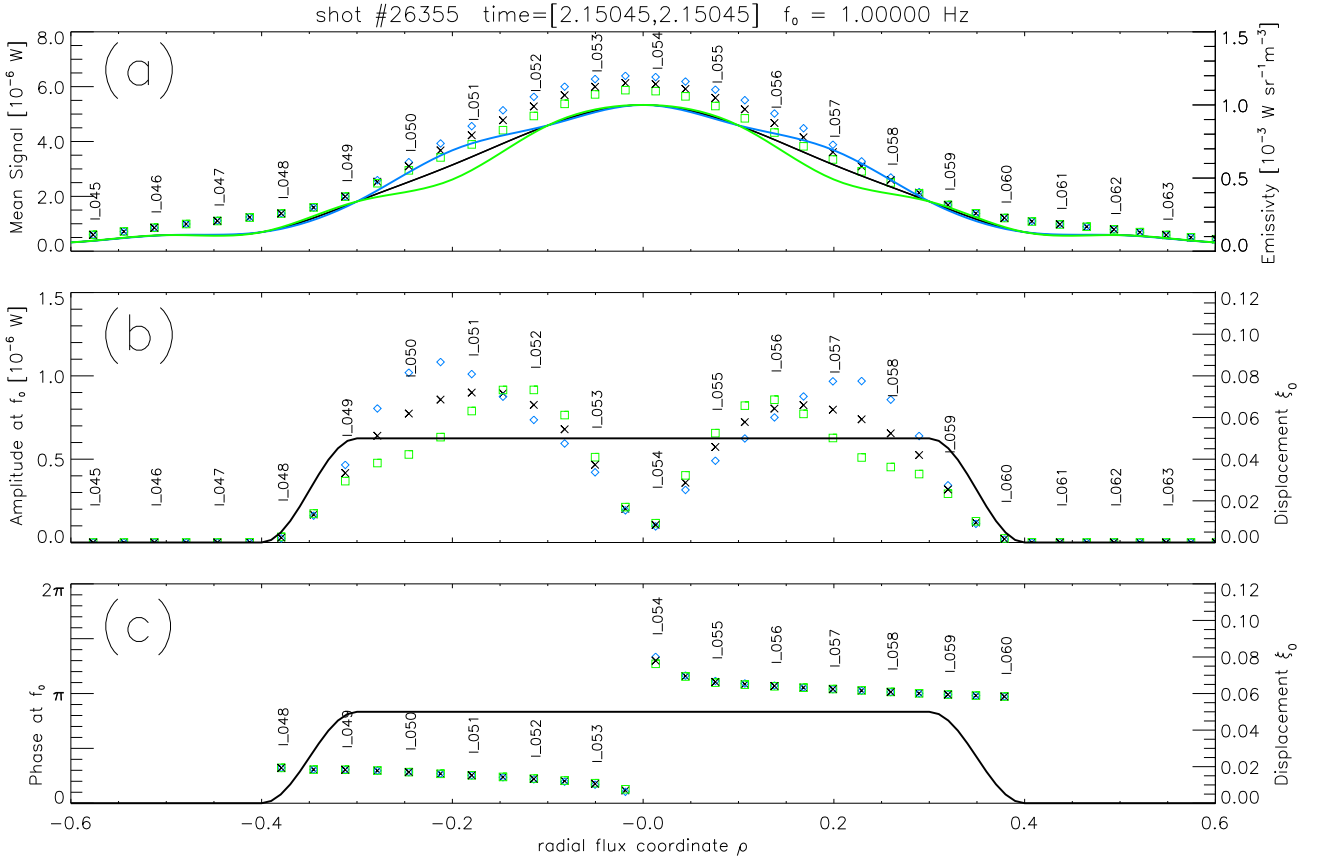


Figure 5.7 – The emissivity is varied at the node $\rho_2 = 0.2$. The impact on the amplitudes and on the phases are visualized in the corresponding color.

The emissivity $e^{(0)}$ with line-style — in figure 5.7 (a) is a natural cubic spline which is defined by the data in equation 5.7. For the emissivity $e^{(1)}$ with line-style — the value of the emissivity at $\rho_2 = 0.2$ is decreased by $\Delta e = 10^{-4}$ and the emissivity $e^{(2)}$ with line-style — it is increased by Δe . The resulting mean signals, amplitudes and phases are plotted with the corresponding color in figure 5.7.

First the impact on the mean signals in figure 5.7 (a) is discussed. In the region $\rho \in (\pm 0.1, \pm 0.3)$ the emissivity $e^{(1)}$ is smaller than the emissivity $e^{(2)}$. This causes the mean signal with the plot mark \diamond (\square) in the region $[0, \pm 0.3)$ to be higher (lower).

The impact of the change of the emissivity on the mean signals of the tangent channels $I_{_050}$ and $I_{_058}$ is comparatively small because the VOS of these channels see the region with changed emissivity only once whereas the central channels $I_{_052}$ to $I_{_056}$ break-through the region with changed emissivity twice.

Now the impact on the amplitudes in figure 5.7 (b) of the signals is discussed. In the region $\rho \in (0.2, 0.3]$ the absolute gradient of the emissivity $e^{(2)}$ is higher compared to the absolute gradient of the emissivity $e^{(1)}$ and in the region $\rho \in [0.1, 0.2)$ it is the other way around. This causes the amplitudes in the region $\rho \in [\pm 0.15, \pm 0.3]$ with plot mark \diamond to be higher than the amplitudes with plot mark \square . And in the region $\rho \in [0.0, \pm 0.15)$ it is the other way around.

The effect results from the fact that with a fixed displacement the change of emissivity inside the VOS is greater, the greater the gradient of the emissivity profile is. Note that the amplitude of a channel is a measure of the change of the emissivity in the VOS and the amplitude is invariant under the transformation of the emissivity $e \rightarrow e + c$ whereas c is a constant.

A similar analysis of varying the emissivity spline at $\rho_0 = 0$ shows that this results in a small change in the central phase at $\rho \approx 0$. This corresponds to the phase change of the most central channel in figure 5.6.

In the next comparison hollow emissivity profiles are studied. A background emissivity profile $e_0(\rho)$ is called to be hollow if the central emissivity $e_0(\rho \approx 0)$ is not the maximal emissivity. For almost all observed cases of hollow emissivity profiles in AUG the temperature profile $T_e(\rho)$ and the density profile $n_e(\rho)$ are peaked (not hollow) and therefore it is assumed that the hollowness is due to a hollow tungsten density [34]. Let the emissivity be given by a natural cubic spline with the following emissivity-values at the nodes ρ_i :

$$\begin{aligned} e_1(\rho_i) &= [4.5, 6.0, 5.7, 2.0, 0.3, 0, 0, 0, 0, 0, 0]_i \\ e_2(\rho_i) &= [3.0, 6.4, 5.7, 2.0, 0.3, 0, 0, 0, 0, 0, 0]_i \\ e_3(\rho_i) &= [1.5, 6.8, 5.7, 2.0, 0.3, 0, 0, 0, 0, 0, 0]_i \end{aligned}$$

The results are visualized in figure 5.8.

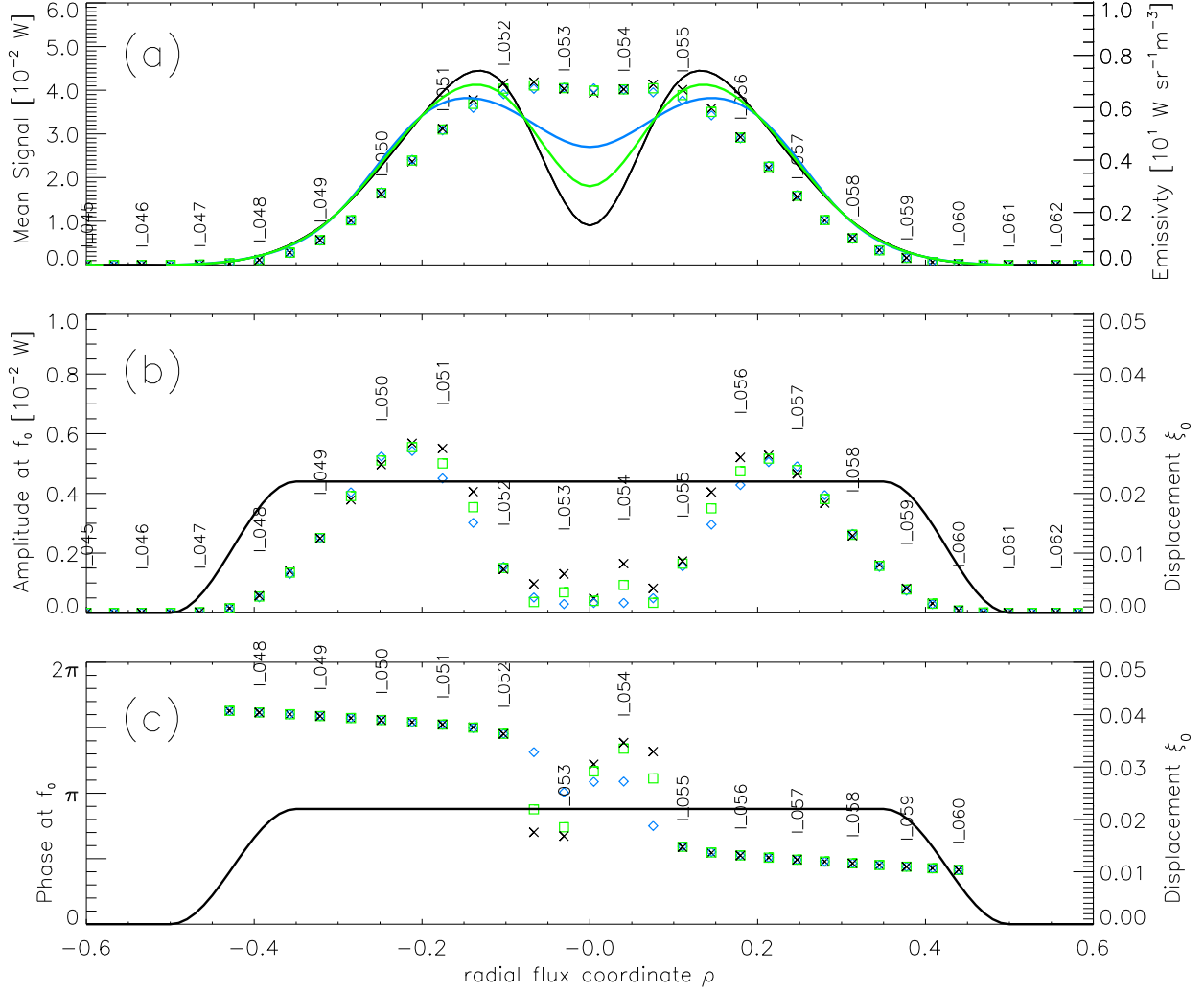


Figure 5.8 – The hollowness of the emissivity profiles $e_1(\rho)$, $e_2(\rho)$ and $e_3(\rho)$ plotted in (a) are varied at the nodes ρ_1 and ρ_2 . The impact on the signals (a), the amplitudes (b) and on the phases (c) are visualized in the corresponding color.

First the mean signals resulting from the emissivity profile $e_1(\rho)$ and $e_3(\rho)$ are compared. The emissivity of $e_3(\rho)$ is lowered in the region $\rho \in [0, \pm 0.08]$ and it is raised in the region $\rho \in [\pm 0.08, \pm 0.2]$ compared to $e_1(\rho)$. The impact of the enormous emissivity profile change on the mean signals is marginal because the channels which *see* the lowered emissivity also *see* the raised emissivity and the two effects compensate each other almost totally. Therefore it is almost impossible to reconstruct the exact hollow structure of a measured hollow background emissivity only with the mean signals given.

Note that the resolution of the plasma center is poorer compared to outer regions. This is because a channel which tangents at ρ_{tan} *sees* all the plasma in the region $\rho \in [\rho_{tan}, 1]$. And only a channel which tangent the center *sees* the center. So only a comparably small number of channels *see* the plasma center.

Now we turn to a comparison of the phases. For the emissivity profile $e_3(\rho)$ there

are two additional phase jumps at $\rho \approx \pm 0.08$. There is a rather simple explanation for the additional phase jumps which is here carried out for the channels $I_{_055}$ and $I_{_054}$: the signal for $I_{_055}$ and $I_{_054}$ are inversely phased because a maximal signal in $I_{_055}$ correspond to a minimal signal in $I_{_054}$. The additional phase jumps of the emissivity profiles $e_1(\rho)$, $e_2(\rho)$ are not fully developed because the region of hollowness $\rho \in [-0.08, 0.08]$ is small and the VOS also *sees* through regions of non hollowness $[\pm 1, \pm 0.08]$ so there are also contributions from non-hollowness-regions which have a different phase.

The increase of the degree of hollowness also has an effect on the amplitudes: the greater the hollowness the greater the emissivity gradient and the higher the simulated amplitudes.

The impact of the hollowness on the amplitudes and on the phases is quite big and therefore the amplitude and phase structure can be a criterion for the hollowness of an emissivity profile.

In this section it has been shown, that the amplitudes depend very sensitively on the emissivity gradient. This restricts the accuracy of the reconstruction of the magnetic structure which is performed in section 6.

5.3 Impact of the equilibrium variation

In this chapter the impact of a change of the equilibrium is investigated. For some discharges the equilibrium geometry calculated with the used equilibrium code (CLISTE) is not correct, especially in the plasma center.

The flux surfaces for the shot #26355 and for the time point 2.15 s are visualized with black lines in figure 5.9. These flux surfaces are modified by a rigid shift in R-direction. The resulting flux surfaces are visualized in blue for $\delta R = -5\text{cm}$ and in green for $\delta R = 5\text{cm}$. Using the background emissivity defined with the spline in equation 5.7 the

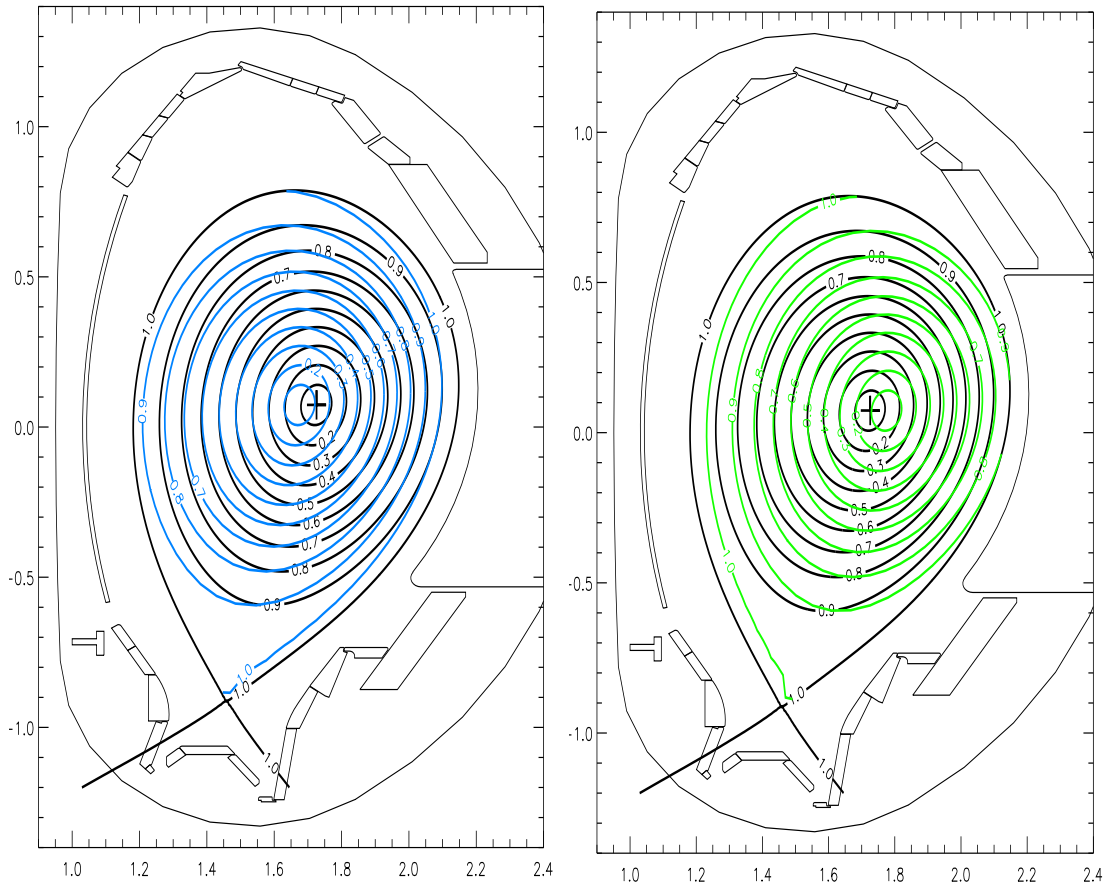


Figure 5.9 – The unmodified flux surfaces in black and the shifted flux surfaces are shown in blue and green. The axes correspond to R and z and the units are meters.

impact on the simulated signal is investigated. As explained in section 2.1 each channel is labeled with a positive or negative ρ_{tan} . Where ρ_{tan} is the flux coordinate of the flux surface on which the AVOS tangents. With the change of the equilibrium also the flux surface on which the AVOS tangents is changed. For reasons of simplicity the signals are plotted in x-direction at the ρ_{tan} -value of the unchanged equilibrium in figure 5.10. The simulation results are shown in figure 5.10.

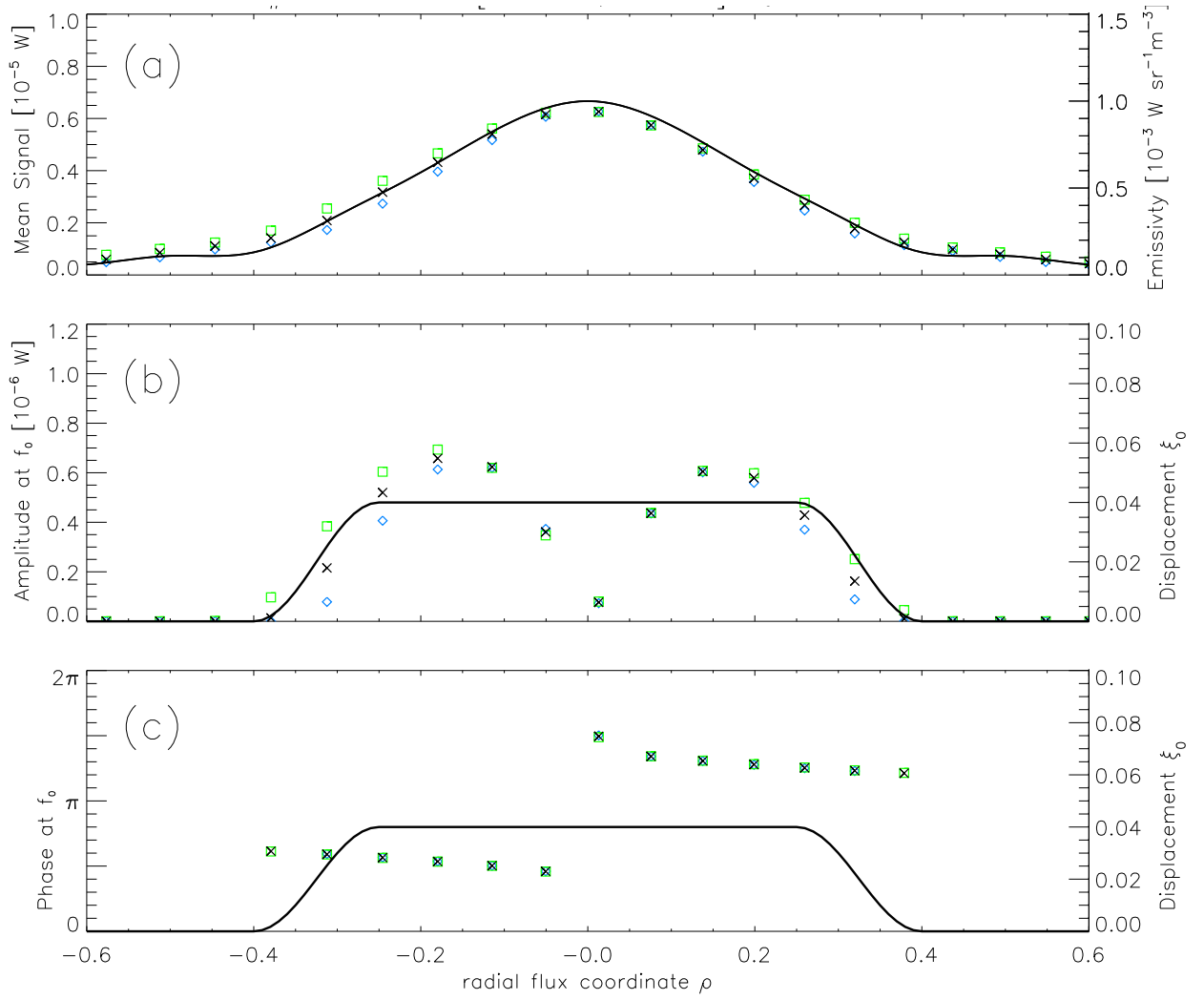


Figure 5.10 – Results of the rigid equilibrium shift.

Camera I is located at the LFS and the VOS point to the HFS. The central channels of the camera point approximately towards the plasma center. The impact of a change of the equilibrium position on the central channels is marginal. This is because the central channels *see* the same flux surfaces with and without the equilibrium shift.

For the channels in the region $\rho \in [\pm 0.175, \pm 0.6]$ the mean signals in figure 5.10 (a) change. For the shift $\delta R = 5$ cm (green flux surfaces) flux surfaces with higher emissivity are shifted inside the VOS and the signals increase. Accordingly, for the shift $\delta R = -5$ cm (blue flux surfaces) the signals decrease. For the change of the amplitudes in figure 5.10 (b) the same explanation holds. Figure 5.10 (c) shows that the rigid shift of the equilibrium does not change the phases of the signals.

Instead of applying a rigid shift in R-direction the flux surfaces can also be shifted with respect to each other. Let ρ_{old} be the flux coordinate of the unmodified equilibrium. The flux surfaces inside the $\rho_{old} \in [0, 0.3]$ region are displaced with a rigid shift (in R-direction) and the flux surfaces inside the $\rho_{old} \in [0.7, 1.0]$ region are not modified. In the region $\rho \in [0.3, 0.7]$ the change from the shifted to the unshifted flux surfaces is smooth. This is accomplished by considering a linear combination of the (rigid) shifted flux ρ_{new} and the unshifted flux ρ_{old} :

$$\rho_{final}(R, z) = \begin{cases} \rho_{old}(R, z) & \rho_{old}(R, z) \leq 0.3 \\ \rho_{new}(R, z) & \rho_{old}(R, z) \geq 0.7 \\ \rho_{new}(R, z)f_{mix} + \rho_{old}(R, z)(1 - f_{mix}) & 0.3 < \rho_{old}(R, z) < 0.7 \end{cases} \quad (5.8)$$

In the region of overlap the weight-function provides a smooth change from ρ_{old} to ρ_{new} . Where the weight-function is given by $f_{mix}(0.3, 0.7, 1.0) = \xi_0(0.3, 0.7, 1.0)$ with the parametrization of $\xi_0(\rho_1, \rho_2, \zeta_0)$ given in equation 5.1. The final coordinate ρ_{final} in the outer part of the plasma is given by $\rho_{final} = \rho_{old}$ and in the inner part of the plasma the final coordinate is given by $\rho_{final} = \rho_{new}$.

The resulting geometry of the flux surfaces are visualized in figure 5.11:

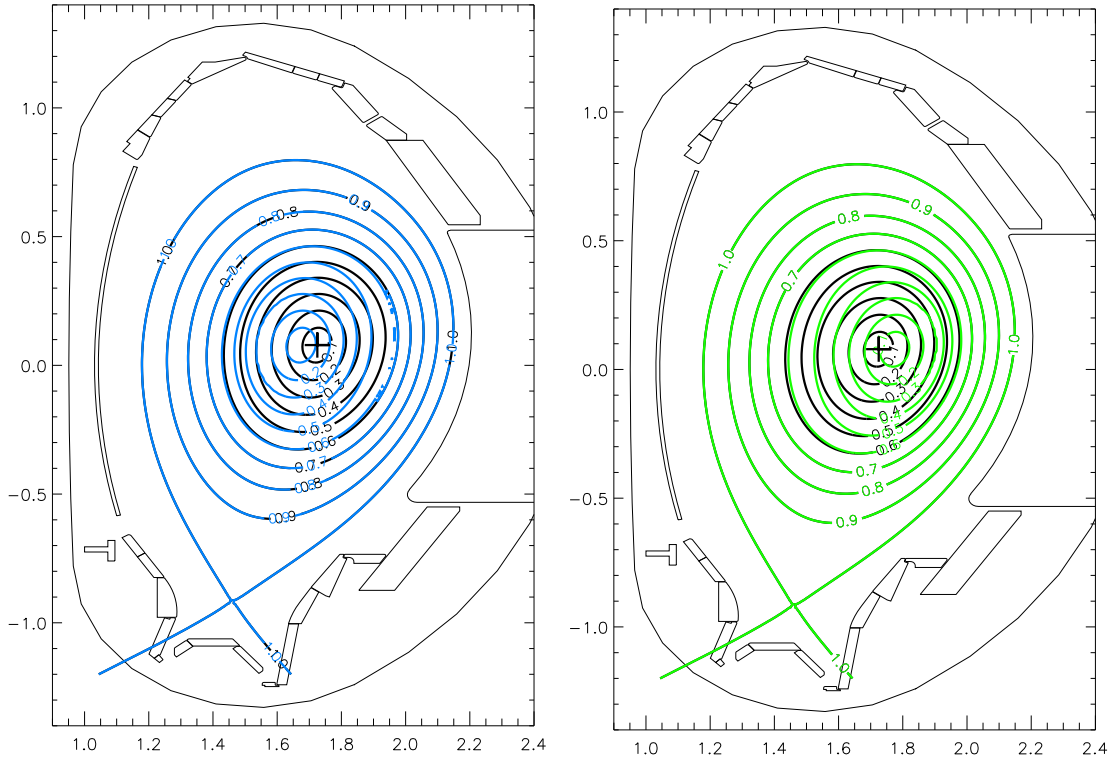


Figure 5.11 – The unmodified flux surfaces in black and the shifted flux surfaces are shown in blue and green. The axes correspond to R and z and the units are meters. Note that only the inner flux surfaces are shifted and the outer flux surfaces are not modified. There is a smooth change in between.

The resulting signals, amplitudes and phases of the simulation are shown in figure 5.12:

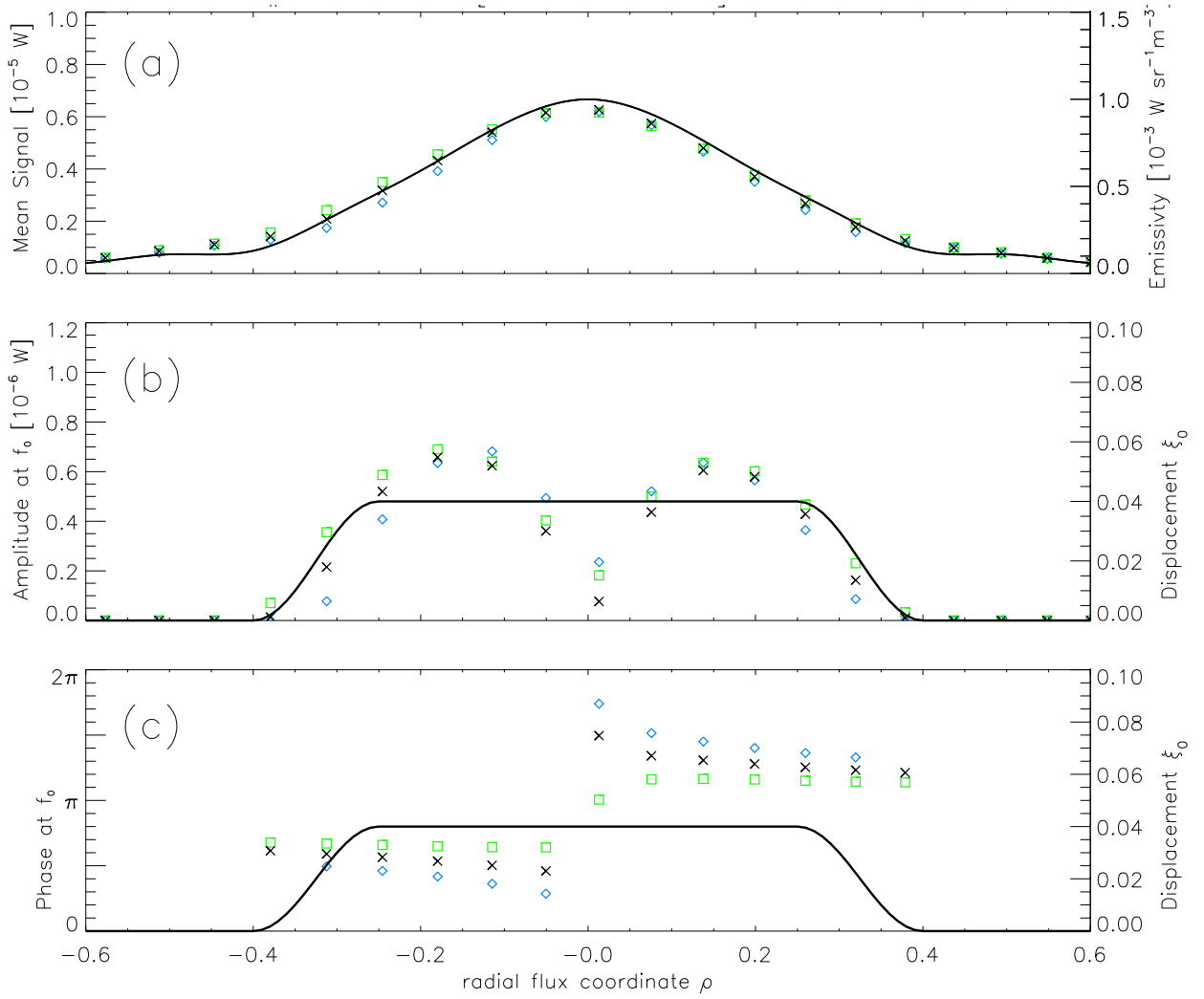


Figure 5.12 – Results of equilibrium shift with flux surface deformation.

The signals and the amplitudes in the region $\rho \in [\pm 0.175, \pm 0.6]$ in figure 5.12 (a) and (b) are changed just like discussed for figure 5.10. This type of plasma shift is more realistic, because the position of the separatrix is much better defined than the position of the magnetic axis and the positions of the inner flux surfaces.

The change of the inner flux surfaces cause an additional change in the central amplitudes and, most important, the phases of all channels change. The phases distance of the channels change if the positions of the inner flux surfaces are modified with respect to the outer flux surfaces.

This is an interesting point, because the conditions for a change of the phases are very specific: a hollow emissivity profile or a change of the inner equilibrium flux surface position with respect to the outer flux surfaces changes the phases of the signals. The phases remain unchanged by modifying the displacement function $\xi_0(\rho)$, by modifying the gradient of the background emissivity $e_0(\rho)$ (except the change of sign which occurs

at hollow profiles) or by a rigid shift of the whole plasma equilibrium.

In this idealized example the shift of $\Delta R = 5\text{cm}$ is exaggerated. In reality we expect the shift of the plasma center to be approximately 2cm.

In order to test whether the phase change in the signals are effected by the geometry of the VOS the pinhole width and the pinhole length are modified. It turned out, that the phases remain unchanged by a significant change of the VOS.

The above change of the position of the inner flux surfaces is a simple model for the Shafranov shift. The Shafranov shift moves inner flux surfaces with increasing β stronger to the LFS compared to outer flux surfaces. The magnetic axis (center of mass of the flux surface with $\rho \rightarrow 0$) is moved to the LFS compared to the center of mass of the plasma cross section.

The Shafranov shift calculated with the equilibrium code (CLISTE) is smaller than the shift chosen for this idealized example. So with the blue shift in figure 5.12 the Shafranov shift is overcompensated. The resulting inner flux surfaces have a shift opposite to the direction of the Shafranov shift.

With the green shift the Shafranov shift is boosted with an unrealistic high shift.

The phase change of this idealized example in comparison with the measured phases in the next section 6 is a hint, that the Shafranov shift calculated with CLISTE may be too high.

6 Experimental investigation of (1,1)-kink modes

In section 5 the impact of a variation of the displacement and of the emissivity is discussed with the help of idealized examples. In this section the methods are applied to measured data and educated guesses are made for the magnetic structure of the observed kink modes. The magnetic structure of a kink mode is investigated with the following two steps.

By varying the emissivity $e_0(\rho)$ and the displacement $\xi_0(\rho)$ the time dependent simulated signals are varied until the chosen magnetic structure is consistent with the measured signals.

Because the emissivity function $e_0(\rho)$ is needed in order to apply the model of mode perturbed emissivity, first the equilibrium emissivity is reconstructed by varying the emissivity function $e_0(\rho)$ (at the 11 nodes) until measured and simulated signals fit best according to a least square test. This procedure is described in section 6.1. The signals resulting from the emissivity of mode perturbed plasma are simulated using the mean emissivity $e_0(\rho)$ from the first step and a displacement function $\xi_0(\rho)$. The displacement function $\xi_0(\rho)$ is then varied manually until measured and simulated amplitudes fit best. This procedure is described in section 6.2.

6.1 Fitting the equilibrium emissivity and its asymmetries

In this section the fitting of the equilibrium emissivity is exemplified. In the plasma discharge with discharge number #26355 in the time range [2.1503 s, 2.1508 s] there is a kink mode with the frequency of 5932.7 Hz.

In order to quantify the quality of a fit the residual sum of squares measure is used. The residual sum of squares (RSS) is given by

$$RSS = \sum_{i=1}^N (S_{sim}^{(i)} - S_{exp}^{(i)})^2, \quad (6.1)$$

whereas $S_{exp}^{(i)}$ and $S_{sim}^{(i)}$ is the simulated and the measured signal of the i-th channel and the RSS of N channels is calculated. The RSS-value is a measure for the quality of the fit and the lower the RSS is the better is the agreement between simulated and measured signals.

The fit-routine is started by loading the time-averaged measured signals of all the 192 camera channels. In order to calculate the simulated signal the virtual counterparts of the channels are initialized. The emissivity is given by a spline. A minimizer-algorithm varies the emissivity at the 11 nodes until an emissivity-spline is found which results in a minimal RSS. The fit converges and the best fit result is given by:

$$e_0(\rho_i) = 10^{-4} \cdot [9.5, 8.6, 5.9, 3.4, 1.3, 1.1, 0.6, 0.5, 0.2, 0.2, 0.1]_i \quad [Wsr^{-1}m^{-3}]. \quad (6.2)$$

For this case the corresponding signals and the corresponding emissivity profile are

plotted in figure 4.1. In order to concentrate on a certain aspect the data of figure 4.1 is replotted for the F and the I camera with signal names in figure 6.1.

shot # 26355 time = 2.15000

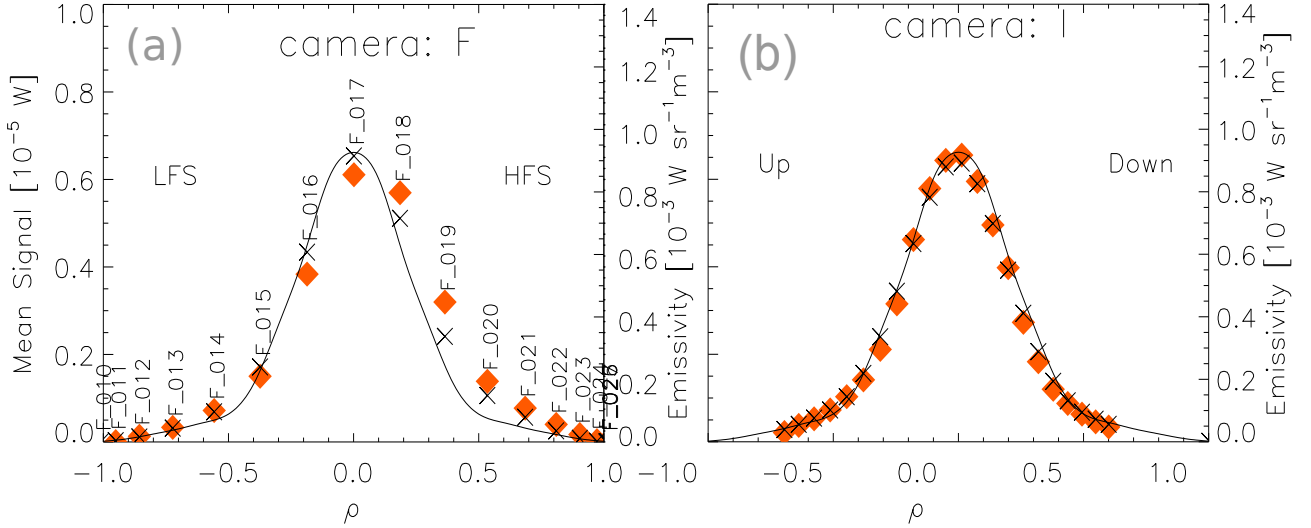


Figure 6.1 – Emissivity profile (—) with the axis on the right side. Measured (◆) and simulated signals (×) are plotted for the F and for the I camera with the axis on the left side.

In figure 6.1 (a) the simulated signals with the plot-marks ($\times F_{016}$, $\times F_{018}$) are called to be asymmetric to the measured signals which are plotted with the plot-marks (◆ F_{016} , ◆ F_{018}). This means the following. The signal (with plot mark) $\times F_{016}$ is higher than the signal ◆ F_{016} but the signal $\times F_{018}$ is lower than the signal ◆ F_{018} .

This asymmetry of the measured signals limits the achievable fit quality using the particular equilibrium and using the model of constant emissivity on flux surfaces: If the local emissivity at $\rho \approx 0.2$ is increased in order to get a better agreement between ($\times F_{018}$, ◆ F_{018}) then the emissivity in the region $\rho \approx -0.2$ is also increased and the agreement of the channels ($\times F_{016}$, ◆ F_{016}) gets worse. And if the local emissivity at $\rho \approx -0.2$ is decreased in order to get a better agreement between ($\times F_{016}$, ◆ F_{016}) the agreement of the channels ($\times F_{018}$, ◆ F_{018}) gets worse.

In conclusion, the quality of the fit presented in figure 6.1 is bad and due to the asymmetry it is not possible to increase the quality of the fit.

On one hand it is advantageous to use as much channels as possible to consider as much information as possible. On the other hand if there is an HFS/LFS asymmetry like in figure 6.1 (a) and almost no up/down asymmetry like in figure 6.1 (b) the quality of the fit considering only the I camera will be much better by considering only the measured signals from the I camera for the fit.

The two possible reasons for the observed asymmetries are discussed:

The first reason for an asymmetry could be that the equilibrium calculated with the used equilibrium code is not correct. These discrepancies are sometimes observed especially in the plasma center. If the asymmetry is exclusively due to discrepancies in the equilibrium, then the asymmetry will disappear if the fit is performed in a correct equilibrium.

Second the reason for an asymmetry could be an asymmetric impurity distribution. The HFS/LFS-asymmetry due to heavy impurity ions in fast rotating plasmas on which a centrifugal force acts is described in [39]. And the up/down-asymmetry due to the asymmetry of impurity density is also often observed and it is described in [40] and in [41].

Of course, these two reasons for an asymmetry can also be fulfilled simultaneously. If there is a instability present it may be possible to distinguish the two possible reasons for an asymmetry because the instability moves along the real equilibrium flux surface and it may be possible to reconstruct the flux surface geometry with good accuracy using the measured sxr signals. If the asymmetries do not disappear using the reconstructed equilibrium the emissivity asymmetries are probably due to an asymmetric impurity distribution.

6.2 The investigation of the magnetic-structure of a kink mode

In the previous section an observed kink mode has been introduced and the emissivity profile $e_0(\rho)$ is given by the fit which is described in section 6.1. The measured signals of the observed kink mode are reproduced by the simulation by varying the displacement. The displacement $\xi_0(\rho_1, \rho_2, \zeta_0, \rho)$ according to the parametrization in 5.1 is varied manually until the simulated amplitudes reproduce the measured amplitudes. The data plotted in figure 6.2 results from the emissivity spline given in equation 6.2 and from the displacement given by:

$$(\rho_1, \rho_2, \zeta_0) = (0.27, 0.37, 0.052) \quad (6.3)$$

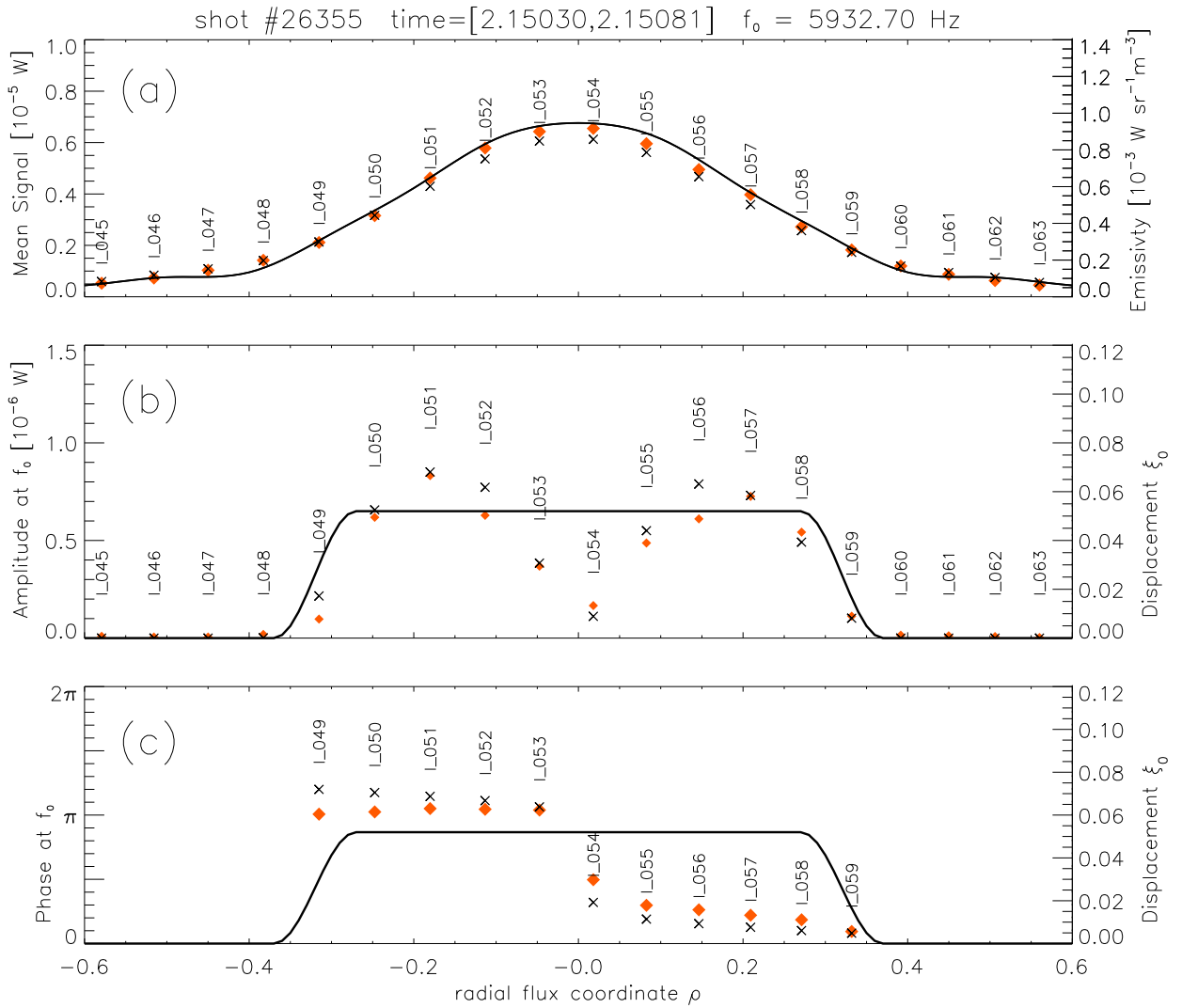


Figure 6.2 – Measured data (\blacklozenge) is compared with the result of the simulation (\times) for the camera I.

The chosen background emissivity $e_0(\rho)$ and the chosen displacement function ξ_0 which describes the magnetic structure of the kink reproduces the measured data quite well.

For the channels which see through the lower region of the plasma $I_{_057}, I_{_058}, I_{_059}$ the amplitude fits the measured amplitude very well.

There is an asymmetry in the simulated amplitudes ($\times I_{_050}, \times I_{_058}$) with respect to the measured amplitudes ($\blacklozenge I_{_050}, \blacklozenge I_{_058}$). Just like discussed for the signals in section 6.1, this asymmetry limits the quality of the fit result. With the model of emissivity on flux surfaces and with this particular equilibrium geometry it is impossible to improve the quality of the amplitude fit.

Comparing the simulated amplitudes ($\times I_{_052}, \times I_{_056}$) and the measured amplitudes ($\blacklozenge I_{_052}, \blacklozenge I_{_056}$) the simulated amplitudes are both too high and there are two possible reasons for this. First it could be, that the displacement is lower in this region. This would mean that there is a local structure at $\rho \approx 0.15$ in the displacement function $\xi_0(\rho)$ and it is not a constant function in this region. Second it could be, that the local emissivity gradient of $e_0(\rho)$ is too high. This would cause the local amplitudes to be too high.

6.3 Investigation of a kink mode with a hollow emissivity profile

It is discussed in section 5 that the measured or simulated amplitudes and the phases of an instability depend on the underlying equilibrium emissivity. In this section a kink mode which displaces a hollow equilibrium emissivity is investigated. We turn to the discharge #25854. In the time range [2.8525 s, 2.8532 s] a kink mode with the frequency $f_0 \approx 7050$ Hz is present.

For this discharge the temperature profile $T_e(\rho)$ and the density profile $n_e(\rho)$ are peaked and therefore it is assumed that the hollowness is due to a hollow tungsten density.

The procedures which are exemplified in section 6.1 and section 6.2 for a peaked emissivity profile are applied and the results for the hollow emissivity profile are shown in figure 6.3.

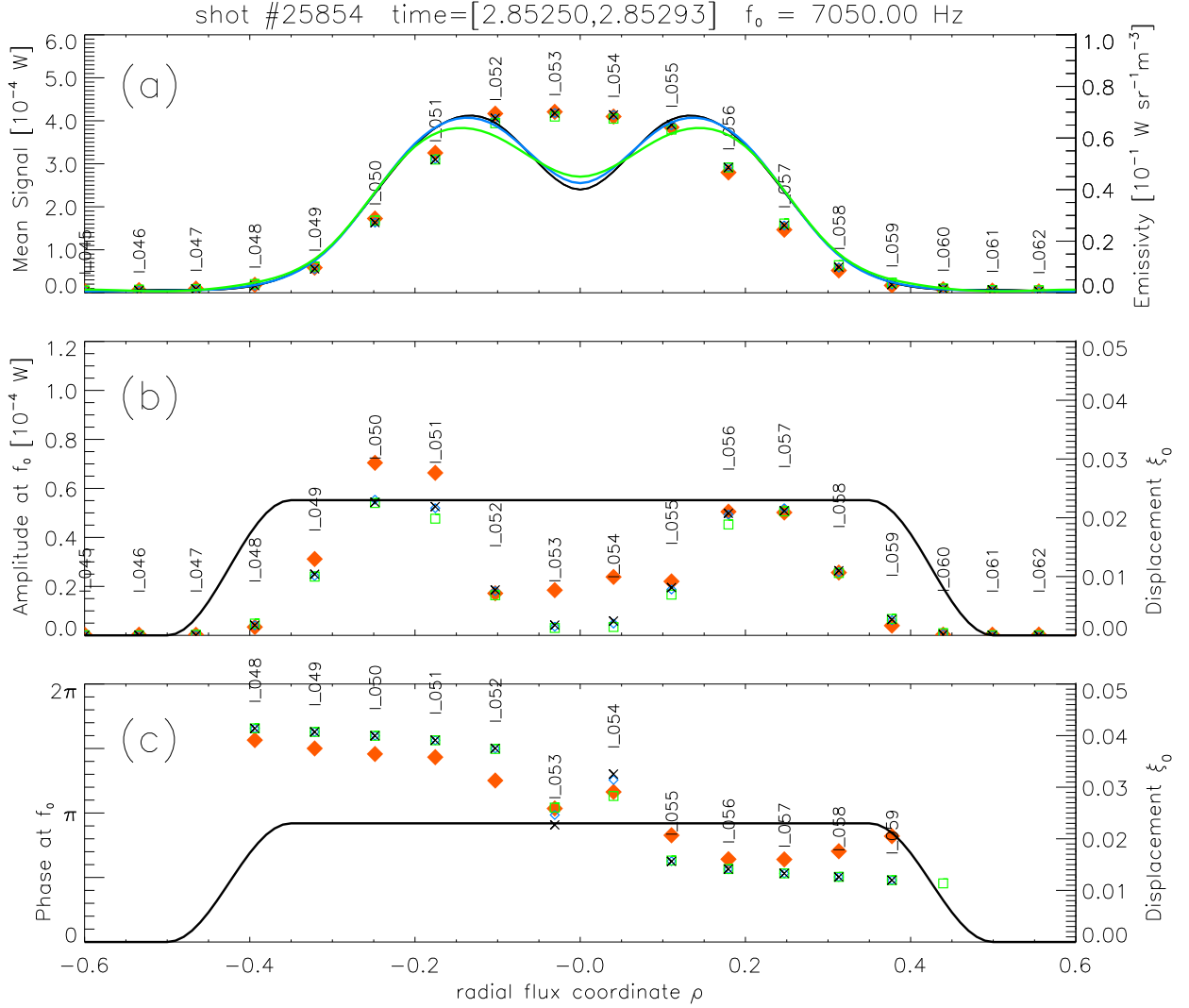


Figure 6.3 – For the camera I the measured mean signals (a), amplitudes (b) and phases (c) are plotted with plot mark \blacklozenge . The results of the simulation is shown with plot mark \times . Note the phase behavior of the channels I_053 and I_054 .

As discussed in section 5.2 the hollowness of the emissivity profile changes the mean signal of the central channels only marginally so it is nearly impossible to reconstruct the hollowness of the background emissivity $e_0(\rho)$ only with the mean signals given. But it is also discussed in section 5.2 that the hollowness has a significant impact on the phases of the central channels.

For this case the emissivity value $e_0(\rho_0)$ at the central node ρ_0 is reconstructed by a comparison with the resulting simulated phase and the measured phase. This is possible because the greater the hollowness the greater is the development of the additional phase jumps of the central channels I_053 and I_054 in figure 6.3.

In order to find the background emissivity profile $e_0(\rho)$ which fits best, the fit has been

performed three times with different fixed emissivity values at the central node:

$$\begin{aligned} e_0(\rho = 0) &= 4.50 \cdot 10^{-2} \\ e_1(\rho = 0) &= 4.25 \cdot 10^{-2} \\ e_2(\rho = 0) &= 4.00 \cdot 10^{-2} \end{aligned}$$

and only the emissivity values at the remaining non central nodes are varied using a least square fit routine. Comparing the central phases the values with plot mark $\square I_{_053}$ and $\square I_{_054}$ fit the measured phases $\blacklozenge I_{_053}$ and $\blacklozenge I_{_054}$ best and only the values for the profile $e_0(\rho)$ are presented:

$$e_0(\rho_i) = 10^{-2} \cdot [4.50, 6.03, 5.67, 1.89, 0.36, 0.06, 0.12, 0.00, 0.00, 0.00, 0.00]_i \quad (6.4)$$

The calculations are carried out with a displacement function defined according to equation 5.1 with the following parameters which are fitted manually:

$$(\rho_1, \rho_2, \zeta_0) = (0.35, 0.50, 0.023) \quad (6.5)$$

Now we turn to the comparison between the amplitudes. There are only small differences between the simulated amplitudes in figure 6.3 (b): an increase in the emissivity gradient causes the amplitudes to increase. The discrepancies between the measured amplitudes and the simulated amplitudes are quite big. In figure 6.3 (b) the simulated amplitudes ($\square I_{_050}, \square I_{_051}, \square I_{_056}, \square I_{_057}$) are asymmetric to the measured amplitudes ($\blacklozenge I_{_050}, \blacklozenge I_{_051}, \blacklozenge I_{_056}, \blacklozenge I_{_057}$). For the asymmetries in the amplitudes the same remarks hold for the asymmetries in the signals which are given in in section 6.1. With the used model of constant emissivity on a flux surface it is not possible to model the measured asymmetries in the amplitudes.

Note that also the corresponding mean signals in figure 6.3 (a) are asymmetric. It is an open question whether a small asymmetry in the spatial background emissivity distribution is sufficient in order to describe such a big and broad asymmetry in the amplitudes. Moreover the amplitudes of the channels $\blacklozenge I_{_053}$ and $\blacklozenge I_{_054}$ are much higher than the simulated amplitudes of these channels. Furthermore the phase distance in figure 6.3 (c) between a pair of channels which is tangent to the same flux surface at $\pm\rho$ is significantly higher for the simulation compared to the measured phase distance. It seems likely that the discrepancies in the phases result from a discrepancy of the position of the inner flux surfaces with respect to the outer flux surfaces. It seems also likely that the discrepancies in the amplitudes are caused by asymmetries in the spatial emissivity distribution.

Recommendations for future work

There are open questions and the area of research of this thesis will remain fruitful. In the following recommendations for future work are listed.

- **Considering an asymmetric background emissivity.** Asymmetries in emissivity due to asymmetries in the spatial distributions of trace impurities are discussed in [39] (equation 10) for HFS/LFS-asymmetries:

$$n_Z^{(1)}(\rho, \theta) = n_{Z0}^{(1)}(\rho) \exp [d(\rho)(R(\rho, \theta)^2 - R_0(\rho)^2)] \quad (7.6)$$

$$\text{with } d(\rho) = \left(1 - \frac{T_e}{T_i + T_e} Z \frac{m_i}{m_z}\right) \frac{m_z \omega^2(\rho)}{2T_Z}$$

where $\omega(\rho)$ is the toroidal rotation velocity, $R_0(\rho)$ is the maximal big radius for a flux surface ρ and T_i, T_Z are the temperatures of the hydrogenic ions and of the impurity with the atomic number Z . The density distribution for up/down-asymmetries is given in [40] and [41].

According to [16] equation (B.13) the emissivity resulting from an impurity - in this case Argon - can be calculated by

$$e_{Ar}^{sxr}(\rho, \theta) = n_e(\rho) n_{Ar}(\rho, \theta) L_{Ar}^{sxr}(\rho, \theta) \quad (7.7)$$

where L_{Ar}^{sxr} is the impurity total radiative power coefficient. This means that the emissivity resulting from an impurity is proportional to the density of the impurity and the equation for the density distribution of the impurities 7.7 can be rewritten in terms of emissivity reducing the - maybe unnecessary - spectral information. The final spatial emissivity distribution considering asymmetries is given by:

$$e(\rho, \theta) = e_1(\rho) + e_2(\rho) \sin(\theta) + e_3(\rho) \exp[d(\rho)(R(\rho, \theta)^2 - R_0(\rho)^2)] \quad (7.8)$$

where $e_1(\rho)$ is the emissivity which is constant on the flux surface, $e_2(\rho)$ and $e_3(\rho)$ describe the up/down and HFS/LFS asymmetries. The function $d(\rho)$ is defined in equation 7.7 and it is given by measured quantities like the temperature profile and the toroidal rotation velocity $\omega(\rho)$. The functions $e_1(\rho), e_2(\rho)$ and $e_3(\rho)$ are to be varied with a fit routine until measured and simulated signals fit best. Note that it is also necessary to consider emissivity asymmetries due to discrepancies in the equilibrium flux surface geometry.

- **Mode perturbed asymmetric background emissivity.** Considering asymmetric emissivity distributions like described in the point above the question is what the impact would be if there is a mode present? With an implemented asymmetric emissivity distribution $e(\rho, \theta)$ it is possible to consider a two-dimensional poloidal displacement on it. This will result in asymmetries in the simulated amplitudes which may reproduce the measured amplitudes.

The question is, how the impurities are spatially distributed if there is a mode present. Is there tungsten accumulation in magnetic islands and to what extend?

By describing the measured asymmetric amplitudes with the above described approach, it is possible to draw conclusions on the spatial distribution of the impurities with a mode present.

- **Determine the magnetic structure of instabilities.** In this thesis the displacement $\xi_0(\rho)$ and so the magnetic structure of the instability is chosen in such a way that the measured signals are reproduced. The chosen magnetic structure is consistent with the measured signals but it is not shown, that the chosen magnetic structure is necessary in order to fit the measured signals. In order to study the magnetic structure of plasma instabilities more closely the magnetic structure which is given by $\rho'(\rho, \theta)$ in equation 4.22 can be compared with other measured flux surface quantities. For example temperature T_e (ECE diagnostics) or current j (Mirnov diagnostics). With a displacement $\xi_0(\rho)$ determined by the sxr diagnostics it is possible to crosscheck this magnetic structure with the other diagnostics mentioned above.
- **Consideration of an angular dependent detector response.** The angular dependency of the spectral response function of the solid-state-detector is neglected in this thesis. But it is observed - for example in figure 4.1 -, that there are discrepancies between the simulated and the measured signals which depend on the angle of the incident radiation. In figure 4.1 for the cameras H, K and J the discrepancies between simulated and the measured signals are higher the steeper the angle of incidence is. The possible causes for this effect are deviations in the thickness of the beryllium foil, the dependency of the spectral response of the detector on the angle of incident radiation and effects resulting from the thickness of the material in which the pinhole is.

The discrepancy can be studied further by reconstructing emissivity profiles $e(\rho)$ using only central chips for many discharges and for many time windows (so that the statistics is improved) and by comparing the simulated signals (resulting from the profiles) with the measured mean signals resulting from non-central chips.

One can investigate how the discrepancy depends on the angle of the incident radiation. Furthermore one can investigate to what extent the discrepancy depends on the temperature T_e of the plasma and therefore on the the spectral distribution of the radiation.

For the reconstruction of the emissivity profile one can add a fit parameter to consider the angel dependent response by multiplying the simulated signal with a correction factor $(1 - c\alpha^2)$, where α is the angle of incidence and the constant c is to be determine with the fit routine. The above given correction factor with quadratic dependency of α is motivated by figure 6 in [17].

- **Verification of the plasma center calculation.** Efforts are being made to calculate the plasma center in real time with the real time sxr signals given. With the virtual sxr diagnostics it is possible to verify the method. The quality of the calculated plasma center depends on the flatness of the emissivity profile and with the virtual sxr diagnostics it is possible to investigate the quality of the result in the dependency of the flatness of the profile.

Summary and conclusion

In the scope of this thesis a virtual soft x-ray (sxr) diagnostics is developed including the full three-dimensional geometry of the VOS in the calculation. The emissivity inside the VOS contributes accordingly to the solid angle of the *seen* detector area. The code is tested with the methods described in section 3.3.

The spatial emissivity distribution is displaced due to plasma modes. A model for the emissivity of a mode perturbed plasma is developed considering the poloidal displacement which depends on the toroidal position. It is discussed that the consideration of the poloidal vectorial displacement in ρ and in θ -direction is crucial, since it is shown in section 4.3 that with the radial perturbation model and with the approximate model mathematical artifacts like negative emissivity and an additional island can occur.

Furthermore it is shown that the approximate model cannot describe the phenomenon of frequency doubling. Because of these limitations these models should not be used and the full displacement in ρ and in θ -direction should be considered.

Idealized examples of ideal $(m, n) = (1, 1)$ kink modes are investigated in dependence of the emissivity profile (especially its gradient), the displacement and the equilibrium geometry. By keeping two of these three dependencies constant and varying the third, the resulting effects (which are isolated from disturbing influences) on the mean signals, on the mode amplitudes and phases of the simulated signals are investigated.

It turned out that a change of the emissivity profile only has a small impact on the mean signals. Therefore it is difficult to reconstruct emissivity profiles just with the measured mean signals given. The reconstruction of the measured time traces resulting from observed kink modes is possible by varying the background emissivity $e_0(\rho)$ and the displacement function $\xi_0(\rho)$. Comparing the measured with the simulated phases the phase distance is not well reproduced.

A small change of the gradient of the emissivity profile causes a big change of the mode amplitude. Furthermore there is coupling between the displacement and the mean signal: a change of the displacement has an impact on the simulated mean signals. In principal the background emissivity profile and the displacement function should be fitted simultaneously.

For emissivity profiles, which are hollow in the core plasma, it is shown that it is almost impossible to reconstruct the degree of hollowness with the measured mean signals given. But it is also shown that the additional phase structure of hollow emissivity profiles can be a criterion for the degree of hollowness. The additional structure in the phases of the central channels which is observed for a kink mode in a hollow emissivity profile is reconstructed with good accuracy by varying the degree of hollowness.

The investigation shows that for peaked profiles the relative phase between the signals is independent of the gradient of the emissivity and it is independent of the displacement. Furthermore it is independent of a rigid shift of all flux surfaces.

It turned out that the relative phases depend very sensitively on the shift of the flux surfaces with respect to each other. It is most likely that the systematic discrepancy between the measured and the simulated phases can be removed by a shift of the inner flux surfaces with unmodified outer flux surfaces. This shift also changes the mean signals and the amplitudes. So the effect is also coupled with the background emissivity and the displacement.

With a virtual srx diagnostics it is possible to compare the simulated symmetric signals resulting from a symmetric emissivity profile with the measured signals. With this comparison it is possible to detect asymmetries in the measured signals, adjusted for geometry effects of the VOS.

Asymmetries are caused by the emissivity not being constant on flux surfaces or/and by errors in the calculated equilibrium geometry. The asymmetries due to the equilibrium geometry could be removed by shifting the inner flux surfaces until the simulated agree with the measured phases. It is very likely that the remaining asymmetries are due to the emissivity which is not constant on flux surfaces. It is recommended for future work to consider mode displaced asymmetric emissivity distributions.

For the variation of big emissivity structures for example due to the considered (1,1) kink modes the change of the geometry of the VOS has no significant impact on the simulated signals. For the variation of small localized emissivity structures, such as snakes or islands, the VOS approach can show its potency in comparison with the LOS approach.

Appendix

Appendix A

Signals resulting from the approximate model are harmonic in time

It is shown that signals resulting from the approximate model are harmonic in time. Because the amplitude resulting from the time independent part of the emissivity is zero we consider only the time dependent part of the approximate model. Then equation 4.25 reduces to

$$\begin{aligned}\epsilon(\rho, \theta^*, \phi) &= \underbrace{\xi_0(\rho) \frac{d\epsilon}{d\rho}}_{=:B(\rho)} \underbrace{\text{Cos}(m\theta^* + n\phi + \phi_0 + \omega t)}_{=: \varphi(\theta^*, \phi)} \quad (.1) \\ &= B(\rho) \text{Cos}(\varphi(\theta^*, \phi) + \omega t) \quad (.2)\end{aligned}$$

Using $B_i = B(\rho_i)$ and $\varphi_i = \varphi(\theta_i^*, \phi_i)$ the emissivity for every grid-point $(\rho_i, \theta_i^*, \phi_i)$ is given by:

$$e_i = B_i \text{Cos}(\varphi_i + \omega t). \quad (.3)$$

According to section 5.4.1 the signal caused by the emissivity which is defined in (.3) is given by:

$$S_{SXR} = \sum_{i=1}^N \Omega_i V_i e_i \quad (.4)$$

Insertion of equation (.3) in equation (.4) and using $D_i = \Omega_i V_i B_i$ leads to

$$S_{SXR} = \sum_{i=1}^N \Omega_i V_i B_i \text{Cos}(\varphi_i + \omega t) \quad (.5)$$

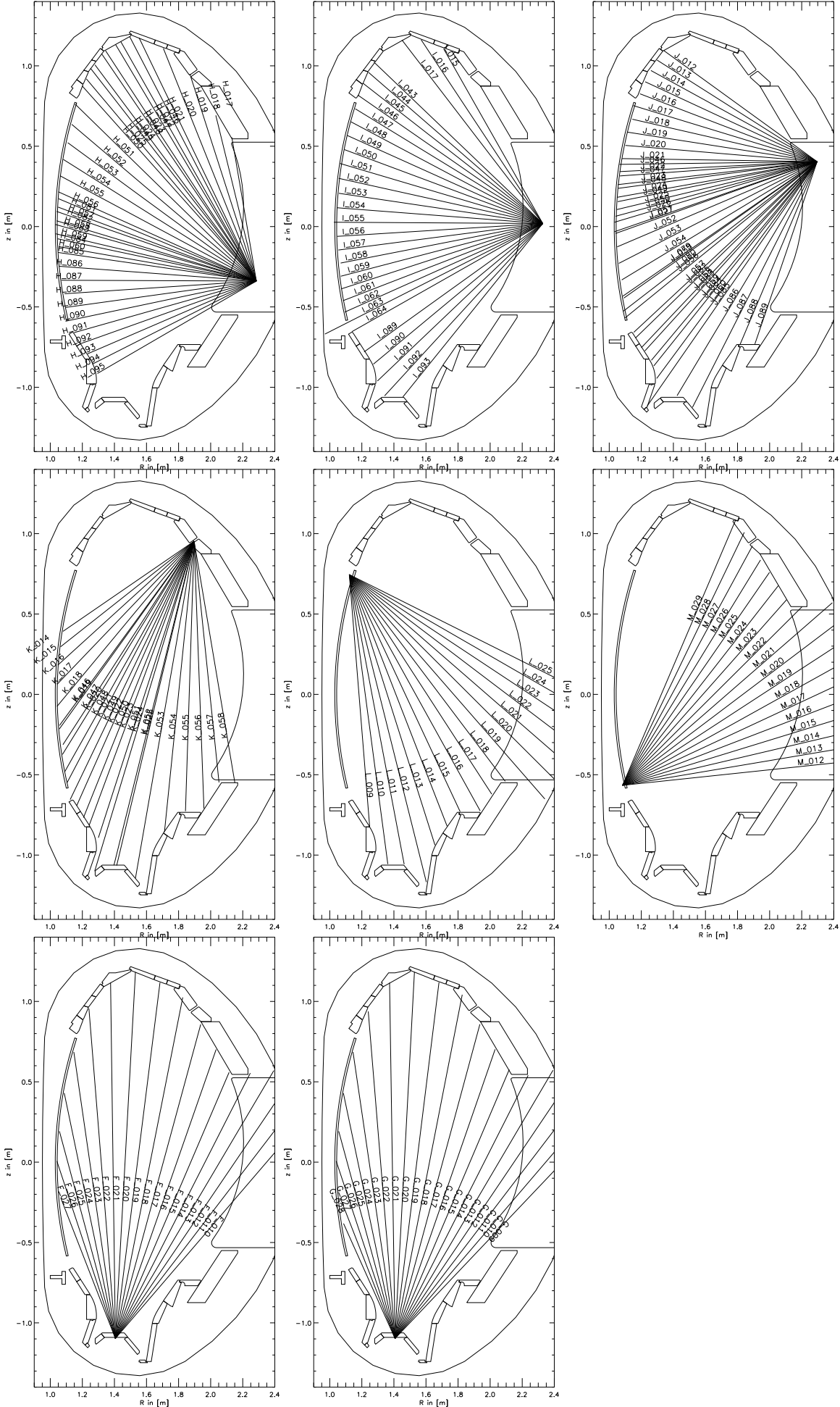
Now we use the fact that a finite sum of harmonic waves with the same frequency ω result in a single harmonic wave with the same frequency [28]. This means that the signal is harmonic in time:

$$S_{SXR} = \hat{D} \text{Cos}(\hat{\varphi} + \omega t). \quad (.6)$$

Note that this argumentation is independent of the values of the phases $\varphi_i = \varphi(\theta_i^*, \phi_i)$ and the argumentation still holds if we consider θ_i instead of θ_i^* .

Appendix B

AVOS of the sxr channels in AUG



References

- [1] International Energy Agency. World energy outlook 2010 factsheet, 2010.
- [2] V. Smil. Energy at the Crossroads. MIT Press, 2003
- [3] The Joint European Torus (JET). <http://www.jet.efda.org/fusion-basics/fusion-as-a-future-energy-source/advantages-of-fusion/>, visited on 7/2011.
- [4] ITER project. www.iter.org, visited on 7/2011.
- [5] A. Koenies and K. Krieger. Summer University for Plasma Physics, Garching/Munich, Germany, 2004.
- [6] J. A. Wesson. Tokamaks. Clarendon Press, third edition, 2009.
- [7] M. Kaufmann. Plasmaphysik und Fusionsforschung. Vieweg+Teubner, 2003.
- [8] J. C. Fuchs and W. Schneider. Routines and Tools for Working with Equilibria Data. V 0.9.0, 2010
- [9] Wikipedia. http://de.wikipedia.org/wiki/Trapezregel#Zusammengesetzte_Tangententrapezformel, visited on 7/2011.
- [10] Wikipedia. http://en.wikipedia.org/wiki/Solid_angle, visited on 7/2011.
- [11] I. S. Kyprianou et al. A method to estimate the point response function of digital x-ray detectors from edge measurements. Physics of Medical Imaging 65100B, 2007.
- [12] V. Igochine, A. Gude, M. Maraschek, ASDEX Upgrade team. Hotlink based Soft X-ray Diagnostic on ASDEX Upgrade, IPP 1/338, 2010.
- [13] M. M. Lavrentiev et al. Computer modelling in tomography and ill-posed problems. De Gruyter, 2001.
- [14] Numerical Recipes. Cambridge University Press, 2007
- [15] J. P. Freidberg. Ideal Magnetohydrodynamics. Plenum Press, 1987.
- [16] M. Sertoli. Local effects of ECRH on argon transport at ASDEX Upgrade. PhD thesis, 2010.
- [17] M. Anton et al. Relative calibration of photodiodes in the soft-x-ray spectral range. Rev. Sci. Instrum. 66 (7), 1995.
- [18] M. Anton et al. X-ray tomography on the TCV Tokamak. In Plasma Phys. Control. Fusion 38:1849, 1996.
- [19] C. P. Tanzi. Emission of soft x-ray and microwave radiation from tokamak plasmas PhD thesis, University Utrecht, 1996.
- [20] Data sheet of centronic Series 5T detectors (LD35-5T). <http://www.centronic.co.uk>.
- [21] J. S. Kim et al. Soft x-ray virtual diagnostics for tokamak simulations. Review of Scientific Instruments 80:113503, 2009.
- [22] M. Sokoll. MHD-Instabilitäten in magnetisch eingeschlossenen Plasmen und ihre tomographische Rekonstruktion im Röntgenlicht. PhD thesis, IPP 1/309, Garching near Munich, 1997.
- [23] H. J. de Blank. MHD Instabilities in Tokamaks. In Transactions of Fusion Science and Technology Vol. 49:118, 2006.
- [24] H.J. de Blank and T. Schep. Theory of $m = 1$ kink mode in toroidal plasma. Phys.

- Fluids B, 1991.
- [25] G. Bateman. MHD Instabilities. MIT Press, 1978.
 - [26] C.P. Tanzi et al. Estimate of magnetic reconnection in sawtoothing RTP plasmas by means of soft x-ray tomography. In Proc. of the 22nd EPS Conf. on Contr. Fusion and Plasma Phys. Part II-029, Bournemouth, 1995.
 - [27] V. Igochine. Investigation of complex MHD activity by a combined use of various diagnostics. In Nucl. Fusion 43:1801, 2003.
 - [28] I.N. Bronshtein et al. Handbook of Mathematics. Springer fifth edition, 2007.
 - [29] W. Benenson et al. Handbook of Physics. Springer, 2002.
 - [30] L.C. Ingesson. Visible-light tomography of tokamak plasmas. PhD thesis, University of Eindhoven, 1995.
 - [31] L.C. Ingesson et al. Projection-space methods to take into account Finite Beam-width Effects in Two-dimensional Tomography Algorithms. JET-P(98)06, 1998.
 - [32] A. Flaws. The Role of MHD Instabilities in the Improved H-Mode Scenario. PhD thesis, 2009.
 - [33] M. Schittenhelm et al. Analysis of coupled MHD modes with Mirnov probes in Asdex Upgrade. Nucl. Fusion 37:1255, 1997.
 - [34] A. Gude et al. Hollow central radiation profiles and inverse sawtooth-like crashes in ASDEX Upgrade plasmas with central wave heating. 37th EPS Conference on Plasma Physics, P4.124, 2010.
 - [35] A. Gude. Hollow SXR radiation profiles. ASDEX Upgrade Core Physics Forum, Garching, Presentation 30. September 2010.
 - [36] B. N. Breizman et al. On the theory of internal kink oscillations. Physics of Plasmas, Volume 5, Number 6, 1998.
 - [37] D. Naujoks et al. Tungsten as target material in fusion devices. Nucl. Fusion 36 671, 1996.
 - [38] R.S. Granetz et al. Is X-ray emissivity constant on magnetic flux surfaces? Fusion Engineering and Design 34-35, 153-157, 1997.
 - [39] J. A. Wesson. Poloidal distribution of impurities in a rotating Tokamak plasma. Nucl. Fusion 37 No. 5, 1997.
 - [40] J.E. Rice et al. X-ray observations of up-down impurity density asymmetries in Alcator C-Mod plasmas. Nucl. Fusion, Vol. 37, No. 2, 1997.
 - [41] R.D. Durst. Vertical asymmetries in soft X-ray emissivity in COMPASS-C Nucl. Fusion, Vol. 32, No.12, 1992.
 - [42] R. Dux et al. Influence of the heating profile on impurity transport in ASDEX Upgrade. Plasma Phys. Control. Fusion 45:1815, 2003.
 - [43] P. Piovesan et al. TAE internal structure through high-resolution soft x-ray measurements in ASDEX-Upgrade. Nucl. Fusion 48: 065001, 2008.
 - [44] S. Guenter and H. Zohm. Chapter 9: Performance-limiting MHD activity and possibilities for its stabilization in ASDEX Upgrade. Fusion Science and Technology, Vol. 44, 2003.
 - [45] W. Suttrop et al. First Observation of Edge Localized Modes Mitigation with Resonant and Nonresonant Magnetic Perturbations in ASDEX Upgrade. Phys. Rev. Lett. 106, 225004, 2011.

- [46] V. Igochine. Investigation of MHD Instabilities in Conventional and Advanced Tokamak Scenarios on ASDEX Upgrade. PhD thesis, 2002.
- [47] R. J. Hastie. Sawtooth instability in Tokamak plasmas. *Astrophysics and Space Science* 256: 177–204, 1998.
- [48] S. Migliuolo. Theory of ideal and resistive $m=1$ modes in tokamaks. *Nucl. Fusion* 33:1721, 1993.
- [49] W. A. Newcomb. Hydromagnetic Stability of a Diffuse Linear Pinch. *Annals of physics*: 10, 232-267, 1960.
- [50] K. Tritz et al. Three-dimensional modeling and inversion of x-ray pinhole detector arrays. *Review of Scientific Instruments* 77, 2006.
- [51] D. D. Schnack. *Lectures in Magnetohydrodynamics*. Springer, 2009.
- [52] M.A. Dubois. Method of cartography of $q = 1$ islands during sawtooth activity in tokamaks.
- [53] J.P. Qian et al. Equilibrium reconstruction of plasma profiles based on soft x-ray imaging in DIII-D. *Nucl. Fusion* 49, 2009.